



HAL
open science

Damage detection for wind turbine towers with Digital Image Correlation

Jordan Curt

► **To cite this version:**

Jordan Curt. Damage detection for wind turbine towers with Digital Image Correlation. Mechanics of materials [physics.class-ph]. Université Paris-Saclay, 2021. English. NNT : 2021UPAST008 . tel-03152984

HAL Id: tel-03152984

<https://theses.hal.science/tel-03152984>

Submitted on 26 Feb 2021

HAL is a multi-disciplinary open access archive for the deposit and dissemination of scientific research documents, whether they are published or not. The documents may come from teaching and research institutions in France or abroad, or from public or private research centers.

L'archive ouverte pluridisciplinaire **HAL**, est destinée au dépôt et à la diffusion de documents scientifiques de niveau recherche, publiés ou non, émanant des établissements d'enseignement et de recherche français ou étrangers, des laboratoires publics ou privés.

Damage detection for wind turbine towers with digital image correlation

Thèse de doctorat de l'Université Paris-Saclay

École doctorale n° 579, Sciences mécaniques et énergétiques, matériaux et géosciences (SMEMAG)

Spécialité de doctorat: Mécanique des solides

Unité de recherche: Université Paris-Saclay, ENS Paris-Saclay, CNRS, LMT - Laboratoire de Mécanique et Technologie, 91190, Gif-sur-Yvette, France

Référent: : ENS Paris-Saclay

Thèse présentée et soutenue en visioconférence totale le 8 janvier 2021, par

Jordan Curt

Composition du jury:

Véronique Aubin Professeure, Centrale-Supélec, MSSMAT	Présidente
Evelyne Toussaint Professeure, Université Clermont-Auvergne, IP	Rapporteur
Jean-Charles Passieux Professeur, INSA Toulouse, ICA	Rapporteur
Sylvain Calloch Professeur, ENSTA Bretagne, IRDL	Examineur
Jan Neggers Maître de Conférence, Centrale-Supélec, MSSMAT	Examineur
Mathieu Corus Ingénieur de recherche expert, EDF R&D	Examineur
Stéphane Roux Directeur de Recherche, CNRS, ENS Paris-Saclay, LMT	Directeur de thèse
François Hild Directeur de Recherche, CNRS, ENS-Paris-Saclay, LMT	Codirecteur de thèse
Matteo Capaldo Ingénieur de recherche, EDF R&D	Coencadrant de thèse, Invité

"Je crois que l'avenir de l'humanité est dans le progrès de la raison par la science." E. Zola

Remerciements

Afin de mettre un point final à ce long périple qu'est la thèse, il ne me reste qu'à exprimer de nombreux remerciements aux personnes qui m'ont permis d'aller au bout de cette aventure...

Tout d'abord, je remercie sincèrement tous les membres du jury, pour leurs nombreuses questions et l'intérêt qu'ils ont porté à mon travail. Merci beaucoup à V. Aubin d'avoir accepté de présider ce jury. Une thèse ne peut être soutenue sans le travail préalable des rapporteurs, et je veux témoigner ici à E. Toussaint et J-C. Passieux toute ma reconnaissance.

J'adresse un grand MERCI à mes directeurs de thèse Stéphane et François. Ces trois années sont passées si vite, j'ai beaucoup appris à leurs côtés, bien plus que ce que j'aurais pu imaginer. Leur disponibilité et leur pédagogie ont été de grands atouts pour mener à bien ce travail.

Côté entreprise, je remercie grandement Matteo pour son accompagnement, son soutien, ses blagues et sa grande aide pour la logistique au cours de cette thèse. Les souvenirs de virée sur site et de pose de caméra à 35m de hauteur resteront gravés dans ma mémoire.

Je remercie tous les membres du LMT pour l'ambiance qui y règne. Merci beaucoup à Charlène et Xavier pour leur aide, tant administrative que logistique. Merci à mes co-bureaux pour les excellents moments : les rires et les discussions passionnées ont toujours été au rendez vous.

J'ai eu chance d'appartenir à un super groupe côté EDF pendant ces trois ans. Malgré le RER B c'était toujours un plaisir d'aller sur site, merci la team T6E ! Mention spéciale à mes collègues doctorants Anais, Quentin et Antoine ! Merci à Malika et Catherine pour leur aide administrative et leur patience, j'étais loin d'être le meilleur dans ce domaine.

Je remercie tous mes amis qui m'ont soutenu tout au long de ce travail. Voir autant d'eux assister (même en visio) à ma soutenance m'a fait chaud au coeur. Mention spéciale à Bap qui a partagé mon quotidien durant les deux premières années... *Malineum manilae exae*.

Je remercie mes parents, ma famille qui m'ont accompagné au cours de ce travail. Un grand merci également à la famille Eon pour son soutien !

Les derniers (et plus grands) remerciements vont à Delphine, qui m'a soutenu et motivé tout au long de ce travail. Sa grande positivité ainsi que ses conseils ont été, jusqu'au dernier jour, essentiels à ma réussite.

A ceux qui s'aventureront vers la suite de ce manuscrit, je vous souhaite une lecture aussi plaisante que possible !

Arvi Pa !

Contents

1	Introduction	9
1.1	Introduction to Wind Energy	10
1.2	Industrial context	12
1.3	Wind turbine tower lifetime	13
1.3.1	Aeroelastics loads	14
1.3.2	Calculation methods	14
1.3.3	Associated uncertainties	15
1.3.4	Residual life time estimation and structure integrity	16
1.3.5	Wind turbine incidents and failures	17
1.4	Wind turbine tower health estimation	22
1.4.1	Non destructive testing	22
1.4.2	Structural Health Monitoring	23
1.5	Scientific issues	24
2	Simulation of a wind turbine tower failure	29
2.1	Introduction	30
2.2	Buckling of a wind turbine tower	30
2.2.1	Litterature review on buckling	30
2.2.2	Buckling simulation with an academic turbine model	33
2.3	Wind turbine failure by crack propagation	39
2.3.1	Literature review	39
2.3.2	Fracture mechanics	40
2.3.3	Application to NREL case	43
2.4	Failure modes and simulation of a storm case	44
2.4.1	Worst failure mode with a crack	44
2.4.2	Simulation of critical load	46
2.5	Conclusion and perspectives	48
3	DIC principle	49
3.1	Introduction	50

3.2	Instantaneous DIC	51
3.2.1	Monochrome DIC	51
3.2.2	Displacement measurement	52
3.2.3	Measurement uncertainty	53
3.2.4	Gray level correction	54
3.3	Spatio-temporal DIC	54
3.3.1	Introduction	54
3.3.2	Classical spatio-temporal DIC	55
3.3.3	Spatio-temporal PGD-DIC	55
3.3.4	Summary	57
3.4	Optimal Color Digital Image Correlation	57
3.4.1	Introduction	57
3.4.2	Color image registration	59
3.4.3	Noise characterization	61
3.4.4	Uncertainty quantifications	69
3.4.5	Conclusion and outlook	72
4	Damage detection at the mesoscale	75
4.1	Structural Health Monitoring with DIC	76
4.1.1	Introduction	76
4.1.2	Damage detection via DIC	79
4.1.3	Case study: Fatigue crack propagation	80
4.1.4	New DIC approach based on optimal extractors	88
4.1.5	Application of one-step DIC	93
4.1.6	Example of extractor	94
4.1.7	Conclusion	95
4.2	Logistical aspects	97
4.2.1	Device	97
4.2.2	Needed measurement resolution	97
4.2.3	Camera	98
4.3	Conclusion and perspectives	100
5	Damage detection at the macroscale	101
5.1	Introduction	102
5.1.1	Measurement of large structures in an outdoor environment	102
5.1.2	Operative Modal Analysis (OMA)	103
5.1.3	Modal analysis with DIC	104
5.2	Wind turbine tower displacement measurement	105
5.2.1	Experimental set-up	105

5.2.2	Strategy	108
5.2.3	Displacement measurement	109
5.3	Wind turbine tower modal analysis	111
5.3.1	First frequency measurement	111
5.3.2	Second frequency measurement	112
5.3.3	Influence of the FE model	116
5.3.4	Summary	116
5.4	Damage identification	118
5.4.1	DIC based methods to calibrate FE models	118
5.4.2	Damage quantification via DIC	118
5.4.3	Sensitivity to damage detection	120
5.5	Conclusion and perspectives	122
6	Conclusion and Perspectives	125
A	Description of aeroelastic simulations	129
B	One step DIC with large displacements	131
B.1	Inhomogeneous filtering	131
B.2	Calibration of the filter	132
B.3	Application to heterogeneous displacement fields	132
C	Transformation between the real world and the camera frame	137
D	Résumé étendu en Français	141
	Bibliography	145

List of Figures

1.1	Schematic view of an onshore wind turbine [Futuren, 2020].	10
1.2	Production curve of a 3MW Vestas wind turbine [Harrison et al., 2008].	11
1.3	Expected wind turbine hub height growth [Wiser et al., 2016].	12
1.4	CapEx (a) and Levelized Cost Of Energy (LCOE) (b) for a wind turbine in 2018 [Stehly and Beiter, 2020].	13
1.5	Classification of a wind site (a) and associated wind rose (b) [Loroux, 2018].	14
1.6	Stress undergone by a wind turbine tower under a flexural loading [Loroux, 2018].	15
1.7	10 minutes damage (rainflow count and Miner rule) reported along seasons in [Loroux, 2018].	16
1.8	Wind turbine failure (a) and downtime (b) rates [Reder et al., 2016].	17
1.9	Photo of a crack in a weld [Lacalle et al., 2011].	18
1.10	Section of a collapsed wind turbine in Taiwan [Chou and Tu, 2011].	19
1.11	Collapsed wind turbine in Germany [The-Civil-Engineer, 2017].	19
1.12	Collapsed wind turbine in Bouin, France [Parisien, 2018].	20
1.13	Collapsed wind turbine in Guigneville, France [France-3, 2018].	21
1.14	Control of a wind turbine tower thanks to ultrasound waves [Force-Technology, 2020].	22
2.1	Tower without (a) and with refinement (b).	34
2.2	Applied force versus displacement at tower top.	35
2.3	Tower deformation profiles at step B (a), step C (b) and step D (c) . The displacement is magnified $\times 1.5$ and the colors highlight the plastic strains.	36
2.4	Example of wind turbine tower failing by buckling. [Jay et al., 2016]	37
2.5	Zoom around the mesh of the crack.	38
2.6	Plastic strain field for a 3MN load without (a) and with a crack (b).	38
2.7	Influence of a crack placed in the tearing or in the compressive side on the critical buckling load for several crack lengths at a 25 m height (a) and for different elevations in the tower (b).	39
2.8	Different modes of fracture.	40
2.9	Three crack propagation regimes [Dillian et al., 2017]. 1: no propagation, 2: stable propagation, 3: unstable propagation	43

2.10	Mesh in the crack tip vicinity from side view (a) and upper view (b).	43
2.11	Strain energy release rate for a 10 cm crack for different upper integration bounds . .	44
2.12	Critical tower loads corresponding to several crack lengths	45
2.13	Critical loadings concerning buckling and critical crack propagation.	45
2.14	Aeroelastic loads simulated with Diego with a wind misalignment of 20 degrees for a wind velocity of 50 m/s (a) and for others (b).	47
2.15	Maximums tower top loads due to rotor misalignment.	47
3.1	Bayer pattern that can be used in color cameras	59
3.2	Color speckle pattern used herein	61
3.3	Autocorrelation functions for the red field for the first (a) and second (b) images . .	63
3.4	Autocorrelation functions along x (a) and y (b) directions	64
3.5	Variance of red brightness with (a) and without (b) corrections for rigid body motions. Units are in color levels (GL), encoded over 16 bits. The different symbols corresponds to the different images.	65
3.6	Variance for the green (a) and blue (b) color fields as functions of the brightness level	66
3.7	Variances for the green (a) and blue (b) color fields after Anscombe transform	67
3.8	Plot of noise covariance matrix eigenvectors in planes (a) Red-Green, (b) Red-Blue and (c) Green-Blue. The eigenvector denoted as “Vect $i - j$ ” corresponds to the i th eigenvector of the j th image	68
3.9	Projections of Figure 3.2 onto (a) first, (b) second, and (c) third color modes.	69
3.10	Black and white speckle pattern used herein	70
3.11	Standard displacement uncertainties with a black and white speckle pattern along x (a) and y (b) directions	71
3.12	Standard displacement uncertainties with a color speckle pattern along x (a) and y (b) directions	72
4.1	(a) Experimental set up. (b) Specimen surface monitored by the camera	81
4.2	(a) Mesh used in T3-DIC analyses. The red rectangle is the region used to pre-calculate the rigid body translations. (b) Zoom of the mesh showing the refinement close to the crack tip.	82
4.3	(a) Eigen values associated with the first 15 modes. (b) Temporal modes $\phi_i(t)$	83
4.4	(a,c) First spatial mode Ψ_1^* respectively along x and y directions. (b,d) Corresponding displacement modes Ψ_1	84
4.5	Second spatial mode Ψ_2 along x (a) and y (b) directions.	85
4.6	Third spatial mode Ψ_3 along x (a) and y (b) directions.	85
4.7	Projection displacement error indicators for all five steps. (a,b) Standard deviation for 3 and 6 modes respectively. (b,d) Corresponding maximum levels.	87

4.8	Normalized standard deviation (a) and maximum (b) displacement errors as functions of the number of modes.	88
4.9	Displacements fields (expressed in px) along the x-direction for steps 1 (a) and 3 (c), and the corresponding projection errors (b,d).	89
4.10	Locations of maximum error for the steps 1 (a) and 3 (b).	90
4.11	Comparison of mean RMS residuals before and after BC corrections for the five steps.	90
4.12	(a) Comparison of RMS residuals with direct DIC and after projection onto the modal basis. (b) Error induced by projection onto the modal displacement basis.	91
4.13	Optimal filtering length for subpixel rigid body translations.	93
4.14	(a) Mean “One-step” DIC absolute error and its standard deviation over the whole set of images from the learning step. (b) Results detailed along each direction.	94
4.15	Filtered image (a) and extractor (b) for the first mode.	95
4.16	Mean RMS residuals after one-step DIC (a). RMS residuals differences between the initial step and the other steps for both T3-DIC and “one-step” DIC.	96
4.17	Modeling schematic of the displacement perturbation induced by a crack (a) and associated results (b). The displacement jump is recorded at the crack middle, where it is maximum.	98
4.18	Picture of a Raspberry Pi and the associated camera.	99
4.19	Experimental set-up (a). The camera is inside the red rectangle, and the observed zone is in the blue rectangle. Camera field of view with DIC mesh (b).	99
5.1	(a) Set-up for image acquisition of the wind turbine tower. (b) Picture of the wind turbine tower taken by the camera.	106
5.2	Gray level through a horizontal line (a) and corresponding gradient (b).	107
5.3	Images acquired with a E70D camera of wind turbines without (a) and with blade shadow (b).	107
5.4	Zoom of the turbine (a) and corresponding selection of pixels (of white color) for DIC application (b).	108
5.5	Three first modes of the wind turbine tower model calculated with a multiple beam FE code. The y-axis is dimensionless with respect to the tower height.	109
5.6	Measurement uncertainty associated with each degree of freedom depending on the number of vibration modes.	110
5.7	(a) Time history of the amplitudes of the two degrees of freedom (translation in blue, and first vibration mode in orange) considered in the DIC analysis for series # 1. (b) Time amplitude of the first vibration mode for series # 1 and # 4 showing similar oscillations although with different amplitudes depending on series.	112
5.8	Power spectrum (a) and estimated peak frequency values with corresponding error bars (b) for the four pictures sets. The power spectrum is the squared Fast Fourier Transform.	113

5.9	Temporal amplitudes obtained for experiment #1 (a) and power spectra obtained for the second mode temporal signal (b).	113
5.10	Amplitude of the first vibration mode with a PGD approach of experiment #1.	114
5.11	Temporal shape functions used for the spatio-temporal approach.	115
5.12	Temporal norm for several frequencies of the second vibration modes for all four experiments.	116
5.13	Influence of the RNA stiffness on the first (a) and second (b) mode shapes. The y-axis is dimensionless with respect to the tower height.	117
5.14	Sensitivity field relative to damage for the first vibration mode (a). It is calculated by considering a damage level $D = 0.01$ at 25 m height (0.31% of the total tower height).	119
5.15	Zoom of the 3D FE mesh of the tower with a crack.	121
5.16	Comparison between 3D FE model and a beam model about kinematic impact of damage. The graph has two ordinates: the homogenised damage variable for the beam model and the crack length for the 3D model.	121
5.17	Measurement uncertainty relative to damage variable.	122
A.1	Corrected coefficients of the NACA64 airfoil [Jonkman et al., 2009].	129
A.2	NREL 5MW model rendering in DIEGO. The arrows represent the wind velocity at multiple points.	130
B.1	Absolute (a) and relative (b) optimal filtering lengths.	132
B.2	(a) Displacement map along x -direction in pixels. (b) Corresponding adaptively filtered image.	133
B.3	One-step DIC error with homogeneous and inhomogeneous filtering over the whole set of displacement fields, for case 1 (a) and case 2 (b).	134
B.4	One-step DIC error with homogeneous and inhomogeneous filtering for the larger displacement magnitude, for case 1 (a) and case 2 (b).	135
C.1	Experimental scheme relative to the tower displacement measurement.	137

List of Tables

2.1	NREL wind turbine parameters. [Jonkman, 2010]	33
3.1	DIC hardware parameters	61
3.2	DIC analysis parameters for rigid body translations	62
3.3	DIC analysis parameters	71
4.1	DIC hardware parameters	81
4.2	DIC analysis parameters	82
4.3	Simulation parameters	97
4.4	Pi Camera properties . [Arducam, 2020]	99
4.5	DIC hardware parameters.	100
5.1	DIC hardware parameters.	105
5.2	Turbine parameters.	106
5.3	DIC analysis parameters	110
5.4	Results for the measurement of the second natural frequency.	116
C.1	Experiment parameters	137

Chapter 1

Introduction

Summary

This chapter aims at introducing the context of the thesis and presenting the scientific issues that will be addressed in the following chapters.

1.1 Introduction to Wind Energy

The use of fossil fuels since the industrial revolution as a source of energy has led to the release of large quantities of greenhouse gases into the atmosphere. The concentration of these gases has resulted in an increase in the average temperature on the globe, which in the long term, if nothing is done, will have disastrous consequences. The end of the 20th century and the beginning of the 21st century marked a growing awareness of the world population with regard to global warming. Worldwide political decisions were taken to limit global warming, the first emblematic step in this fight was the ratification of the Kyoto Protocol in 1997 by 196 countries around the world [UNFCCC, 2009]. The main point of the agreement was to reduce carbon dioxide emissions. In this context, the sovereign states around the world undertook to develop so-called renewable energies in order to substitute them for fossil energies such as coal, oil or gas. Electricité De France, the historic French company and now the leading European producer and second largest producer in the world, has significantly invested in the development of low-carbon energy worldwide. Wind power is one of the major components of the energy transition alongside nuclear, hydraulic and solar power. EDF holds nearly 10 GW of wind power capacity worldwide through its subsidiary EDF Renewables [EDF-Renewables, 2020].

A wind turbine is a device that transforms the kinetic energy of the wind into electricity by passing through a mechanical converter. There are two types of wind turbines: horizontal and vertical axis. The first ones are the most widely used industrially. Several components make up a wind turbine as shown in Figure 1.1.

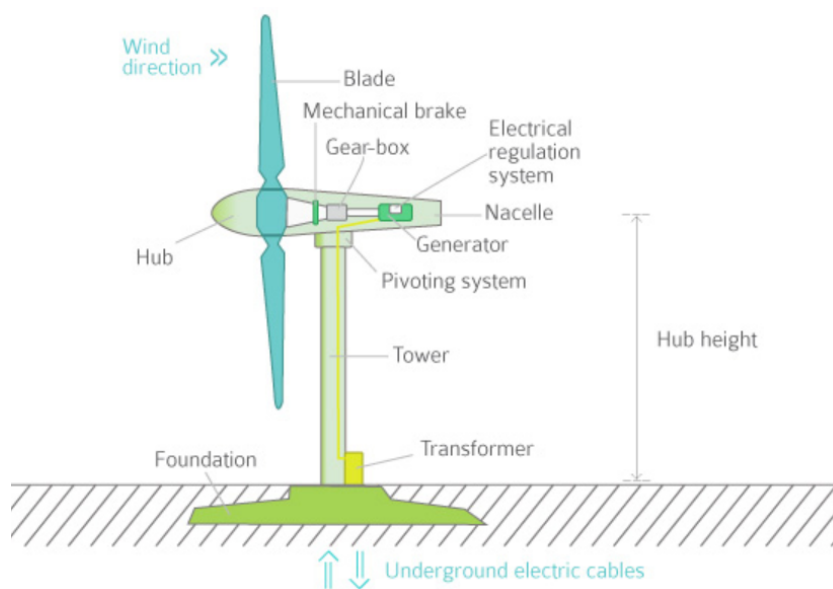


Figure 1.1: Schematic view of an onshore wind turbine [Futuren, 2020].

First, the rotor, which generally consists of three composite blades attached to a hub. There are upwind and downwind rotors, much less common due to poorer performance results. The rotor axis is always along the wind direction to take full advantage of the rotating blade profile. This rotor is

linked to a nacelle, which contains the whole chain of conversion of the mechanical energy from the rotor into electrical energy. This nacelle pivots with the rotor to face the wind thanks to continuously collected anemometric data. The orientation of the rotor is updated, usually every 30 seconds, by means of a Supervisory Control And Data Acquisition (SCADA) system [Yang and Jiang, 2011]. This system allows continuous data storage and feedback control strategies. The assembly is based on a conical tower with a circular cross-section made of steel. The different circular parts of the tower are bolted and welded together. Finally, the tower is built on a concrete foundation. The turbine electricity generation depends on the wind conditions. The power profile is separated into three phases:

- Below a particular wind velocity threshold, the turbine does not produce energy and the rotor remains motionless.
- When the wind velocity exceeds this threshold, the lift force acting on the blades is sufficient to induce rotor rotation. The turbine starts to produce energy. The rotation velocity increases with that of wind and at some point the turbine reaches a plateau of nominal production level.
- When the wind outreaches the security threshold, the turbine stops and is automatically placed in emergency stop position.

The power curve of a Vestas V90 turbine is presented in Figure 1.2. It can be noticed that the power production is maximum for a wind velocity of 15 m/s.

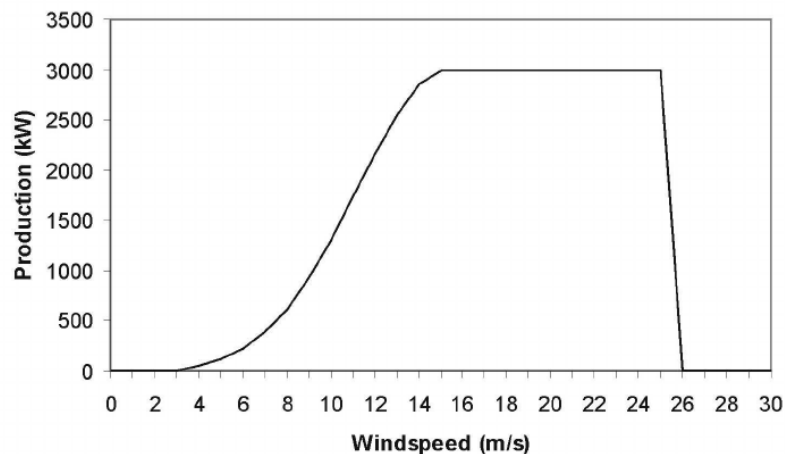


Figure 1.2: Production curve of a 3MW Vestas wind turbine [Harrison et al., 2008].

The choice of turbine type depends on site wind conditions, and the landscape according to the standards [IEC, 2005].

1.2 Industrial context

In Europe, the first onshore wind turbines with a capacity of 20kW were installed in 1982 [Carlin et al., 2003]. Since then, the power of the machines has continuously increased and the market for wind turbines has been growing both onshore and offshore. In Europe, electricity from wind power has reached 14.5% of total electricity production from all sources [EWEA, 2019]. However, the ageing of onshore wind farms now becomes a concern. Wind turbines are designed to last 20 years. Currently, it is estimated that 15% of the European wind farms have reached at least 15 years of operation [EWEA, 2019]. This observation leads to several issues. The first one concerns the operations and maintenance actions to certify structural integrity until the end of the planned operating period. The older the turbines, the more acute these concerns. The second one, which is directly related to the former is about the wind park future. Park operators have several choices:

- It may be decided to dismantle the old machines and replace them with new, more efficient ones. This choice makes sense, as long as technological innovation makes it possible in terms of gains.
- A hybrid solution is repowering. This option involves keeping the foundations and the tower of the wind turbine, and only replacing the nacelle and the rotor. These elements are the most expensive and the most subject for technological innovations.
- The last solution is to extend the service duration of the parks.

As far as technological innovation is concerned, there is a continuous increase in the power of the turbines and therefore in the size of the towers and blades, as shown in Figure 1.3. Nowadays largest turbines reach 10MW, General Electric already announced the production of the Haliade-X 12 MW model. In the next ten years, capacity is expected to reach 15 MW [Wiser et al., 2016].

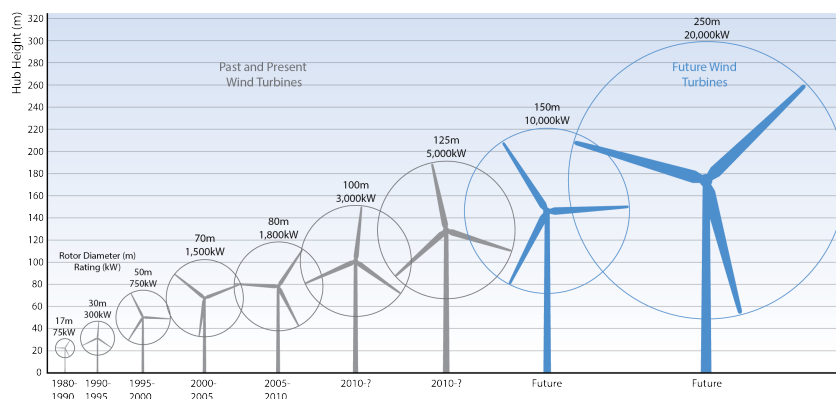


Figure 1.3: Expected wind turbine hub height growth [Wiser et al., 2016].

However, the deployment of larger turbines on land is restricted for several reasons in the French case:

- Laws relating to visual and noise pollution.

- Lack of wind strong enough inland to make it profitable to install larger turbines.
- Military restrictions on the flight of combat helicopters, for instance.

It should be noted that the cost of a wind turbine is important, especially at the initial investment level. In 2010, the National Renewable Energy Laboratory estimated the Capital Expenditure (CapEx) of an onshore wind turbine to be 1970 € per KW [Tegen et al., 2012]. In 2018 this cost dropped to 1350 € per KW [Stehly and Beiter, 2020]. Thus, for a 2 MW wind turbine, the initial investment is in the range of about 3 to 4 million €. This amount covers the turbine price, the installation costs, and the electrical connection to the grid representing about 70% of the total cost over the turbine lifetime. The remaining 30% is associated with operation and maintenance costs. The nacelle is the most expensive component of a turbine, accounting for 25% of the price, followed by the rotor for 20% and the tower for 15%. These figures are summarized in Figure 1.4.

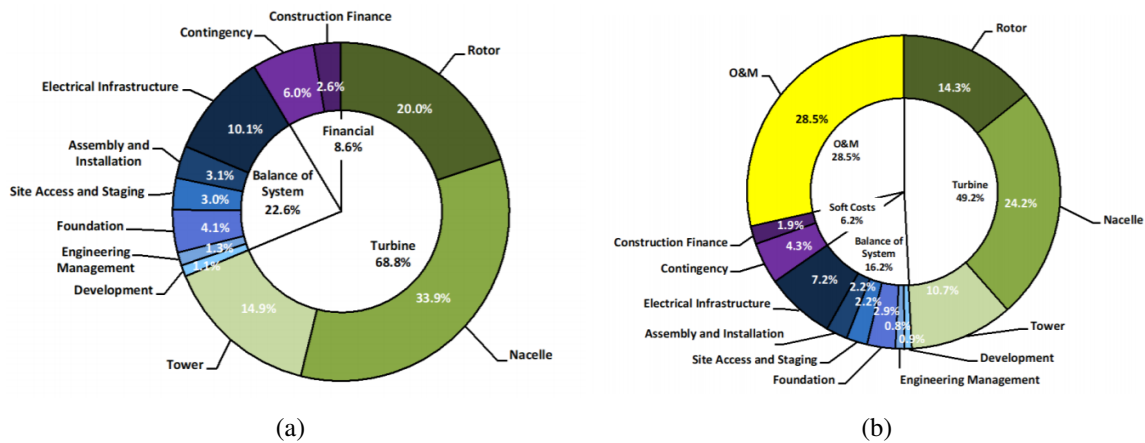


Figure 1.4: CapEx (a) and Levelized Cost Of Energy (LCOE) (b) for a wind turbine in 2018 [Stehly and Beiter, 2020].

The solutions that enable to certify the structure integrity will help to lower operations and maintenance costs. The repowering and extending park exploitation solutions would also rely on these methods to estimate park residual lives.

1.3 Wind turbine tower lifetime

Wind turbine providers design their structures respecting three constraints according to the standards [IEC, 2005]:

- Natural frequencies of the system have to be far away from "3P" frequency, which is the blade rotation frequency.
- For the environmental condition and the wind turbine configuration giving the most extreme load on the structure, the material has to remain in the elastic domain when considering its plasticity criterion.

- Under extreme conditions the structure must resist against buckling failure.
- Wind turbines are subjected to cyclic loads. The structures can face fatigue problems. Fatigue is the weakening of a material, caused by repetitive loads. It is a progressive phenomenon. In most of the cases of interest, fatigue concerns chiefly localized defects which may grow and become critical. If the loads applied on a structure are above a certain threshold, microscopic cracks begin to form at stress concentrators until one of them reaches a critical size and suddenly propagates.

1.3.1 Aeroelastics loads

For onshore wind turbines, the loads are almost exclusively aerodynamic due to wind-blade interaction. The tower is mainly stressed in bending and is subjected to repeated vibrations due to the variations in wind speed and the repeated passage of the blades in front of the tower. On-site meteorological studies provide statistics on wind directions and speeds over time. Usually one dominant wind direction exists, as illustrated by the wind rose of Figure 1.5 characterising a site in Switzerland [Loraux, 2018].

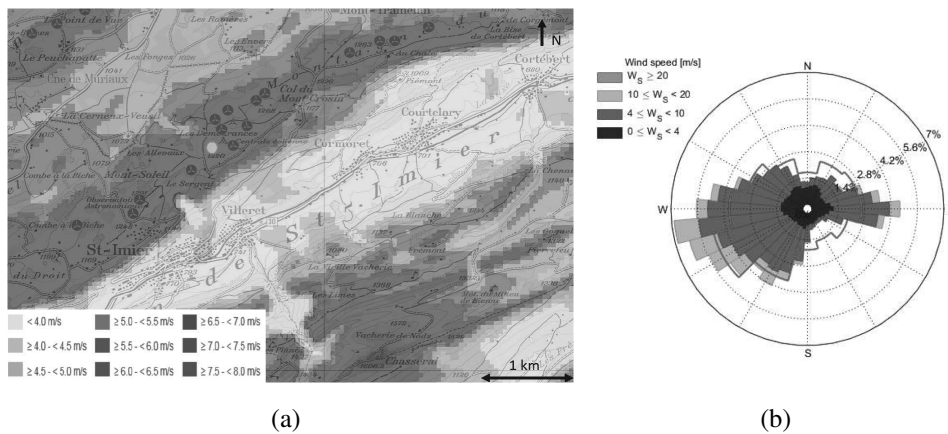


Figure 1.5: Classification of a wind site (a) and associated wind rose (b) [Loraux, 2018].

1.3.2 Calculation methods

From these wind conditions, aerodynamics loads brought back to the hub are calculated [Ingram, 2011]. The structural dynamics of the tower is modeled by a multi-beam approach [Huchet, 2018] and a particular integration scheme is used to solve the whole aero-elastic problem. The stress distribution is not uniform on a tower, due to its design, as shown in Figure 1.6.

The lifetime calculation is made considering a single wind direction and a single position (localization of highest stress). From 10 minutes of real time simulations corresponding to a single set of wind characteristics, stress amplitudes are deduced by rainflow algorithms [Musallam and Johnson, 2012]. The service duration life is calculated by means of a damage variable, using Miner rule [Miner

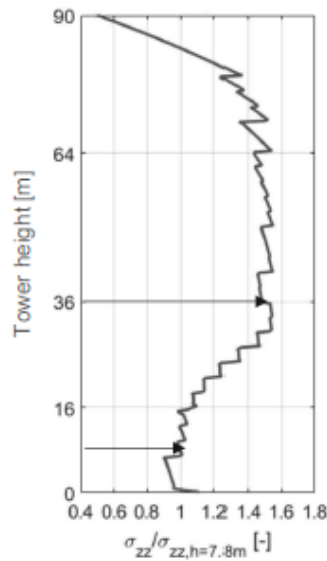


Figure 1.6: Stress undergone by a wind turbine tower under a flexural loading [Loroux, 2018].

et al., 1945] and Wohler curves [Wöhler, 1867] of the used material [Veers and Winterstein, 1998, Ragan and Manuel, 2007].

1.3.3 Associated uncertainties

Uncertainties in this overall damage calculation are due to several factors that have been listed by EDF R&D. Some are created by errors or model and methodologies limitations (systemic uncertainties) and the others are driven by statistical random variability. The whole list is:

- Variability coming from each turbulence modeling.
- Geographical variability in wind assessment.
- Statistical variability of the S-N curve.
- On-site variability affecting material like corrosion or weld over-stressing.
- Error from neglecting the change of wind direction during damage calculation.
- Error from neglecting the mean stress effect when considering S-N curves.
- Errors from controller issues noted during model validation.

All these sources of uncertainties can induce premature fatigue, this is why lifetime re-calibration strategies have been proposed.

1.3.4 Residual life time estimation and structure integrity

A small amount of works is dedicated to residual life assessment due to the recent interest in this field. Certification offices recommend to perform again aero-elastic calculations based on onsite data collected during the turbine life [Veritas, 2016, UL, 2016]. To go further, several works have been published about turbine instrumentation with strain gauges or accelerometers at specific points [Heilmann et al., 2014, Beganovic and Söffker, 2016, Rubert et al., 2019, Ziegler et al., 2018]. By precisely estimating the stresses experienced by the tower at several locations while correlating these measurements with anemometric data, statistics on the expected damage to the tower should be more accurate. In particular, Loraux's work [Loraux, 2018] studied a wind turbine instrumented with 8 strain gauges, 3 temperature sensors and 3 accelerometers. This work has brought to light some very interesting observations about tower damage. First, the total damage, in the sense of Miner's count, is mainly due to a very low number of cycles. In this particular case, 50% of the damage resulted from less than 1.29% of the monitoring duration. For 604 days of measurement, this most damaging time amounted to about 8 days, and corresponded to storms as represented in Figure 1.7.

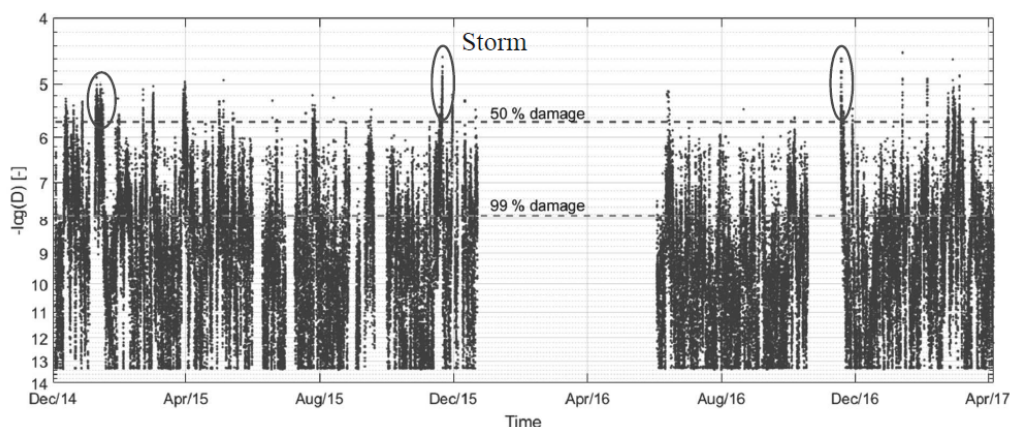


Figure 1.7: 10 minutes damage (rainflow count and Miner rule) reported along seasons in [Loraux, 2018].

It appears that depending on the method used to count the loads experienced by the wind turbine over time, the predictions of lifetimes vary from 57 to 200 years. The adjustment variables are the safety factor for the loads, the partitioning time for the rainflow stress count and the consideration on the material S-N curve. This observation shows that the structures are expected to last beyond the service life recommended by the standards. The author specifies that the studied wind turbine is on a low wind site, so the loads were low as compared to other sites. Finally, measurement drifts were observed for the strain gauges. A resetting is possible thanks to temperature measurements close to the gauges but then the measurement uncertainty is amplified by about 20%. Such works are useful to validate fatigue calculations and correction methods. However, they still present the drawbacks that a possible damage appearance due to unforeseen events is not taken into account, which leads to a lot of uncertainties to certify structural integrity.

1.3.5 Wind turbine incidents and failures

Wind turbine incidents

There are numerous publications on the compilation of statistics on incidents involving onshore wind turbines [Wen et al., 2009, Dao et al., 2019, Mabel et al., 2011, Pérez et al., 2013]. However, few are about last generation wind turbines. To be clear, here an incident does not correspond to collapse. It refers to a problem that required an intervention and induced a turbine shutdown. One of the most recent and most complete studies concerns 2270 of latest generation wind turbines, i.e. with a capacity ranging from 1 to 3 MW, and an average operating life of 6 years [Reder et al., 2016]. This study is part of a European AWESOME project. Fault occurrences according to each wind turbine sub-component are presented in Figure 1.8.

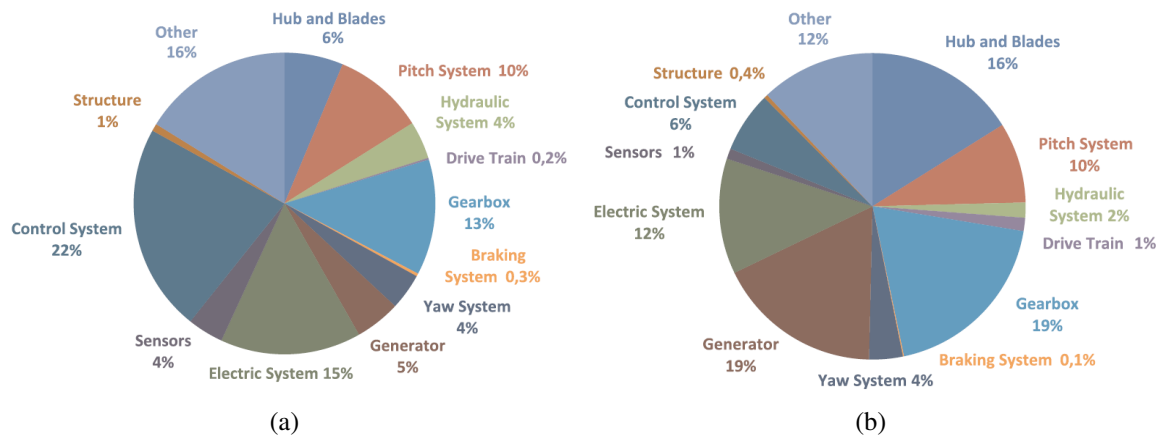


Figure 1.8: Wind turbine failure (a) and downtime (b) rates [Reder et al., 2016].

Most of them are due to mechanical or electrical problems inside the nacelle. The electro-mechanical conversion chain is complex and composed of many elements. The incidents related to the tower are associated with the index "structure". This index also includes incidents in the foundations. These incidents present a very low occurrence frequency. Regarding other reviews, the proportions are similar even with older wind turbines. The paper [Reder et al., 2016] states that most of the structural defects found occur early in the operation of the turbine and are due to malfunctions during installation. For example, this can be a faulty foundation, loose bolts or cracks in welds. However it is underlined that the occurrence of structural defects is expected to increase when the turbine age exceeds 15 years. The set of studied turbine is now very small, young, and access to data is complicated, due to park operator policies. Some publications focused on cracks found in concrete foundations or welds. In Ref. [McAlorum et al., 2018], surface cracks in an onshore wind turbine foundation have been spotted. A strategy using fibre-optic based strain-sensors to monitor deterioration and determine crack severity over 9 months is presented. It was concluded that the crack growth is acceptable and the foundation would not need repairs. The potential causes of 10 cm crack initiation at the bottom of a 5 years old tower have been studied [Lacalle et al., 2011], a picture extracted from the article is

displayed in Figure 1.9.



Figure 1.9: Photo of a crack in a weld [Lacalle et al., 2011].

Finite element simulations, with precise geometrical description of the weld joints, showed that under normal conditions the fatigue experienced by the material should not induce cracks. However, cracks do appear in the areas of highest stress. The speculated causes are multiple like slight misalignment of weld joints and underestimated loadings. It can be guessed that the presence of defects in wind turbine towers may induce unexpected structure collapses.

Turbine collapse

Very few publications are devoted to the identification of incidents that have led to the fall of wind turbines. There are two main reasons for this. First, the number of large wind turbines that have collapsed is less than 100 [Ma et al., 2019], *i.e.*, too small to be statistically significant. Second, the operating companies do not share their expert analysis of the causes of collapse. Yet, a paper published in 2019 tries to list all the cases of turbine collapse between 2000 and 2016 [Ma et al., 2019], which amounts to 64 cases. The published forensic studies are exploited. Forensic engineering is the investigation of materials, structures or components that fail or do not operate or function as intended, causing personal injury or damage to property [Noon, 2000]. The majority of forensic engineering publications come from Asia, more particularly from China, Japan and Taiwan. Most of wind turbine collapse took place in this region [Chou and Tu, 2009, Chou and Tu, 2011, Chen et al., 2015, Chen and Xu, 2016, Liu and Ishihara, 2015]. Two main types of failures have been identified in the literature. First, the breakage of the bolts causes the wind turbine to fall in several parts. This happened in Taiwan [Chou and Tu, 2011] as shown in Figure 1.10.

This type of failure may occur if the tower fastening system was not installed properly, possibly due to improper torqueing of the base or yaw system bolts. Second, the tower may collapse due to buckling at some point depending on the tower geometry, if the overturning design loads on the tower base are exceeded. For example, in January 2017, a 95-metre-high turbine collapsed near Leisnig,

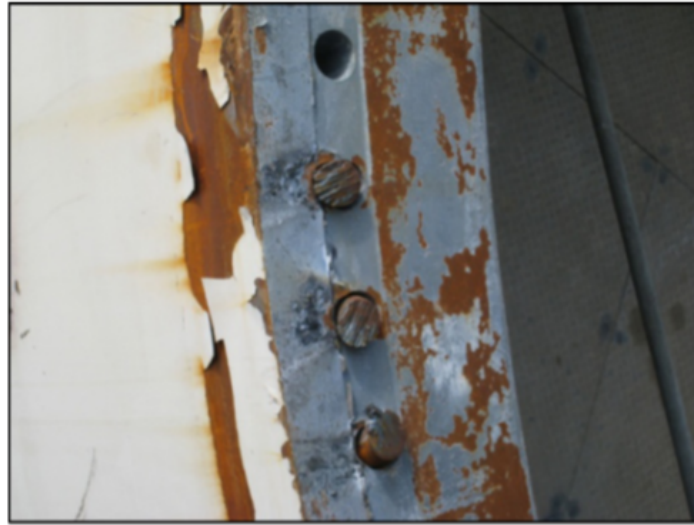


Figure 1.10: Section of a collapsed wind turbine in Taiwan [Chou and Tu, 2011].

Germany (Figure 1.11).



Figure 1.11: Collapsed wind turbine in Germany [The-Civil-Engineer, 2017].

Concerning the identified causes, in 55% of the cases, the collapse occurred due to extreme weather conditions: typhoons and storms, especially in Asian countries. The wind velocity was greater than the turbine extreme endurance limit. In 6% of the cases, bolt fatigue or excessive material fatigue was recognized as the cause of tower collapse. When a bolt breaks, the local stresses experienced by the tower increase and the load experienced by the surrounding bolts increases. This phenomena causes the premature fatigue of the other bolts to occur and a buckling-coupled pull-out can occur. Another source of tower failure is the breakage of one or more rotor blades. Under the effect of inertial forces the blade can be thrown against the tower and induce irreversible damage that will lead to its fall. The loss of a blade induces a loss of balance of the forces experienced by the hub.

These disturbances can induce higher loadings and consequently premature collapse of the tower by one of the two causes identified in the literature. It has been identified for some wind turbines in a priori good condition that buckling collapse occurred for loads below the ultimate level. Two causes were identified. First, geometrical imperfections in the tower, such as a small variation in diameter or thickness between two cylindrical parts, may have favoured buckling. Second, problems in the control system may also happen. When storms occur and the wind speed exceeds a certain threshold, around 25 m/s, the turbine stops and the blades move to the "flag" position. This position is intended to minimize the drag forces on the turbine. The yaw movement is left free so that the rotor can be aligned with the wind direction. The position of wind turbines at an emergency stop exhibited vital importance on structural failure. Due to the change of wind direction during typhoon impact, a stop position once structurally favourable may result in significant increases of wind loads to the turbine when the prevailing wind direction changes. Then the buckling load may be reached [Chou et al., 2018]. More locally in France, only two collapses of large wind turbine have been reported. The first took place at the end of December 2017, on a park in the city of Bouin. The picture of the collapsed wind turbine is shown Figure 1.12. It was a 62 m high wind turbine with a total weight of about 260 tons.



Figure 1.12: Collapsed wind turbine in Bouin, France [Parisien, 2018].

A series of technical incidents occurred during a storm, that resulted in poor blade and rotor positioning during high wind events. The wind turbine upper part was torn off 5 m from the ground at a weld section. We did not have access to the report concerning the fall of this wind turbine because it did not belong to EDF. This wind turbine was 15 years old. In view of the uprooting and age of the turbine, it is conceivable that a crack was present following the coalescence of defects due to fatigue at weld location. The sudden propagation of the crack would then have taken place under such violent loads. Slight local buckling is also seen on the images. It should be noted that, to the author's knowledge, no case of crack propagation as a cause for collapse has been reported in the literature. The second fallen wind turbine in France belonged to a park near the town of Guigneville, the tower was 90 m high. The incident occurred in 2018 following a failure of the rotor brake. The rotor then

ran out of control, which caused the bolts between the first and second floors of the tower to break, as shown in Figure 1.13.



Figure 1.13: Collapsed wind turbine in Guineville, France [France-3, 2018].

Summary

Studies of incidents resulting in turbine shutdowns show that most of the problems stem from the nacelle's electro-mechanical conversion chain, not from the structure (either foundation or tower). However, the presence of a defect in the nacelle will in most cases not lead to turbine collapse, whereas in the tower the potential criticality of a defect is much higher. The study of fatal accidents that led to the fall of turbine towers has enabled several conclusions to be drawn. Three failure modes have been identified. First, bolt breakage at the flanges, which causes the upper part of the tower to tear off. Second, local buckling of the tower due to excessive flexural loading. The last mode of failure is related to crack propagation at a weld. Tower failures have mainly taken place in areas where extreme typhoon and storm conditions can occur. It is during very strong wind events that wind turbines collapse. In half of the cases identified and documented by post-mortem analysis, the climatic conditions were such that the loads on the towers were above the permissible limit. In the other half of the cases these particular meteorological parameters go hand in hand with a malfunction of a turbine part. The first recorded problem was premature fatigue of the bolts at the flanges. This problem can be fixed by inspecting the bolts for proper torque at regular and close intervals. The other types of failures involve the nacelle rotor assembly. This can be the loss of a blade that causes the tower to become unbalanced, a brake problem that causes the rotor to overspeed, or a control problem when the turbine is in the fail-safe position. The last identified issue is the appearance of cracks at welds due to premature fatigue. It can be envisaged that with the increasing competition between the different actors of wind energy, the resulting optimization of the structures, the appearance of rotors of greater power, that the occurrence of crack fatigue cases will increase with time. Even with more stressed structures, fatigue is not a problem under nominal operating conditions. However, the presence of defects coupled with turbine malfunctions or extreme conditions make structures vulnerable. It is therefore essential to develop methods to monitor structure health over time.

1.4 Wind turbine tower health estimation

The health control of large structures is a vast research field [Farrar and Worden, 2007]. The objective of the implemented techniques is to detect the appearance of a defect before it becomes critical to the structure from the point of view of its integrity. They can be divided into two groups. The major points of differentiation is whether or not the technique is automatic, autonomous and continuous. First, Non Destructive Testing (NDT) [Lakshmi et al., 2013] techniques gather methods which consist in checking at regular time intervals the structure as a whole to detect defects. The Structural Health Monitoring (SHM) Techniques [Farrar and Worden, 2007] consist in continuously gathering information about the studied structure from several sensors and automatically detecting health indicator shifts synonymous of damage appearance.

1.4.1 Non destructive testing

First, the simplest and cheapest technique to apply is the visual inspection of the structure. Generally, in the wind energy industry, such inspections are carried out annually from inside the tower by qualified technicians. The main goal is to detect corrosion within the structure, but the search for cracks is also part of the work. The main drawback of this technique is that it is not exhaustive, since only the interior of the tower is examined. The defects may be not visible under the paint or when they are located on the structure outer surface. To the author's knowledge, there is no publication on the development of original NDT methods for turbine tower integrity qualification. Publications on the subject related to the wind energy industry focus on defect characterization for blades [Raišutis et al., 2008, Galappaththi et al., 2012, Lakshmi et al., 2013, Jasinien et al., 2009]. However, these methods are well used for tower inspection by wind farm operators. The industry mainly focuses on welds and bolts. An example of robot inspection is shown in Figure 1.14.



Figure 1.14: Control of a wind turbine tower thanks to ultrasound waves [Force-Technology, 2020].

In the case of bolts, following feedback from accidents that have occurred due to excessive bolt fatigue, recommendations have been made to check bolts regularly. If a bolt no longer meets the

torque resistance criterion, it is replaced. Checking welds relies on different techniques that mostly are magnetic particle testing, ultrasound and eddy currents. Magnetoscopy is based on the detection of discontinuities, opening on the surface or down to a few millimetres deep [Tehranchi et al., 2011]. This method is only applicable on ferromagnetic materials and on uncoated surfaces. The principle of ultrasonic inspection consists in emitting and propagating an ultrasonic wave in the part to be inspected, then collecting and analysing the wave at the end of its interaction with the material [García-Martín et al., 2011, Beard and Lowe, 2003]. The receiver will record the echoes coming from the reflection or diffraction caused by obstacles encountered in the wave path. These obstacles can be defects, interfaces of different materials of a part or the surface of the part to be inspected. This method requires to be in contact with the part to be tested and to use a gel or water type coupler in order to allow the propagation of the ultrasonic waves. It is therefore necessary to have a clean and regular surface. To check the welds on wind turbine masts, it is compulsory to remove the paint. The ultrasonic technique has the advantage of being able to identify defects in the underlay (invisible to the naked eye) of the structure. The latest possible technology is eddy currents testing [García-Martín et al., 2011]. This method is based on the flow of currents induced in an electrically conductive material and allows, as in ultrasonic testing, for the detection of underlying defects. Compared to ultrasonic testing, this technique has the advantage that no surface preparation of the tested material is required. However, the disadvantage of this technique is that it is not able to inspect sheets with a thickness of more than a few millimetres. The development of pulsed eddy current methods makes it possible to overcome this limitation, but this technology remains very expensive [Sophian et al., 2017]. It is possible to detect cracks in welds for few centimeters large specimen. However, the knowledge of the material properties and the defect signature are mandatory, hence it needs calibration. These methods have the disadvantage that their use involves stopping the machine for a long period of time because it is forbidden to operate in or near a functioning turbine. Moreover, their cost can be prohibitive if one wishes to check an important part of the structure in an exhaustive way: these technologies are complex and require the preparation of the surfaces mentioned above, and especially the full-time work of specialised technicians. Thus, the NDT strategy will rather be reserved for situations where there is a suspicion of damage, localized in space and time, in order to carry out a finer diagnosis and allow the alert to be disqualified or remedied. Then there is a need for the implementation of automated continuous structural monitoring, if possible with low cost technologies, allowing the centralization of wind farm control.

1.4.2 Structural Health Monitoring

Health monitoring of structures aims at giving, at each moment of the structure life, a diagnosis of the state of all its components [Farrar and Worden, 2007]. The goal may be to trace back to an equivalent damage, and for example to recalibrate the tools for predicting the fatigue life of the component [Rytter, 1993]. The field of SHM applied to wind turbine towers has given rise to numerous publications. Detailed reviews summarizing the proposed scientific methods are available [Wymore et al., 2015, Martinez-Luengo et al., 2016].

Most publications in the field have focused on damage detection by frequency tracking [Devriendt et al., 2014, Smarsly et al., 2013, Bassett et al., 2010]. A measured eigenfrequency variation of the structure corresponds to the occurrence of a defect. The interesting aspect of this technique is that the measurement of natural frequencies by accelerometers is fully mastered by the industry. However, these techniques have several disadvantages. First, considering that the sought damage is the initiation of cracks, the expected impact on the first eigenfrequencies, those usually measured, is minimal before this damage develops in a catastrophic way and requires measurements at very low noise levels, which is delicate in a context of random loadings [Bang et al., 2012]. In addition, variations in the inertial properties of the structure due to the environment can distort the measured eigenfrequency variations. One way to deal with these difficulties is to search for information in the non-linear vibration content, for example by wavelet analysis [Bassett et al., 2010]. These analyses also provide information on the spatial vibrations of the structure. However, these techniques are also subject to certain weaknesses, such as the appearance of interference terms in the time-frequency plane caused by noise. Most of the publications dealing with this method demonstrate its feasibility on numerical simulations of situations with major defects. Even with a high number of sensors, these methods do not enable to detect precisely the defect localization and categorize it. Few studies have focused on techniques that do not exploit vibrometric data. For example, one publication suggests placing strain gauges at regular intervals around hot spots of the structure (areas of largest strains) in order to detect localized strain gradients that would correspond to the presence of cracks [Benedetti et al., 2011]. The drawback of this technique is that a very high density of sensors is required to detect any crack occurrence. The radius of influence of a crack is very small, its impact on plane strains inversely decreases with the square root of the distance to the defect. In addition, strain gauges may suffer from measurement drifts over time. They can be corrected but with increased uncertainties [Loroux, 2018]. Other publications focus on the use of fibre-optic sensors, which also provide access to local strains but are also sensitive to temperature variations [Bang et al., 2012]. In conclusion, the common disadvantage of all these techniques is that they extrapolate a structure state of health as a whole from local information. Potentially fatal defects may go undetected. Moreover, neither the defect localization identification, nor its categorization, are possible with many of proposed methods, which is problematic for structures that can reach up to 100 m in height.

1.5 Scientific issues

As wind farms age in the whole world, turbine integrity certification is becoming a major industrial issue to optimise asset management and guarantee the safety of the technicians working on site. In particular, farm life extension and repowering are being considered to amortize costs and make wind energy more competitive. The tower is a critical component since a fatal incident cannot occur under any circumstances. The calculation of the service life of wind turbine towers is based on damage calculation in the Miner sense using Wohler curves. The standards require that the service life exceeds the operating life, which is currently 20 years [IEC, 2005]. This form of calculation remains approximate and should require recalibration from site data for precise estimation. Yet, the current tower

designs are normally not to be questioned thanks to sufficient margins. At first glance, the life span of a wind turbine tower is not a problem. However, structural incidents have already been reported, especially bolt breakage, corrosion or cracks in welds. This last type of incident is principally due to premature fatigue induced by misalignment of welding joints, underestimated loads or stress concentration due to a faulty weld cooling process. Even if their number is very small in comparison to the number of installed turbines, towers have already collapsed around the world. Collapses almost never occur at nominal operating conditions, but always under particular wind conditions. It can be guessed that a crack presence will then make it much more susceptible to collapse. Both induced failure modes are premature buckling and fatal crack propagation. From post-mortem analyses both causes can be assumed: buckled areas as well as cracked parts are often present. Then, several questions arise:

How is the wind turbine tower integrity affected by the presence of a crack-like defect ? What is the worst corresponding failure mode ?

Chapter 2 aims to answer that question. First, it will be studied how a crack-like defect affects the buckling resistance of a wind turbine tower. Second, the conditions needed for critical crack propagation will be addressed. Both results will be confronted and a conclusion about the worst failure mode will be made. Simulations of rotor misalignment with respect to the wind direction will be conducted to illustrate severe loading under storm conditions. Then, the interest of monitoring the health of the wind turbine structures will be stressed.

Concerning structure monitoring, two types are available on the industrial market: non destructive testing and structural health monitoring techniques. The first ones are full-field but expensive, complex to use and not autonomous. The second ones are autonomous but are expensive and not full-field. The cost/benefit trade-off is an obstacle for widespread wind turbine tower monitoring. The motivation behind that is that the occurrence of incidents in turbines is concentrated in the rotor nacelle assembly. Therefore, as highlighted in Ref. [Wymore et al., 2015], the structure monitoring is nowadays motivated by optical methods to detect damage because they are non-intrusive and low cost. The suggestion made in the review is about damage surface detection, like corrosion. These methods have been explored for turbine blades [Wang and Zhang, 2017], but nearly no research has been carried out for towers. Within the exposed framework, Digital Image Correlation [Sutton et al., 2009, Hild and Roux, 2012b] (DIC) is the technique chosen to develop new methods that would allow the limitations of previously cited ones to be overcome. DIC provides a full-field measurement in terms of displacement, the exploitation of which can allow for a more direct interpretation of the nature of any mechanical damage observed [Hild et al., 2015]. Thus the second question that will drive the thesis is:

How can DIC be used to assess the turbine tower health ?

Two routes are followed: identification at the local scale with a material vision, and identification at the global scale of the structure.

For the first approach, a planar sample is considered whose dimension is much smaller than a wind turbine tower on which a defect of length l is present, the displacement field u under mechanical stress between two instants is

$$u = u_{meca} + \delta_u \quad (1.1)$$

where u_{meca} is the displacement field due to the mechanical stress, and δ_u corresponds to the disturbance associated with the presence of the defect. At this scale, the problem is considered bi-dimensional due to the very small thickness of a cylindrical tower. In the following r corresponds to the distance from the defect. At the vicinity of a crack tip, when $r \ll l$, the displacement influence is

$$\delta_u \propto r^{1/2} \quad (1.2)$$

When the distance from the defect increases and the condition $r \gg l$ is met, one can approximate that

$$\delta_u \propto l^2 r^{-1} \quad (1.3)$$

according to Eshelby's perturbation theory [Eshelby, 1957]. Thus, the relative perturbation reaches a maximum when $r \approx l$, which justifies to develop a damage detection method at this scale. In the following it will be called the "mesoscopic" approach. The second approach takes place in the mechanics of materials framework. The tower is modelled by a beam, so the studied environment is one-dimensional. At this scale, damage is homogenized over a complete section of a tower and represents a loss of lateral moment of inertia [Marante and Flórez-López, 2003, Marante et al., 2012]. When damage is concentrated at one point, it implies a discontinuity in the rotation field, such as a hinge. The influence on the displacement field is comparable to a lever arm, which implies that the perturbation will be proportional to the distance from the defect

$$\delta_u \propto r \quad (1.4)$$

This explains why, for this approach, the distant and global vision is important because of the proportionality in r . In the following it will be referred as the "macroscopic" approach.

Chapter 3 will present the DIC principle and develop the scientific concepts related to this field that are used in this work. More particularly, instantaneous and spatio-temporal DIC will be presented. A work about the *optimal* DIC framework with N channels will also be addressed, with the underlying objective to lower measurement uncertainty.

Chapter 4 is devoted to the mesoscopic approach. First, the aspects related to the industrially deployable device will be exposed. Then, the automatic damage detection algorithm using DIC developed during this thesis will be discussed.

Chapter 5 deals with the theory for damage detection at the macroscopic scale. An innovative method of wind turbine tower modal analysis by DIC will also be exposed.

For chapters 4 and 5, the uncertainties of damage detection will be compared to displacement

perturbation modeling to conclude about the detection feasibility.

Chapter 2

Simulation of a wind turbine tower failure

Summary

In this chapter, finite element calculations are carried out to determine the wind turbine tower worst failure mode with a presence of a crack. The chosen tower type is based on an academical model. First, the theory about buckling and the calculations performed are exposed. Second, theory and calculations about a critical crack propagation are adressed. Then, a comparison between both failure modes is made. Eventually, simulations of rotor misalignment with respect to the wind direction are conducted to illustrate severe loading under storm conditions.

2.1 Introduction

Field studies have revealed that cracks could be present along the welds at material interfaces. They may originate from high residual stresses induced by the welding process, or over-stressing due to non-optimized weld joint design [Chen and Xu, 2016, Lacalle et al., 2011]. Post-mortem observations of collapsed wind turbine towers revealed two characteristic failure modes: flexural buckling of the tower and crack propagation on the tower tensile side (Section 1.3.5). It is difficult to establish, when the tower is initially cracked, which is the primary cause of the turbine fall. On the one hand, a crack can influence buckling in two ways, namely, local weakening caused by the crack lowers the critical load, and if the crack propagates under heavy loads, the buckling resistance can drop and cause the tower to fall prematurely. On the other hand, buckling of the tower may induce local overstressing and cause the propagation of an initially present crack. In this chapter, the objective is to determine which is the most critical mode of failure for a wind turbine tower in the presence of cracks: buckling or fatal propagation? The influence of the crack, whether on the tensile or compressive side, is studied. The results are compared with those available in the literature concerning their relative influence. The second part of this chapter deals with fatal crack propagation within a wind turbine tower. The theoretical aspects related to fracture mechanics are first presented, then computations are made to determine the critical corresponding loads. Results from both studies lead to determine which is the worst failure mode for a damaged tower. In the third part, a loading case in which strong winds are coupled with a rotor axis misalignment with respect to the wind direction is simulated to illustrate a critical loading condition. For the numerical models, the numerical framework is the EDF R&D Finite Element Model(FEM) open-source code: *code_Aster* [EDF, 2017a].

2.2 Buckling of a wind turbine tower

2.2.1 Literature review on buckling

In mechanics, buckling is a geometric instability of a structure under a given load [Timoshenko, 1910, Rhode and Lundquist, 1931, Brazier, 1927]. It generally occurs on thin or slender structures and results in strong deformations of the structure due to a very small increase in load. At the onset of buckling the load is termed *critical*. The structure loses its stiffness at this point. In the structural design field it is essential to avoid bifurcation towards an unstable post-critical branch, which is synonymous with the failure of the structure. Buckling may occur in the elastic domain but may also be coupled with plastic phenomena [Gerard and Becker, 1957, Hutchinson, 1974, Bushnell, 1974, Johnson and Will, 1974], the appearance of plastic deformations inducing a local loss of resistance to buckling. The typical geometry of a wind turbine tower is similar to that of a thin cylindrical shell. Generally, when cylindrical shells are subjected to a bending moment, several effects lead to the collapse of the tube: ovalization, local buckling, and plastification [Brazier, 1927, Gerard and Becker, 1957].

Buckling of a cylinder in presence of defect

In real life, built structures are never perfect. Manufacturing defects do exist and the quantification of their influence has proven to be essential in order to ensure the integrity of structures with respect to instabilities. First, analytical solutions were proposed in order to evaluate the influence of defects corresponding to geometrical discontinuities [Hutchinson et al., 1971] in shells. The obtained results hold in the limit of very long and thin cylinders. Many experimental approaches were carried out to validate either the analytical approaches or the simulations when the deviations from the conditions of applicability of analytic solutions were encountered. The work performed in [Miladi and Razzaghi, 2014] focused on the study of axial compression of cylindrical shells with circular holes using finite element calculations. More specifically, the analysis was about the influence of the cylinder aspect ratios $\alpha = L/R$ and $\beta = R/t$. Here L designates the length of the cylinder, R the radius and t its thickness. The tested ranges of values were $1.5 < \alpha < 6$ and $125 < \beta < 1000$. The main conclusion of the study was that the factor that most influenced the critical load drop was β . The higher this aspect ratio, the greater the influence of a defect. For the largest defects the influence ranges from less than 10% for the thickest tubes to 35% for the thinnest tubes. The influence of α is much smaller. In Ref. [Yeh et al., 1999] the flexural buckling of thicker tubes ($\beta = 25$) in the presence of rectangular or circular holes was studied experimentally and by simulations. Three main conclusions were drawn from this work. First, a plastic bending on the face in compression was observed. Second, the defects had more influence on the critical load when they were on the compressive side than on the tensile side. Third, the differences between the buckling loads obtained by experiments and simulations were small, less than 5%. The influence of cracks on the critical load in compression has been studied in Ref. [Saemi et al., 2015], both experimentally and numerically. The studied shells had aspect ratio β ranging from 10 to 12. The ratio of crack size over cylinder diameter lied between 0.2 and 0.4. The influence on the critical load for circumferential cracks was of the order of 8% regardless of crack length, whereas longitudinal cracks could lower the critical load by up to 15%. These cracks were more likely to open during the compressive phase. Several techniques have been used to model buckling of damaged cylinders. In Ref. [Akrami and Erfani, 2017], it is assimilated by a particular rotational spring between the two cylinders to facilitate the calculation. The use of extended finite elements has been proposed [Nasirmanesh and Mohammadi, 2017] but the use of such elements is not possible in all finite element solvers. Last, more classical techniques are used [Saemi et al., 2015, Vaziri and Estekanchi, 2006], given that the interpenetration of the crack lips must be avoided, and contact is taken into account.

Wind turbine towers generally present thickness aspect ratio β around 100 and their diameter is about 4 m. Thus, for cracks about 10 to 50 cm, the influence on the buckling load is expected to be small, i.e. less than 10%. This assumption has to be validated by simulation. Another interesting element is to be underlined. It has been observed that the defect presence on the compressive side is more critical than on the tensile side. For cracks in compression, the simplest modelling is to use a non-penetration condition between the crack lips.

Wind turbine towers buckling

A few works have been published on the study of the wind turbine tower collapse and its modelling. Most of them were motivated by tower failures due to high winds [Chen and Xu, 2016] which sought to corroborate post-mortem observations with static finite element simulations. The studied wind turbine was 47 m high. From elastic buckling mode calculation, it was deduced that plasticity must be taken into account in the finite element simulation. Otherwise the critical loadings would be unrealistic. A stress concentration factor was used to model the bolted or welded connections of the different parts of the tower. The point where buckling occurred matched with the maximum stressed area where the material yielded. In Ref. [Dai et al., 2017], a dynamic simulation was performed. The temporal loads at the hub were obtained by aeroelastic simulation. The tower under study was 65 m high and actually collapsed during high wind events. Once again, the calculation was elasto-plastic due to the fact that the theoretical elastic buckling values led to stresses four times higher than the yield strength. Plastic hinging was observed at the site of maximum stress and this was consistent with post-mortem observations. The authors indicated that total collapse occurred less than three seconds after the onset of the plastic zone, in real simulation time, which was particularly fast. Furthermore, it was indicated that visco-plastic effects were not to be taken into account due to the material properties and deformation rates calculated after simulation. This work also showed that the loading on the wind turbine has become unsustainable due to sudden changes in wind direction. The forces related to the acceleration of the nacelle led to the collapse of the turbine. Finally in Ref. [Guo et al., 2011], a pushover finite element analysis of a 53 m high wind turbine tower was performed. The tower was progressively loaded with a transverse force until it buckled. The calculation was conducted in statics, and it was carried out post-buckling thanks to a piloting technique. In this work the influence of a very small geometrical defect on the critical load of the tower was investigated. The defect was a 25 kN preload applied to the nodes over a length representing 0.5% of the tower diameter. It was shown that the influence of the defect is of the order of a few percents on the critical load. Another work has focused on the sensitivity of the critical load to the position and shape of the inclusion of the wind turbine entrance door at the bottom of the turbine [Dimopoulos and Gantes, 2012]. It was shown that the use of stiffeners in the lower part of the tower can counteract this loss of resistance to buckling.

Summary

The buckling of cylindrical shells is a phenomenon that has been studied for a long time and is particularly well understood. In the case of thick shells, buckling by compression or bending involves plasticity, thus modelling this phenomenon is complicated due to the combination of non-linear phenomena and instabilities. However, the piloting methods developed in finite element solvers make it possible to overcome these problems and to perform these computations successfully. The impact of the presence of defects on the critical buckling load is a problem that has also been studied in the scientific literature. Experimentally and numerically it has been shown that the aspect ratio of the cylinder thickness to its radius is a prevalent for the defect sensitivity. The following conclusion has been often drawn: the greater this ratio, the greater the loss of resistance to buckling. Wind turbines

are cylinders whose diameters and thicknesses vary with height. However their aspect ratio remains similar and they can be considered as thick shells. Thus the expected critical load drop is of the order of a few percent for circumferential cracks of few tens of centimetres. These wind turbines are stressed in flexure and these orders of magnitude are valid if the crack is located on the compressive side. When the crack is situated in the tensile side, its influence is almost negligible. To model buckling with a crack on the compressive side, the contact between the crack lips must be considered in order to avoid interpenetration.

2.2.2 Buckling simulation with an academic turbine model

Some results presented in this section have been published [Capaldo et al., 2020].

Case presentation

To illustrate buckling of a wind turbine tower in the presence of defects an academic tower model is chosen, and called NREL (inspired from National Renewable Energy Laboratory) in the following. The geometrical parameters of the tower are presented in Table 2.1. The geometry of this tower has mainly been used for offshore wind turbine applications [Jonkman, 2010], and particularly for the comparison and validation of hydrodynamic codes [Jonkman and Musial, 2010, Popko et al., 2012, Robertson et al., 2017]. For the NREL tower, assuming a geometry with no thickness or diameter jump, the scaled parameters range, from 29 to 45 for β , and from 102 to 111 for α . Other wind turbines are generally thinner than the NREL prototype, but the orders of magnitude for the geometric aspect ratios are close. The tower is considered to be a truncated cone. The thickness varies linearly

Table 2.1: NREL wind turbine parameters. [Jonkman, 2010]

Size of tower	87.6 m
Diameter: from base to top (linear variation)	6-3.87 m
Thickness: from base to top (linear variation)	27-19 mm
Young's modulus	210 GPa
Poisson's modulus	0.3
Yield stress	355 MPa
Hardening tangent modulus	8.4 GPa
Density	8000 kg/m
Nacelle mass	297 tons
Nacelle COG coordinates from tower axis	-0.579, 0.0, 87.6 m

from the base to the top. The welds and flanges are not taken into account for the sake of simplicity. This is a limit of the model because the discontinuities can induce premature buckling, and then the critical load may be overestimated. However it has been shown in bibliographical review 2.2.1 that for such type of cylinder a defect or discontinuity has very small influence. The Rotor Nacelle Assembly (RNA) is simply modeled as a point mass. The material is a J0355 steel [Seitl et al., 2019] and concerning the plasticity behavior a simple linear isotropic hardening model with elastic threshold is chosen. The thrust force of the RNA is modeled by a transverse force applied to the top of the

tower. The distributed drag pressure over the tower is neglected in order to simplify the analysis and the conclusions in terms of critical loads. However, it is to be noted that this drag pressure is an important contribution for high wind speed. The analysis is of *pushover* type: the tower is subjected to a constant vertical loading and a variable lateral one up to the post-buckling regime.

Buckling of a wind turbine tower with no crack

Only half of the tower is modelled, exploiting its symmetry. The choice is for 3D hexahedra with 20 nodes to better represent the gradients in the thickness. Sub integrated elements are considered in order to avoid numerical locking related to the incompressibility behavior of plasticity [EDF, 2011]. A refinement in the direction of the tower axis is considered where buckling occurs since the gradients are stronger when instability is reached as shown in Figure 2.1. The maximum side size of an element

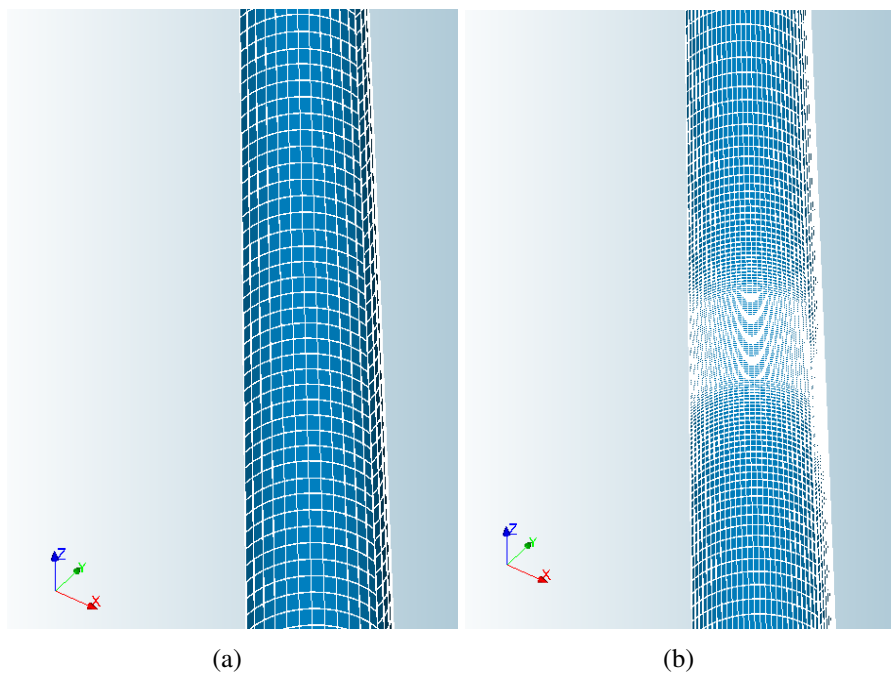


Figure 2.1: Tower without (a) and with refinement (b).

in this zone is 10 cm. The elasto-plastic calculation in large strains is very strongly non-linear. To carry out such a calculation, a quasi-static iterative Newton algorithm is used. At each step, the transverse force applied to the tower increases. The buckling of the tower causes a loss of rigidity which leads to a non-monotonic response of the loading-displacement function. At some point, the problem becomes singular. To overcome such a computational problem, it is therefore necessary to complete Newton's algorithm with a "piloting" method [EDF, 2013] in order to observe the post-critical behavior of the buckled tower. The external force at the tower top is driven thanks to the "elastic prediction" method. It imposes that at each time step of the quasi static scheme, at least one integration point deviates from the elastic regime. The piloting method ensures that during the buckling and post-buckling period plasticity increases at each time step, at least in one element [EDF, 2013]. Figure 2.2 shows the force-displacement history at the tower top during the buckling and post-

buckling processes. They are illustrated with snapshots of tower deformations at different steps in Figure 2.3.

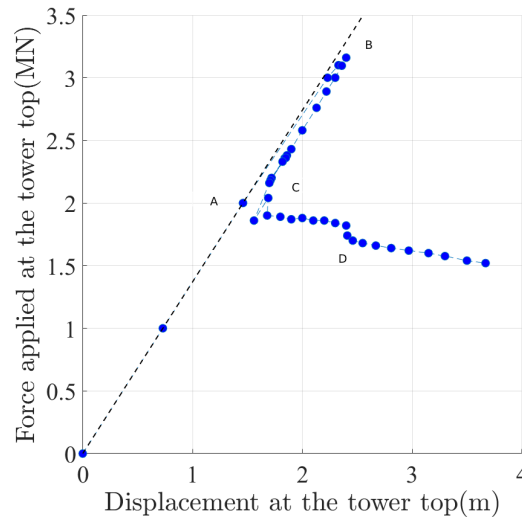


Figure 2.2: Applied force versus displacement at tower top.

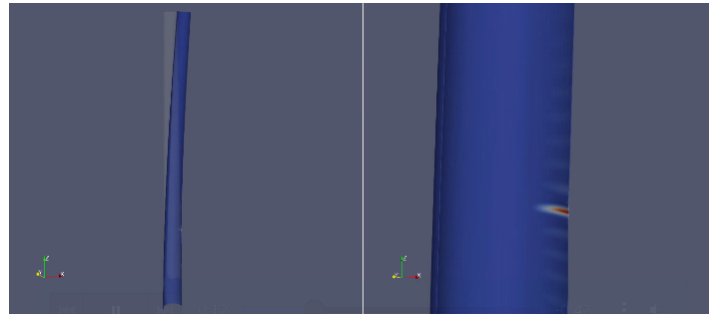
Several regimes are recognised during the buckling process:

- At point A: From a macroscopic point of view the tower behaves in an elastic regime, even though plasticity appears.
- At point B: This is the buckling point. A pattern of wavelets appears on the structure, characteristic of instability due to buckling.
- At point C: The tower exhibits a large loss of stiffness, this is called the snap-back regime.
- At point D: This is the post buckling regime and the tower slowly collapses.

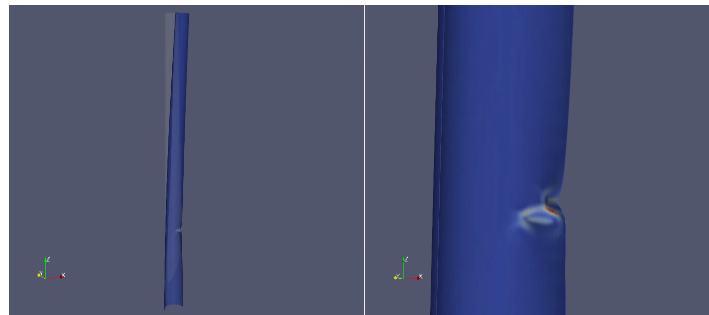
A picture of a post-buckled tower is shown in Figure 2.4. Similarities are observed between the real buckling zone shape encountered with post-mortem observations and the one obtained by simulation. From an industrial point of view, the full post-buckling simulation is not necessary. Only knowledge of the critical load is sought. However, observations like the presence of wavelets during the loading process and the final buckling zone shape encountered enables the simulation to be deemed physically acceptable.

Buckling of a tower with a crack

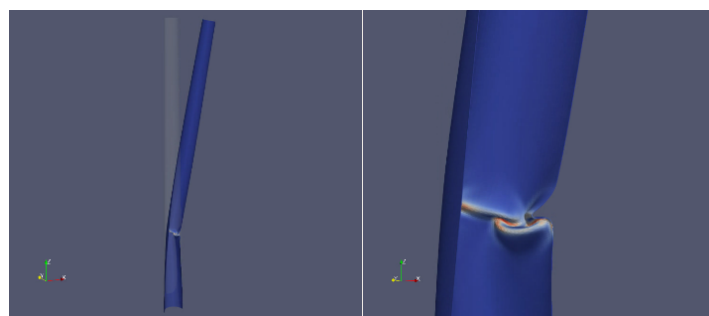
The influence of cracks located in tearing and compression sides is studied hereafter. For the latter, a contact condition must be taken into account to avoid crack lips interpenetration, and more precisely a penalization is chosen to enforce this condition. The contact is frictionless, this allows to remain conservative from an energetic point of view. In *Code_Aster*, it was not possible to couple piloting and contact methods. Thus, the buckling and post-buckling regime cannot be simulated. Another



(a)



(b)



(c)

Figure 2.3: Tower deformation profiles at step B (a), step C (b) and step D (c) . The displacement is magnified $\times 1.5$ and the colors highlight the plastic strains.



Figure 2.4: Example of wind turbine tower failing by buckling. [Jay et al., 2016]

way to assess the critical load is to iteratively reach the point where the problem becomes numerically singular, which signals the onset of buckling. More precisely, the tangent operator is calculated at each iteration, if one of its eigen value becomes negative it means that the bifurcation point has been reached. The considered cracks are horizontal and through, ranging in size from 10 cm to 40 cm, placed at different heights. Cracks on the tensile side are also subject to the risk of propagation in opening mode. Critical crack propagation is studied in the following section, for this case only, the influence of the loss of lateral stiffness induced by crack opening on the buckling load is observed. A crack, considered as a surface, is introduced into the mesh thanks to Z-cracks software. Details about the algorithms can be found in Ref. [Chiaruttini et al., 2013]. The resulting meshes are presented in Figure 2.5. A convergence study has been carried out to estimate the needed local refinement to fully capture the perturbation in the buckling process induced by the crack. The needed maximum refinement is about 10 cm. Figure 2.6 shows the plastic strains for a 3 MN load on the compressive side with or without the presence of a crack. An amplification of the strain is observed in the vicinity of the crack. In Figure 2.7 the influences of the crack length and its vertical position are investigated. First, the crack is placed at the maximum stress position: 25 m from the ground. While the critical load drops with the crack length in the compressive side, placing a crack in the tensile side seems to have absolutely no influence. It is even noted that the critical load is slightly higher (0.1%): the difference in refinement and local orientation of the mesh due to the crack inclusion is the most likely cause. Several heights have been tested and the influence does not change. The vertical position has an influence for a crack in the compressive side: outside the maximum stress area its influence vanishes. It is explained by the fact that buckling occurs always at the same spot. These results are in agreement with what has been published in the literature on the subject: the flexural buckling of a cylindrical shell is influenced by cracks present on the compressive side only. This influence remains small, less than 10% due to the high relative thickness aspect ratio. To continue this work it could be interesting to integrate tower geometrical feature, like bolts, welds and the door at the tower bottom.

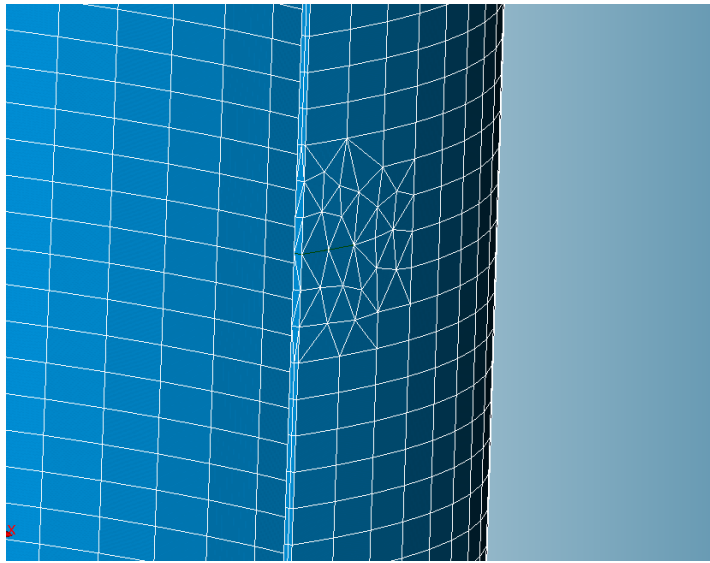


Figure 2.5: Zoom around the mesh of the crack.

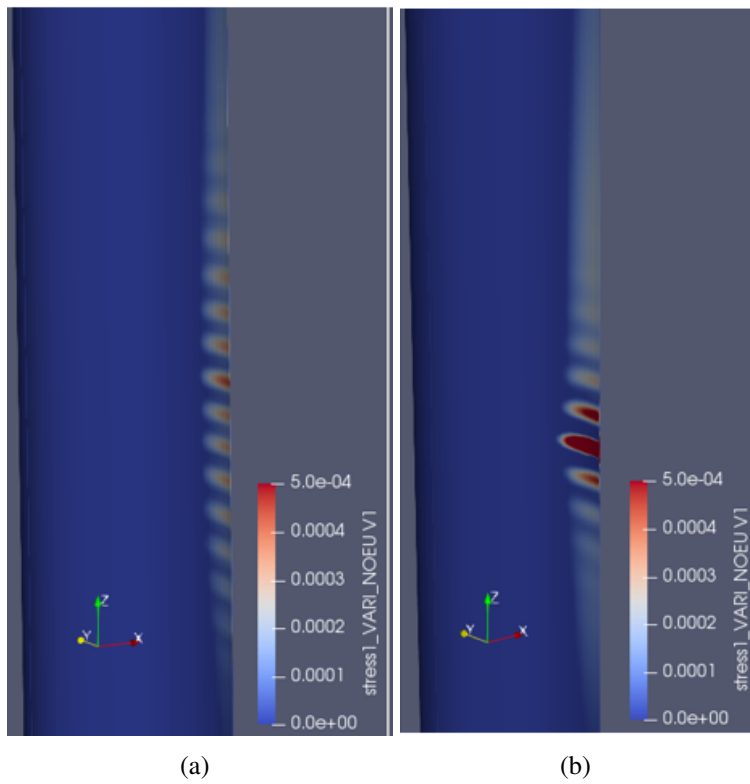


Figure 2.6: Plastic strain field for a 3MN load without (a) and with a crack (b).

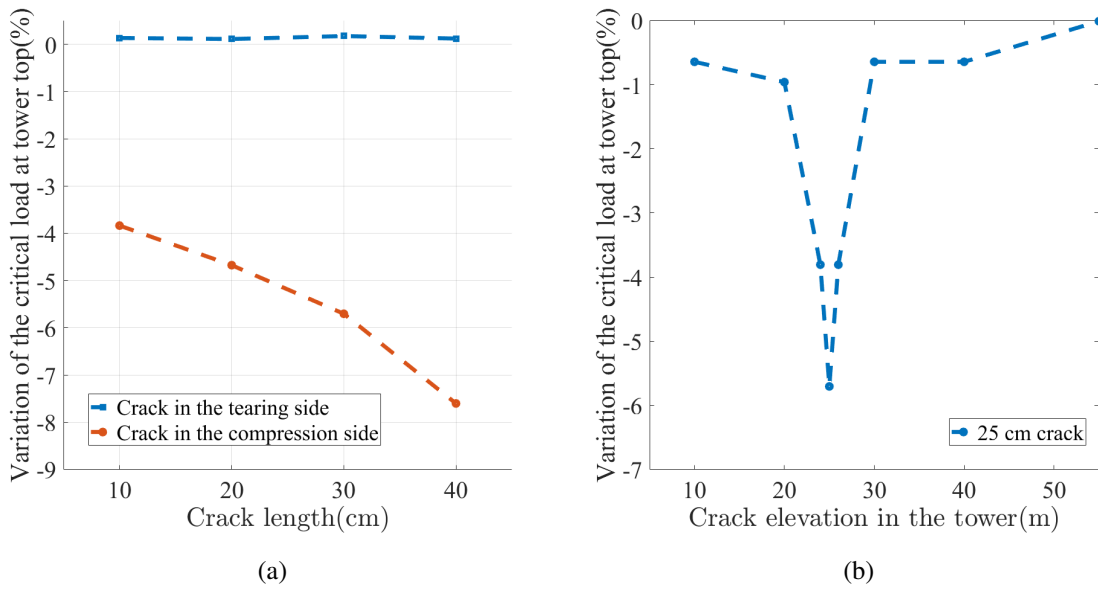


Figure 2.7: Influence of a crack placed in the tearing or in the compressive side on the critical buckling load for several crack lengths at a 25 m height (a) and for different elevations in the tower (b).

However, their influence should remain minor.

2.3 Wind turbine failure by crack propagation

The purpose of this section is to present the theoretical basis for fracture mechanics, and the results obtained on the limit loads for an academic NREL wind turbine.

2.3.1 Literature review

Few publications have addressed the presence of cracks in wind turbines. This type of finding is generally not disseminated in the public sphere by wind farm companies. It was identified that the hotspots areas were at the welds and that the cracks appeared at the material-weld junction (Section 1.3.5). Publications are mainly interested in establishing methods to assess the fatigue resistance of these structure areas or to explain premature fatigue encountered. For example a crack was identified in the lower part of a wind turbine [Lacalle et al., 2011]. A strategy to identify crack initiation cause has been set. Then, fatigue calculations were undertaken but the author remained at a material fatigue scale, no crack propagation study was performed. In Ref. [Cicero et al., 2009] a methodology was developed to study the criticality of a defect in cylindrical structures. This approach was inspired by the standards on fatigue of metallic materials. Defect growth was studied based on the Paris's law. In conclusion, the study of the behaviour of onshore wind turbines at extreme loads in the presence of cracks from the point of view of their critical propagation has not been studied in the literature to the author's knowledge.

2.3.2 Fracture mechanics

Introduction

Fracture is a heterogeneous process of deformation, causing the separation of different areas of a material, and, leading to the decrease to zero of the load capacity. Several types of fractures exist depending on the studied materials. Elastic-brittle fracture appears for materials whose overall behaviour is linear elastic and when the fracture occurs abruptly. Ceramics and glasses correspond to these characteristics. Quasi-brittle fracture occurs when the behaviour is non-linear approaching the maximum admissible stress, such as for composites or concrete. For steels, there are two types of fracture: plastic-brittle fracture and ductile fracture. In the first case, the material yields but breaks abruptly for relatively small strains. The second case corresponds to a large scale yielding and a progressive failure of the material. This mechanism occurs in particular for ductile steels. The studied material is a J0235 steel at room temperature. To simplify the further study, it is assumed hereafter that the case of plastic-brittle fracture is relevant.

Crack mechanical description

The three modes of fracture are presented in Figure 2.8. Hereafter, the case of a crack in opening mode I is used.

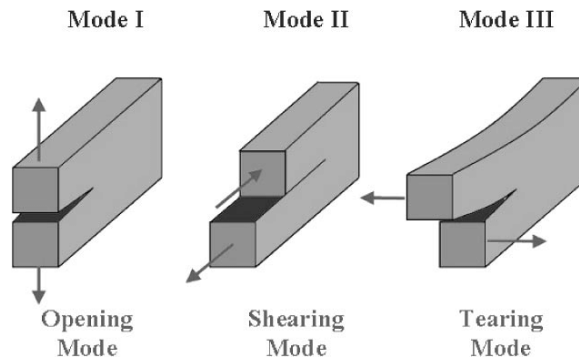


Figure 2.8: Different modes of fracture.

When a notch or open crack is present in a structure the stress distribution changes and becomes concentrated at singularities. The local stress is proportional to the stress that would normally be present without the defect, through a stress intensity factor K_I . This factor depends on the length of the crack and the geometry of the part under study. If an isotropic elastic material containing a crack is considered, the crack tip stress field σ_t expressed at a point P as a function of the distance to the crack tip, r , and the angle to the plane of the crack, θ , is expressed as follows [Irwin, 1957, Westergaard, 1933]

$$\sigma_t = \frac{K_I}{\sqrt{2\pi r}} f_a(\theta) \quad (2.1)$$

This solution is obtained by the Airy potential f_a method assuming plane stresses or strains in the case of a crack in opening mode I.

Energetic approach

The energetic approach to crack propagation was first introduced by Griffith [Griffith, 1921]. The energy release rate, G , related to a crack extension is defined as the infinitesimal variation of the potential energy ∂W in the structure due to an increment of crack surface ∂A under constant displacement, or load

$$G = -\frac{\partial W}{\partial A} \quad (2.2)$$

Within this theoretical framework and assuming that only mode I is to be considered, the following equivalence is obtained for plane strains

$$G = \frac{K_I^2}{E}(1 - \nu^2) \quad (2.3)$$

and in plane stresses

$$G = \frac{K_I^2}{E} \quad (2.4)$$

where E is the Young modulus, and ν the Poisson's ratio. Under plane elasticity condition the calculation of this quantity is similar to the evaluation of the J integral, or Rice integral [Rice, 1968], defined as

$$J = \int_{\Gamma} (w dy - \mathbf{t} \frac{\partial \mathbf{u}}{\partial \mathbf{x}} ds) \quad (2.5)$$

with Γ the closed contour surrounding the crack, w the strain energy density, \mathbf{t} the traction vector on the contour, \mathbf{u} the displacement vector, \mathbf{x} the coordinates and ds a contour element. Practically, in 2D, the contour considered for the calculation is generally a cylinder characterized by minimum and maximum radii. In practice, steels are known to yield before they break. To remain within the elastic frame the minimum radius must be far enough from the crack tip. It is possible to estimate the radius of the plastic area r_Y from the crack tip using Irwin's formula, approximating that the material is perfectly plastic

$$r_Y = \frac{1}{2\pi} \left(\frac{K_I}{\sigma_Y} \right)^2 \quad (2.6)$$

where σ_Y is the yield strength. The determination of this plastic zone size allows for the modeling choice for the calculation of G . First, if plasticity is confined, which means that the plastic radius is small with respect to the crack size, a classical elastic calculation can be carried out. The choice of the minimum radius limit for G computation with respect to the crack front is then made beyond the plastic zone. This approach is valid for elasto-plastic materials as long as the load remains monotonic and radial which is the case if critical crack propagation is considered. If the plastic radius is large with respect to the crack length or if the loads are non monotonic more complex methods must be used to properly consider elasto plasticity [Bui, 1978, Leblond, 2003]. Local [Beremin et al., 1983] or

energetic [Lorentz et al., 2000, Lorentz and Wadier, 2004] methods have been developed for instance.

Three-dimensional approach

Since the case study is a wind turbine, it is necessary to consider three-dimensional crack propagation, where the crack is likely to propagate along its plane. Let γ be the crack front, regular curve parametrized by its curvilinear abscissa ζ . $G(\zeta)$ represents the local energy release rate at point ζ of the front. For the case studied hereafter, the ratio between the thickness of the tower and its radius is of the order of 100, which can then be considered very thin. It is mentioned [Cicero et al., 2009] that given the geometries of wind turbine towers and the loading they are subjected to, a crack if it is to grow will quickly traverse the whole thickness. Under flexural loadings it is expected that G will be uniform along the crack front. Moreover, only the mode I is to be considered.

Crack propagation

Three regimes are distinguished with respect to crack propagation: non-propagation due to low stresses around the crack tip, stable propagation and unstable propagation. If only mode I is considered, these propagation regimes are directly related to the value of the corresponding stress intensity factor. Above a threshold, the crack begins to propagate. This is followed by a stable propagation regime, characterized by Paris's law [Paris, 1961, Paris and Erdogan, 1963]. Many experiments conducted on different materials have shown that crack growth rate, noted $\frac{da}{dN}$ is related to the variation of the stress intensity factor over the same cycle: $\Delta K = K_{max} - K_{min}$, where K_{max} denotes the maximum value, and K_{min} the minimum. This law is no longer valid above a certain stress level at the crack tip. The value of K_I is limited to a critical value K_{Ic} called "fracture toughness". This parameter characterizes the resistance to crack propagation of a material and is an inherent property in the same way as the yield stress. Both properties vary with temperature, loading rate and metallurgical structure. The three regimes are depicted in Figure 2.9.

From an energetic point of view, there is also a critical fracture energy, which is noted G_c , and the Griffith relationship is still valid with respect to fracture toughness. Under plane stress condition

$$G_c = \frac{K_{Ic}^2}{E} \quad (2.7)$$

When this limit value is reached, the propagation may remain stable or become unstable, depending on the structure geometry. In the case of a double cantilever beam test [Kanninen, 1974], the assembly is designed so that as the crack propagates the stress decreases at the crack tip and so K_I does. Considering a center cracked tension specimen [Gamot et al., 2019], as the crack grows, stresses increase for an equivalent loading. Thus when the maximum stress intensity factor value is reached the propagation becomes unstable or "critical". When a wind turbine tower is subjected to a bending load, a crack would propagate circumferentially if it is located on the tensile side. Then, the structure resistance would be carried by a smaller surface area, thus reaching the limit value would induce a critical crack propagation in this case. This assumption will be checked in Section 2.3.3. At room temperature $K_{Ic} = 80 MPa \cdot \sqrt{m}$ [EDF, 2018].

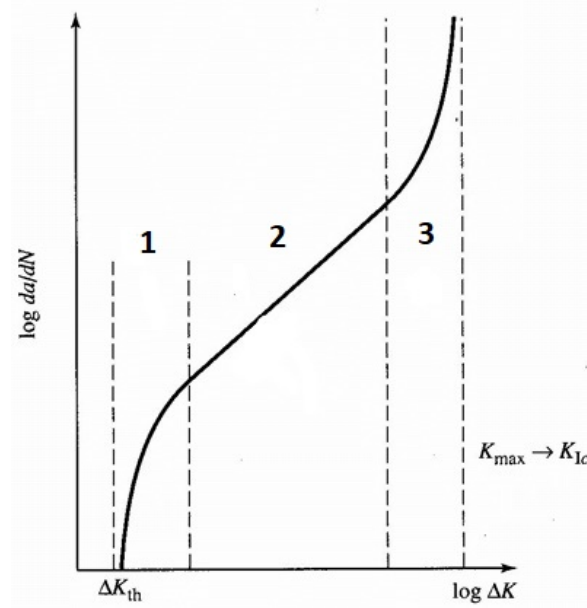


Figure 2.9: Three crack propagation regimes [Dillian et al., 2017]. 1: no propagation, 2: stable propagation, 3: unstable propagation

2.3.3 Application to NREL case

In this part the NREL turbine model is studied.

Modelling

The Zcracks mesh is still used but this time in a more refined way to integrate the crack within the tower mesh [Barsoum, 1974]. The calculation of the energy release rate requires a finer mesh at the crack tip, as shown in Figure 2.10. The number of FE nodes at the crack front is approximately 100.

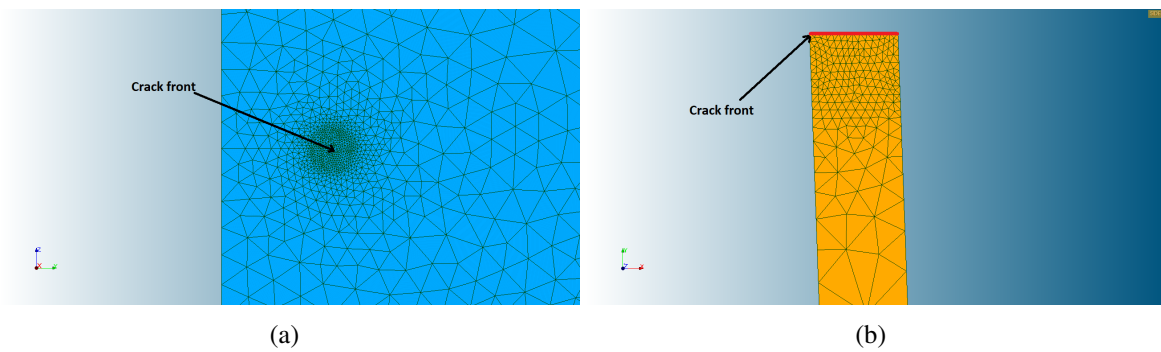


Figure 2.10: Mesh in the crack tip vicinity from side view (a) and upper view (b).

The calculated plastic radius is $r_Y = 8mm$. It shows that plasticity remains confined close to the crack tip, relatively to long cracks from 10 cm to 50 cm. Here the load is considered radial and proportional, thus an elastic calculation is sufficient. The crack is located at the place of highest stress, i.e. at 25m height. The calculation of G is carried out by means of the function $Calc_G$ [EDF, 2017b]. At the vicinity of the crack tip the Integration bounds are chosen based on the plastic radius. Thus

the lower integration bound is taken at 2 cm from the crack front. Two upper integration bounds are tested, 3 cm and 4 cm, and the local strain energy release rates are plotted along the crack front in Figure 2.11.

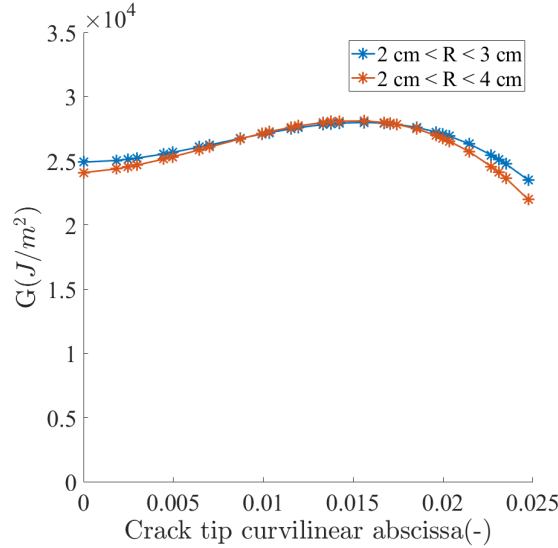


Figure 2.11: Strain energy release rate for a 10 cm crack for different upper integration bounds .

As expected, the value of G is quasi uniform along the crack front, thus averaging its value is possible. It can be noticed that the upper integration bound has virtually no influence on the result.

Critical loading

The critical load value at which the crack propagates in an unstable manner is obtained iteratively, as long as mean value of G is less than G_{Ic} . For cracks with lengths from 10 cm to 50 cm the associated critical load values are plotted in Figure 2.12.

The longer the crack length, the lower the failure load. Between two cracks of 10 and 50 cm, the calculated critical load is divided by a factor of more than 2. This observation shows that it is necessary to detect a crack in the structure as soon as possible before it becomes dangerous for its integrity.

2.4 Failure modes and simulation of a storm case

2.4.1 Worst failure mode with a crack

The previous two sections have identified strategies to quantify the impact of a crack-like defect on the critical load that a wind turbine can sustain with respect to buckling and crack propagation. The results found are summarized in Figure 2.13. The most critical mode is due to crack propagation, which causes the upper part of the tower to be torn off. Then, buckling may also occur due to the loss of lateral rigidity. Between two cracks of 10 and 40 cm, the critical load is halved with regard to the critical propagation. For buckling, a drop of 8% is calculated at the worst. The presence of a crack therefore has little influence on the critical load level for buckling. This result is very interesting

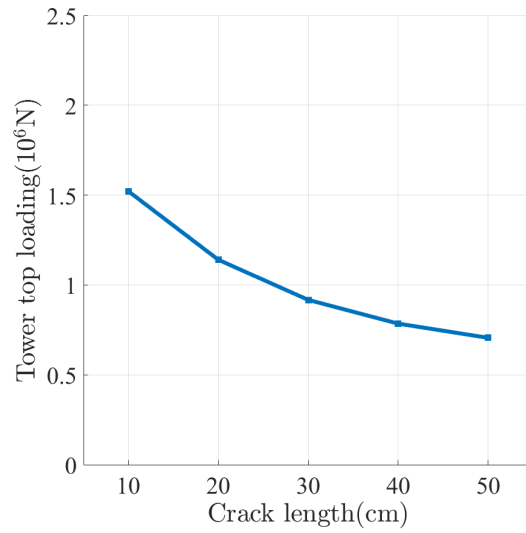


Figure 2.12: Critical tower loads corresponding to several crack lengths

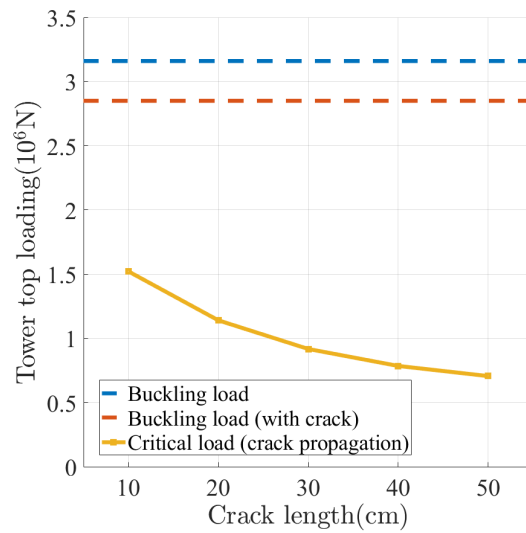


Figure 2.13: Critical loadings concerning buckling and critical crack propagation.

considering the residual life time assessment of turbine towers. At the design stage, only buckling is considered in case of extreme loads. This study shows that even if a tower is damaged, its buckling resistance is still robust. To reassess the service life duration, the critical crack propagation must be considered and wind farm operators must ensure that no cracks have initiated at the hotspot areas during the service life.

2.4.2 Simulation of critical load

As mentioned in Section 1.3.5, a wind turbine undergoes extreme loads in two main types of cases. In case of strong, swirling winds the rotor axis may not be aligned with the wind direction, so even in the flag position the turbine will be subjected to high loads. The second case also takes place during strong winds, coupled with a malfunction of the turbine control system. This can range from rotor overspeed or failure of the turbine yaw motor, so that as in the previous case the rotor will not be aligned with the wind direction. To prevent from such cases, the standards require that the turbines must still be able to withstand exceptional loads [IEC, 2005]. The case of rotor misalignment regarding the wind direction in the stop emergency position is one such case. The structures must be able to withstand:

- Winds relative to annual storms with a misalignment of 20 degrees.
- Winds relative to a 50-year storm with a misalignment of 8 degrees.

It is proposed here to illustrate such cases with simulations. In addition to structural characteristics the aerodynamics parameters of the blades are available [Jonkman et al., 2009]. Thus, the whole turbine can be modelled in Diego, an in-house aeroelastic code [Milano et al., 2019], and dynamic simulations can be carried out. A more complete description is proposed in Appendix A.

The wind is considered with no turbulence, i.e of constant magnitude. Here the wind turbine is put in "flag" position with an incident wind misaligned with respect to the rotor. Initially, wind velocity is 30 m/s, then after 100 seconds a gust is simulated by gradually increasing the wind over a period of five seconds, and then returning to the initial speed. The forces brought back to the hub are calculated for maximum wind speeds ranging from 40 m/s to 70 m/s and are plotted in Figure 2.14.

When the gust is initiated, the total force increases until it reaches a peak caused by aerodynamic and inertial effects. The maximum recorded tower top loads are summarized in Figure 2.15.

With a 40 cm crack, the critical load at the hub is of the order of 0.8 MN, which occurs for a misalignment of 20 degrees with winds speeds greater than 60 m/s. To give an order of magnitude, the strongest winds measured in 2018 in France had a velocity of 62 m/s on January 16 for storm Fionn in Corsica [Meteo-France, 2020]. Each year, during storms or thunderstorms the maximum wind speeds recorded often reach 45 m/s. The calculations presented here are specific to the NREL turbine model. However, they remain valid in magnitude orders for industrial turbine models.

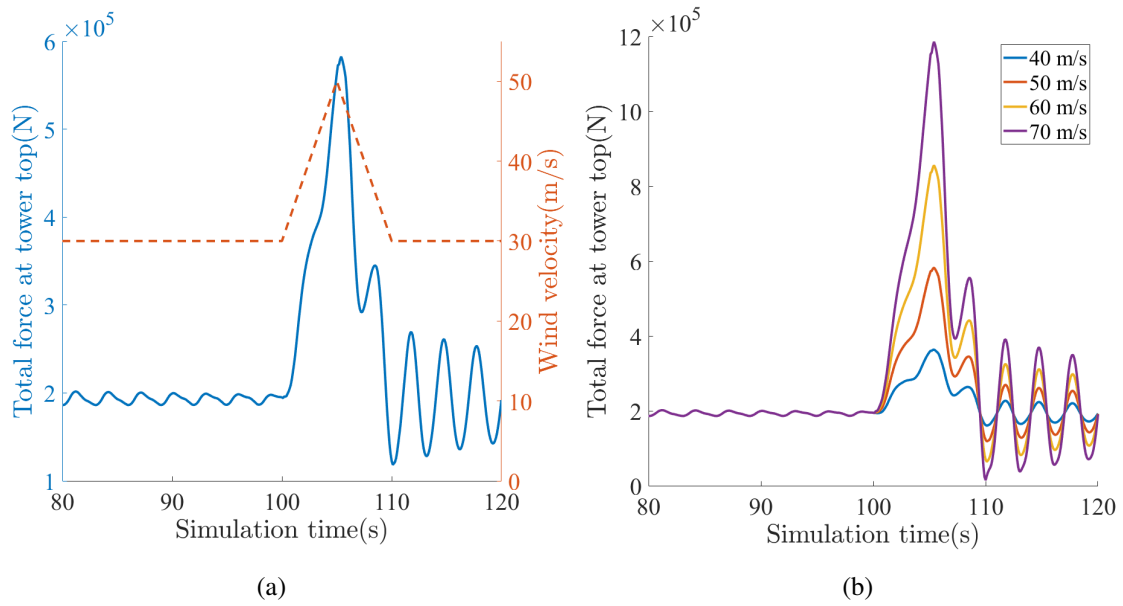


Figure 2.14: Aeroelastic loads simulated with Diego with a wind misalignment of 20 degrees for a wind velocity of 50 m/s (a) and for others (b).

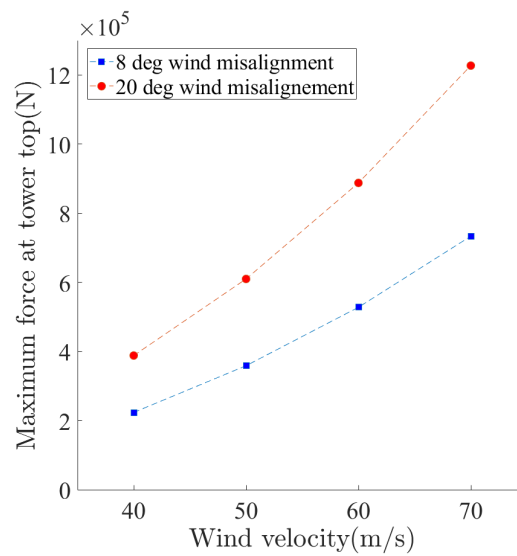


Figure 2.15: Maximums tower top loads due to rotor misalignment.

2.5 Conclusion and perspectives

The crack presence in a wind turbine tower can induce two different modes of failure: early buckling of the tower and the fatal crack propagation under extreme loading. First, concerning flexural buckling, it has been shown that it is more influenced if the crack is located on the compressive side than on the tensile side. However, for a thick shell such as a wind turbine tower, the influence is small: about 8% decrease on the buckling load for a 40 cm crack. For the studied tower model, the limit load relative to the critical propagation of a 10 cm crack is two times lower than the buckling limit load. For a 40 cm crack it is three times lower. The criteria for certification of the residual service life of a wind turbine structure must therefore be based on the resistance to crack propagation. Their detection before they reach a critical size is of paramount importance. Moreover, with the constant optimization of structures in a context of competitiveness, these structures will be increasingly sensitive to the presence of defects, which further motivates their early detection. A case of high winds coupled with a misalignment of the rotor was simulated, corresponding to standards worst scenario. With a 20 degrees RNA misalignment coupled with wind velocity of 60 m/s, the aeroelastic force was close to the critical load for a 30 cm long crack. As a perspective, in this work, fatigue crack propagation has not been addressed. It should also be taken into account for the calculation of the residual service life based on the actual wind conditions measured on site. It is known that cracks are present at the material-weld interface. In this work this aspect has been neglected. The objective was simply to compare the criticality of both collapse modes. However, an improvement would be to integrate initial stresses due to the welding process. Fatigue test campaigns carried out under site conditions could also be conducted to better understand the material behaviour in these hotspot areas.

Chapter 3

DIC principle

Summary

This chapter aims to introduce the principles of Digital Image Correlation (DIC) that will be used in the following chapters. The concepts of classical, spatio-temporal DIC and optimal digital color image correlation are explained. A published article about the latter subject is exposed.

3.1 Introduction

In the experimental mechanics field, the use of local informative sensors such as strain gages or extensometers were mandatory to extract information, since no other option was available in the past. In the second half of the twentieth century, technological advances in digital cameras have pushed the use of this technology for experimental mechanics. They are full-field sensors that enable information to be acquired from the whole experimental scene. First, the cross-correlation technique has been applied to digital images to measure shifts in datasets [Anuta, 1970, Keating et al., 1975]. The concept of Digital Image Correlation (DIC) as used nowadays has emerged in the 1980's [Peters et al., 1983, Sutton et al., 1983, Chu et al., 1985]. First, local approaches have been developed. They rely on dividing the Region Of Interest (ROI) in multiple subsets. The displacement of each subset is sought independently. Local finite element shape functions can be selected to locally consider strains of first order [Bruck et al., 1989] or second order [Lu and Cary, 2000]. The global approach has appeared later on. It consists in solving the DIC problem over the whole ROI at the same time [Wagne et al., 2002, Besnard et al., 2006]. A global formulation allows to any global property of the kinematic fields to be accounted for, by choosing them in an adapted space, or by penalizing their deviation from this property. One simple kinematic hypothesis is, for instance, the displacement continuity over the whole ROI [Besnard et al., 2006]. The ROI can be divided into finite elements and they constitute a mesh. Then, the displacement continuity is enforced at each mesh node. Several works have been devoted to evaluate which one, between local and global approaches, was the most suited for experimental mechanics. The local subset-based DIC is known to be a faster solving technique due to its simplicity [Pan et al., 2015, Pan et al., 2016]. However, complex displacement fields are less properly identified. The global DIC philosophy presents the main advantage to be physics-based. It enables to gain robustness with noisy images thanks to displacement continuity, and lower measurement uncertainty with appropriate shape functions [Hild and Roux, 2012a]. The displacement fields can be directly compared to finite element simulations, and calibration procedures can be then implemented [Grediac et al., 2006, Mathieu et al., 2015, Claire et al., 2004]. In this work, the FE-based approach will be used. The theory about monochrome DIC and color DIC will be presented. For the latter, it can be emphasized that the presented theory about digital color image correlation is novel (and has been published [Curt et al., 2020b]). The goal was to establish the optimal mathematical framework to perform optimal DIC with N channels. The instantaneous and spatio-temporal DIC methods to measure displacement fields will also be explained. These concepts will be used in the following chapters. *The sections that are part of the published article [Curt et al., 2020b] are delimited with a red rectangle*

3.2 Instantaneous DIC

3.2.1 Monochrome DIC

First, DIC with monochrome images is based on registering an image $f(\mathbf{x})$ defined as a “gray” level f for all pixels in a region of interest $\mathbf{x} = [x, y]$ in the reference configuration, and a series of pictures $g(\mathbf{x})$ of deformed configurations. The objective is to measure the displacement field \mathbf{u} that obeys the brightness conservation up to the presence of noise η

$$f(\mathbf{x}) = g(\mathbf{x} + \mathbf{u}(\mathbf{x})) + \eta(\mathbf{x}) \quad (3.1)$$

In other words, the two images are said to be registered when their difference, the so-called residual, $\rho(\mathbf{x}) = g(\mathbf{x} + \mathbf{u}(\mathbf{x})) - f(\mathbf{x})$, cannot be distinguished from noise.

It is quite usual to face a white Gaussian noise. Gaussian refers to the probability distribution function that is a centered Gaussian, and thus only characterized by its standard deviation $\sigma(\mathbf{x})$. “White” means that the noise affecting two distinct pixels is uncorrelated, so that the power spectrum of the pair correlation function is uniform over all wavevectors, akin to “white light,” which has a uniform power density over all wavelengths. It is worth noting that noise usually affects both reference and deformed images. However, when both noise fields are uncorrelated, they can be grouped as one equivalent field as above written, with a double variance as compared to each single-image noise field.

In the case of Gaussian noise, the probability of observing a residual $\rho(\mathbf{x})$ at point \mathbf{x} reads

$$P(\rho(\mathbf{x})) = \frac{1}{\sigma(\mathbf{x})\sqrt{2\pi}} \exp\left(-\frac{\rho(\mathbf{x})^2}{2\sigma(\mathbf{x})^2}\right) \quad (3.2)$$

If η is “white,” the probability of obtaining a residual field $\rho(\mathbf{x})$ over the ROI composed of N_x pixels is simply the product of the pixel-to-pixel probabilities

$$\begin{aligned} P(\rho) &= \prod_{k=1}^{N_x} P(\rho(\mathbf{x}_k)) \\ &= \prod_{k=1}^{N_x} \frac{1}{\sigma(\mathbf{x}_k)\sqrt{2\pi}} \exp\left(-\frac{\rho(\mathbf{x}_k)^2}{2\sigma(\mathbf{x}_k)^2}\right) \\ &= \left(\prod_{k=1}^{N_x} \frac{1}{\sigma(\mathbf{x}_k)\sqrt{2\pi}}\right) \exp\left(-\sum_{k=1}^{N_x} \frac{\rho(\mathbf{x}_k)^2}{2\sigma(\mathbf{x}_k)^2}\right) \end{aligned} \quad (3.3)$$

where the products or sums run over all pixel labels k , while \mathbf{x}_k refers to their location. Thus, the maximum likelihood of this residual is achieved by minimizing the opposite of the argument of the exponential, *i.e.*, the quadratic pixel-to-pixel difference between both pictures, weighted

by the inverse noise variance

$$\begin{aligned} Q &= \frac{1}{2} \sum_{k=1}^{N_x} \left(\frac{\rho(\mathbf{x}_k)}{\sigma(\mathbf{x}_k)} \right)^2 \\ &= \frac{1}{2} \sum_{k=1}^{N_x} \left(\frac{f(\mathbf{x}_k) - g(\mathbf{x}_k + \mathbf{u}(\mathbf{x}_k))}{\sigma(\mathbf{x}_k)} \right)^2 \end{aligned} \quad (3.4)$$

Moreover, if the standard deviation of the noise is uniform throughout the considered ROI, the maximum likelihood of image matching reduces to minimizing the quadratic pixel-to-pixel difference

$$Q[\mathbf{u}] = \frac{1}{2\sigma^2} \sum_{k=1}^{N_x} (f(\mathbf{x}_k) - g(\mathbf{x}_k + \mathbf{u}(\mathbf{x}_k)))^2 \quad (3.5)$$

This derivation proves that when white, Gaussian and uniform noise occurs, then the Euclidean norm of the difference between the reference and the corrected deformed image is *optimal* (i.e., the least sensitive to noise) to register two grayscale images. Any other measurement of the discrepancy between these images may be used successfully. However, the corresponding uncertainty of the result cannot be smaller than with the above objective functional Q .

3.2.2 Displacement measurement

The objective is to find the displacement field that minimizes the Q . It is convenient to discretize the displacement field into N_{dof} degrees of freedom via finite element shape functions $\mathbf{n}_i(\mathbf{x})$ with unknown nodal displacements a_i

$$\mathbf{u}(\mathbf{x}) = \sum_{i=1}^{N_{dof}} a_i \mathbf{n}_i(\mathbf{x}) \quad (3.6)$$

The nodal displacements are determined modified Gauss-Newton algorithm where incremental corrections to the displacement are obtained from the linear problem [Besnard et al., 2006, Hild and Roux, 2012b]

$$[\mathbf{M}]\{\delta\mathbf{a}\} = \{\mathbf{b}\} \quad (3.7)$$

with

$$M_{ij} = \sum_{k=1}^{N_x} (\mathbf{n}_i(\mathbf{x}_k) \cdot \nabla f(\mathbf{x}_k)) (\mathbf{n}_j(\mathbf{x}_k) \cdot \nabla f(\mathbf{x}_k)) \quad (3.8)$$

and

$$b_i = \sum_{k=1}^{N_x} (\mathbf{n}_i(\mathbf{x}_k) \cdot \nabla f(\mathbf{x}_k)) (f(\mathbf{x}_k) - \tilde{g}_{\{\mathbf{a}\}}(\mathbf{x}_k)) \quad (3.9)$$

where $[M]$ is the DIC (Hessian) matrix and $\{\mathbf{b}\}$ the right hand side. In the above equation, $\tilde{g}_{\{\mathbf{a}\}}$ is the deformed image g , corrected by the current determination of the nodal displacements field

$$\tilde{g}_{\{\mathbf{a}\}}(\mathbf{x}) = g(\mathbf{x} + \sum_{i=1}^{N_{dof}} \tilde{a}_i \mathbf{n}_i(\mathbf{x})) \quad (3.10)$$

3.2.3 Measurement uncertainty

Theoretically, it is assumed that the deformed image is the sum of the reference image and a random white noise η , of zero mean and variance σ_ρ^2 . Let us evaluate the impact of such noise on the determination of the unknowns of the DIC problem. First, the noise does not affect $[M]$, but only the right hand side. Its derived quantity is

$$\delta b_i = \sum_{k=1}^{N_x} \eta(\mathbf{x}_k) \cdot (\nabla f(\mathbf{x}_k) \cdot \mathbf{n}_i(\mathbf{x}_k)) \quad (3.11)$$

Thus on average $\langle \delta \mathbf{b} \rangle = 0$ and

$$\langle \delta b_i \delta b_j \rangle = \sigma_\rho^2 M_{ij} \quad (3.12)$$

By linearity the fluctuating part of a component of the DIC solution δa_i is

$$\delta a_i = M_{ik}^{-1} \delta b_k \quad (3.13)$$

The fluctuating part of the whole unknown vector $\langle \delta \mathbf{a} \rangle$ is equal to zero and its associated covariance reads

$$\langle \delta a_i \delta a_j \rangle = \sigma_\rho^2 M_{ik}^{-1} M_{jl}^{-1} M_{kl} = \sigma_\rho^2 M_{ij}^{-1} \quad (3.14)$$

Thus the covariance matrix representing the uncertainty related to the determination of nodal displacement is simply proportional to the noise variance and to the diagonal of the inverse Hessian. It must be emphasized that a factor 2 must be taken into account if the noise variance is determined with a noisy reference image.

The measurement quality is affected by three parameters. First the quality of the speckle pattern due to the dependence of $[M]$ on the reference image gradients. Then the digital camera quality plays a major role, it will have a direct impact on the measurement uncertainty due to the dependence to the noise variance. The third element which can have an influence on the measurement is the choice of the shape functions and the number of degrees of freedom. A finer mesh will give lower correlation residuals but a higher measurement uncertainty [Besnard et al., 2006, Hild and Roux, 2012b].

3.2.4 Gray level correction

In many cases the gray level conservation is violated due to small illumination variations of the experimental scene. An affine transformation of the gray level scale is generally considered [Chu et al., 1985, Pan, 2011, Hild and Roux, 2012b, Kammers and Daly, 2013, Peng et al., 2012, Tong, 2005, Sciuti et al., 2020]

$$c(\mathbf{x}) + (1 + d(\mathbf{x}))f(\mathbf{x}) = g(\mathbf{x} + \mathbf{u}(\mathbf{x})) + \eta(\mathbf{x}) \quad (3.15)$$

where c and d are spatially varying fields. Like the displacement field they are discretized over the whole ROI thanks to N_{lum} shape functions m_i

$$c(\mathbf{x}) = \sum_{i=1}^{N_{lum}} c_i m_i(\mathbf{x}) \quad (3.16)$$

$$d(\mathbf{x}) = \sum_{i=1}^{N_{lum}} d_i m_i(\mathbf{x}) \quad (3.17)$$

Their determination, as for the displacement, relies on linear problem solving. They can be calculated either in the same loop of the displacement, alternatively after if their contribution is small [Mendoza et al., 2019].

3.3 Spatio-temporal DIC

3.3.1 Introduction

When a set of multiple images is considered, the DIC framework becomes spatio-temporal. The displacement fields associated to the deformed images are now denoted with the index t , associated to time. The number of images in a set is denoted N_t . The residuals are noted

$$\rho(\mathbf{x}, t) = g(\mathbf{x} + \mathbf{u}(\mathbf{x}, t)) - f(\mathbf{x}) \quad (3.18)$$

As previously, the images are said to be registered when their difference cannot be distinguished from noise. The grey-level conservation now becomes

$$f(\mathbf{x}) = g(\mathbf{x} + \mathbf{u}(\mathbf{x}, t), t) + \eta(\mathbf{x}, t) \quad (3.19)$$

The displacement fields obtained with instantaneous DIC are written as

$$\mathbf{u}(\mathbf{x}, t) = \sum_{i=1}^{N_{dof}} a_i(t) \mathbf{n}_i(\mathbf{x}) \quad (3.20)$$

where $a_i(t)$ are the unknown amplitudes. When a spatio-temporal analysis is considered, in the same way that $\mathbf{u}(\mathbf{x})$ is not determined in a punctual manner but via a shape function that delocalizes the

information, it is also possible to delocalize in time via the choice of temporal shape functions. Thus the displacement fields are directly solved spatio-temporally. Such an analysis can be carried out with (classical approach) and without (Proper Generalized Decomposition approach) *a priori* knowledge about the temporal shape functions. Their respective principles are described in the following.

3.3.2 Classical spatio-temporal DIC

The classical technique consists in giving as problem entry the shape functions covering space and time. One can choose coupled or separated shape functions in space $\mathbf{n}_i(\mathbf{x})$ and time $w_j(t)$. The latter option is the one used here after [Besnard et al., 2011]. The displacement fields are then expressed

$$\mathbf{u}(\mathbf{x}, t) = \sum_{i=1}^{N_{sdof}} \sum_{j=1}^{N_{tdof}} a_{ij} \mathbf{n}_i(\mathbf{x}) w_j(t) \quad (3.21)$$

The choice of the shape functions will define the kinematic space. The basis must be rich enough to properly describe spatio-temporal displacement fields. The solving scheme is still a modified Gauss-Newton algorithm and the linear problem has the same form

$$[\mathbf{M}^{st}] \{ \delta \mathbf{a}^{st} \} = \{ \mathbf{b}^{st} \} \quad (3.22)$$

Thanks to the separated time and space variables the main spatio-temporal DIC matrix $[\mathbf{M}^{st}]$ has the following simplified expression

$$M_{ijkl}^{st} = M_{ik} W_{jl} \quad (3.23)$$

with $[\mathbf{W}]$ the temporal DIC matrix with size $N_{tdof} \times N_{tdof}$

$$W_{jl} = \sum_{t=1}^{N_t} w_j(t) w_l(t) \quad (3.24)$$

The instantaneous DIC matrix $[\mathbf{M}]$ can be directly reused with this formulation. The same simplification occurs with the spatio-temporal right hand side \mathbf{b}^{st}

$$b_{ij}^{st} = \sum_{t=1}^{N_t} b_i(t) w_j(t) \quad (3.25)$$

It results in a simple weighted sum of the instantaneous right hand side by the chosen time functions.

3.3.3 Spatio-temporal PGD-DIC

The use of model order reduction techniques like Principal Component Analysis (PCA) or Proper Orthogonalized Decomposition (POD) have been used in DIC or DVC to extract the main information from a set of displacement fields [Hao et al., 2017, Jailin, 2018, Wang, 2019]. As an extension to the POD technique, the Proper Generalized Decomposition (PGD) has been introduced [Chinesta et al.,

2010, Nouy, 2010, Ladevèze, 2012, Ladevèze, 2014]. It builds in an iterative strategy, called *greedy* approach, a numerical approximation of unknown fields in a separated form, for instance in space and time. This technique has been first brought in the context of DIC [Passieux and Périé, 2012] for 2D DIC and then for DVC [Gomes Perini et al., 2014]. The displacement field was separately represented along different spatial representations. An extension has been proposed for spatio-temporal analyses in stereo-DIC [Passieux et al., 2018]. A fixed point algorithm was used. The spatio-temporal displacement field was strongly regularized by a unique vibration temporal mode. In Ref. [Berny et al., 2018] a new PGD spatio-temporal framework has been proposed in which the spatio-temporal displacement field can be regularized over time. The complete algorithm description is available in Ref. [Berny et al., 2018]. Here the main steps are presented.

First, the residuals $\rho(\mathbf{x}, t)$ are computed. Then, the matrix $[\mathbf{R}]$ representing the temporal correlations of residuals is calculated.

$$\mathbf{R}(t, t') = \sum_{k=1}^{N_x} \rho(\mathbf{x}_k, t) \rho(\mathbf{x}_k, t') \quad (3.26)$$

The temporal modes that are used in this approach are the $[\mathbf{R}]$ eigenvectors, $\beta_n(t)$. At each iteration, the N_m largest eigenvectors $\beta_n(t)$ are selected from the $[\mathbf{R}]$ matrix. The associated eigenvalues indicate the level of importance for each mode. Then, the associated spatial modes are calculated by only keeping the contribution from the temporal modes in the residuals

$$\alpha_n(\mathbf{x}) = \sum_{t=1}^{N_t} \tilde{\rho}(\mathbf{x}, t) \beta_n(t) \quad (3.27)$$

The right hand side of the problem to solve is calculated by computing

$$b_i^{pgd} = \sum_{k=1}^{N_x} \alpha_n(\mathbf{x}) \mathbf{n}_i(\mathbf{x}) \cdot \nabla f(\mathbf{x}) \quad (3.28)$$

Then the solution of the problem for each temporal mode is calculated as follows

$$d_i^{pgd} = M_{ij}^{-1} b_i^{pgd} \quad (3.29)$$

For each temporal mode the displacement update $\delta \mathbf{u}(\mathbf{x}, t)$ becomes

$$\delta \mathbf{u}(\mathbf{x}, t) = \beta_n(t) \sum_{i=1}^{N_{dof}} d_i^{pgd} \mathbf{n}_i(\mathbf{x}) \quad (3.30)$$

With such a procedure there is no regularization. A soft one can be performed by filtering the high-frequency variations of the shape functions. It is carried out by weighting the $[\mathbf{R}]$ matrix with a temporal regularization matrix $[\mathbf{T}]$ calculated as follows [Berny et al., 2018]

$$[\mathbf{T}] = ([\mathbf{I}] + \tau^2 [\mathbf{D}]^T [\mathbf{D}])^{-1} \quad (3.31)$$

with τ the regularization time, $[I]$ the identity matrix and $[D]$ the finite difference operator. The temporal modes are then calculated from the regularized matrix

$$[\tilde{R}] = [T] \cdot [R] \cdot [T] \quad (3.32)$$

3.3.4 Summary

Two different approaches have been presented to solve a spatio-temporal DIC problem. The classical one is very interesting because it enables the temporal shape functions to be chosen *a priori*, and narrowing the time space can be interesting in some cases, like for a modal analysis [Passieux et al., 2018]. The second method requires no *a priori* which is also very appealing. Moreover, the framework enables temporal regularization that can be carried out to only extract the main trends of the spatio-temporal displacement fields. For very low amplitude displacement fields or noisy images such a feature is highly appreciated.

3.4 Optimal Color Digital Image Correlation

3.4.1 Introduction

For scientific applications, monochrome cameras are used in most cases [Sutton et al., 2009]. At each pixel of the sensor, a brightness level is recorded. In standard laboratory conditions, a speckle pattern consisting of black and white paints is applied on the studied surface, which makes the use of monochrome cameras sufficient. Since the use of these cameras is mostly restricted to the scientific world, the diversity of the cameras available on the market is limited. Conversely, digital color cameras are widely distributed among the public with a large range of choices. High-quality and high-definition color cameras are today available at low cost compared to scientific cameras. It is therefore legitimate to question the best use of their performance. In the literature, digital color cameras have been used for various applications such as modal measurements [Jailin, 2018], 3D shape deformation detection [Yu and Pan, 2017b, Yu and Pan, 2017a], hybrid stereocorrelation using infrared and visible light cameras [Charbal et al., 2016b, Wang et al., 2019]. In these works the interest of using a color camera was not always addressed. The resulting color fields were transformed into a single grayscale field (generally without specifying the transformation used).

From this amount of (color) data, different options are available to perform DIC analyses. One easy choice consists in combining the color information into a single, or “gray,” equivalent level, and further use a classical DIC methodology [Jailin, 2018]. Generally, the color fields (*i.e.*, single gray level field transition) is not even mentioned in publications.

Alternatively, the three color fields (for RGB color encoding) can be exploited [Baldi, 2018]. It will depend on the data quality and diversity available from the image. For a gray scale image, the data stored on the three color filters are similar. Thus, performing DIC with

only one channel can be considered sufficient. Yet some information is lost, and hence this treatment cannot be “optimal.” For colored structures, working with all color components may benefit from all the stored data. However, particular attention must be paid to the noise features of each color.

Many standard color cameras are equipped with the so-called Color Filter Array (CFA) technology. It is assumed that the color fields are continuous and mostly smooth. Thus, the color components are not acquired at every pixel location; they are sampled on a regular array. At each pixel location, a single color component is stored, whereas other ones are calculated thanks to interpolation schemes from neighboring pixels. One of the most utilized architecture is known as the Bayer pattern [Bayer, 1976], which ensures to mimic the physiology of the human eye. There are twice as many green elements as red or blue are used to fit with human retina sensor features. Recent publications have addressed the question of usefulness of color cameras for DIC applications [Hang et al., 2016, Baldi, 2018, Petiot et al., 2015]. The influence of several parameters was studied in the literature regarding the use of commercial color cameras, namely, the utility of a color speckle, the demosaicing algorithm used and the transformation of color fields (from three fields into a single grayscale field).

More remotely related to color, let us mention the case of DIC performed on electron backscattered diffraction (EBSD) maps. In such a case, at each pixel, a crystal orientation information is available, or equivalently, three Euler angles, which can be loosely compared to the three primary colors. However, dealing with crystal orientations, the notion of “distance” between two crystal orientations has an objective meaning, that can easily be handled with a quaternion formalism, leading to an extension of DIC to register EBSD maps as proposed in Ref. [Shi et al., 2016]. Similarly, the “distance” between two RGB images at corresponding pixels has to be defined for digital color image correlation.

Since the beginning of imaging, the definition of color metrics has been the subject of intense research. For instance, the CIE 1931 color spaces [Smith and Guild, 1931, CIE, 1932] were the first quantitative links between distributions of wavelengths in the electromagnetic visible spectrum, and physiologically perceived colors in human vision. Nowadays, these metrics aim to more accurately represent the perceptions of color differences in the human eye in order to develop the most effective sensors and filters for digital color cameras [Indow, 1980, Melgosa et al., 1994, Ponomarenko et al., 2009]. For color- DIC, such considerations of human perception have no legitimacy. Instead, it is here proposed to use noise as dictating the most appropriate metric.

The objective of this work is to introduce the mathematical foundations of an optimal DIC method when color cameras are used. The quantification of acquisition noise, which is intrinsic to the camera, is carried out, thereby leading to a unique (*i.e.*, optimal) procedure to compare the distance between images, a question that lies at the root of any DIC formulation. When

spatial correlations are present, it will be shown that an appropriate linear transformation at a pre-processing stage can be used to unravel those correlations and restore a uniform white noise for which the comparison metric is trivial. A case study of displacement uncertainty quantification is performed when comparing different color image transformations.

3.4.2 Color image registration

This part aims to present the mathematical framework of optimal color DIC. In the following, a *global*-DIC framework will be used, where the entire Region of Interest, ROI, is considered at once with a finite element discretization of the displacement field. However, this choice has no consequence on the handling of colors as discussed hereafter. For *local*-DIC, it suffices to consider that what is mentioned for the entire ROI holds for smaller interrogation windows (*e.g.*, “subsets”).

A color image is usually composed of three fields for each of the primary hues. The most common technology is the Bayer filter consisting of four primary sensors organized as 2×2 subpixels. Each pixel contains two green, one red and one blue sensors [Bayer, 1976]. Figure 3.1 shows one possible sensor ordering, referred by the initial of the color of the matrix (top-bottom, left-right). These pixels repeat themselves horizontally and vertically.



Figure 3.1: Bayer pattern that can be used in color cameras

The reconstruction of the color fields on all elementary detectors from the Bayer matrix with the use of *demosaicing* algorithms consists in the interpolation of fields. Generally, the set of three color components is Red, Green and Blue (RGB). The stored data must be post-processed and interpolated [Longere et al., 2002, Chung and Chan, 2006, Hirakawa and Parks, 2005] to obtain three complete color channel planes. All algorithms aim at enhancing contrasts and restoring human vision. Some works have been devoted to understanding which demosaicing interpolation scheme is better suited for DIC purposes [Forsey and Gungor, 2016, Baldi, 2018]. The main conclusion is that low order interpolation schemes perform better. The algorithm that provides better results in terms of error and uncertainty was the one with no interpolation where the subpixels are *binned*. Only pixels corresponding to a Bayer elementary matrix were

considered as a unique gray level pixel [Baldi, 2018]. The bias induced by demosaicing results in noise with spatial correlations [Yu and Pan, 2017b], which is not appropriate for DIC applications [Baldi, 2018].

As seen for the previous monochrome case, DIC starts from a distance between two images, namely 1) the reference image and 2) the corrected deformed one, and among many possible distances, the one that is optimal exploits the known statistical information on noise within a Bayesian framework. Thus, it is crucial to characterize noise of color pictures in order to assess whether it may (or not) account for a given image difference.

When no spatial correlations are present, and for a Gaussian noise, the entire statistical characterization is contained in the covariance matrix \mathbf{C} defined as

$$C_{ij} = \langle \eta_i(\mathbf{x}) \eta_j(\mathbf{x}) \rangle \quad (3.33)$$

where $\eta_i(\mathbf{x})$ is the noise affecting the i -th color channel at pixel \mathbf{x} , and $\langle \bullet \rangle$ denotes the statistical expectation. It is assumed that $\langle \eta_i \rangle = 0$, otherwise a bias would be present, and in this case, because it would affect all images in the same way, it would not contribute to image differences and hence would be harmless.

Based on the color covariance matrix, the probability density for a noise vector $\boldsymbol{\eta}$ reads

$$P(\boldsymbol{\eta}) = \frac{1}{\det(\mathbf{C})(2\pi)^{3/2}} \exp\left(-\frac{1}{2}\boldsymbol{\eta}\mathbf{C}^{-1}\boldsymbol{\eta}\right) \quad (3.34)$$

Following the same footsteps as in the previous section, it is straightforward to express the probability that a color residual $\rho_i = f_i(\mathbf{x}) - g_i(\mathbf{x} + \mathbf{u}(\mathbf{x}))$ be solely due to noise. Maximizing this probability over trial displacement fields provides the *optimal* variational formulation of color DIC. More precisely, the co-logarithm of the likelihood is to be minimized, or

$$Q_N[\mathbf{u}] = \frac{1}{2} \sum_{k=1}^{N_x} \sum_{i=1}^3 \sum_{j=1}^3 \rho_i(\mathbf{x}_k) C_{ij}^{-1}(\mathbf{x}_k) \rho_j(\mathbf{x}_k) \quad (3.35)$$

where 3 is number of channels, and can be straightforwardly generalized to N if more channels are used (say for hyperspectral imaging). It can be observed that in the case of a noise that would uniformly affect all three color channels without correlation and with identical variance, then the above functional reduces to the canonical form

$$Q_3[\mathbf{u}] \propto \sum_{k=1}^{N_x} \sum_{i=1}^3 (f_i(\mathbf{x}_k) - g_i(\mathbf{x}_k + \mathbf{u}(\mathbf{x}_k)))^2 \quad (3.36)$$

3.4.3 Noise characterization

In this section, a method for characterizing the intrinsic noise of color cameras is introduced. Three properties are studied, namely, uniformity, spatial correlations and color space correlations. A set of color images with color speckle pattern is considered (Figure 3.2).



Figure 3.2: Color speckle pattern used herein

The experiment was very simple. A speckled sheet of paper, placed on a horizontal table, was repeatedly photographed with a camera mounted on a tripod. The hardware parameters of the optical setup are reported in Table 3.1.

Table 3.1: DIC hardware parameters

Camera	CANON E70D
Definition	2748 × 1835 (Bayer) pixels
Color filter	Bayer
Gray Levels amplitude	14 bits (raw data)
Lens	CANON 50-mm
Aperture	$f/12$
Field of view	274 × 182 mm ²
Image scale	100 μm/pixel
Stand-off distance	30 cm
Image acquisition rate	1-2 fps
Patterning technique	sprayed paints (see more details in text and Figures 3.2 and 3.10)
Pattern feature size (B/W)	3.4 pixels
Pattern feature size (colored)	3.8 pixels

The noise of color channel i in image number n , $\eta_i^n(\mathbf{x})$, is obtained from the following steps:

1. After converting all color images to a (monochrome) gray scale thanks to an rgb2gray transform [Kumar and Verma, 2010, Higham and Higham, 2017], the n th image was registered with the first one accounting for a rigid translation, \mathbf{u}^n . This registration was performed in Fourier space using cross-correlations [Hild and Roux, 2012b].
2. From the measured displacements, corrected images were computed $\tilde{g}_i^n(\mathbf{x}) = g_i^n(\mathbf{x} + \mathbf{u}^n)$. The chosen subpixel interpolation scheme was cubic (Table 3.2).
3. An average color reference image, $\hat{f}(\mathbf{x})$ was obtained by averaging over all corrected (*i.e.*, registered) color images, $\hat{f}_i(\mathbf{x}) = \langle \tilde{g}_i^n(\mathbf{x}) \rangle_n$ the three color fields with all corrected images \tilde{g}^n .
4. Last, the noise was computed as $\eta_i^n(\mathbf{x}) = \tilde{g}_i^n(\mathbf{x}) - \hat{f}_i^n(\mathbf{x})$.

The first two steps were needed because it was observed that spurious rigid body translations of small amplitudes occurred in the acquisition of image series. This may have been caused by ambient vibrations and a compliant setup, but due to the low frequency of acquisition, the translations appeared random in time. If such motions were not corrected, the apparent noise appeared to have a broader scatter, and a higher spatial correlation at short distances.

Table 3.2: DIC analysis parameters for rigid body translations

DIC software	Correli 3.0 [Leclerc et al., 2015]
Image filtering	None
ZOI size	1000 × 1000 pixels
Step size	None
Shape function	Constant
Matching criterion	Cross-correlation product
Interpolant	cubic
Displacement noise-floor (x direction)	1.6×10^{-2} pixel
Displacement noise-floor (y direction)	2.4×10^{-2} pixel

Spatial correlations

Let us recall that the 3-layer description of a color image given at the same pixel location is already a reconstruction, and even if no demosaicing algorithm is used, an interpolation scheme is inherently present at the scale of elementary color sensors, beneath the Bayer matrix scale. It is therefore very important to assess the presence or not of spatial correlations in noise. For a single field of data, the spatial autocorrelation function reads

$$C(\boldsymbol{\delta}) = \langle \eta(\mathbf{x})\eta(\mathbf{x} + \boldsymbol{\delta}) \rangle_{\mathbf{x}} \quad (3.37)$$

where the expectation value denoted by angular brackets can be substituted by a spatial average over x for stationary fields. The dimensionless autocorrelation functions of noise on the field associated with the red color are plotted for two images of the sample. In order to quantify acquisition noise, the images are shifted by translation movements using bi-cubic interpolation in both directions with respect to the first image, corresponding to the FFT-DIC calculation result. The applied rigid body displacements, that have been calculated for two real images, are:

- 0.018 pixel along x , 0.036 pixel along y for the first image.
- 0.056 pixel along x , 0.190 pixel along y for the second image.

The autocorrelation functions are plotted in two dimensions in Figure 3.3, and in each direction in Figure 3.4. The larger the translation amplitudes, the more correlated would nearest neighbor pixels be, as a result of the subpixel interpolation scheme. In particular, for half a pixel translation, the interpolated color level weights equally both neighbors (along each dimension). However, for small amplitude translations, the noise keeps its white character.

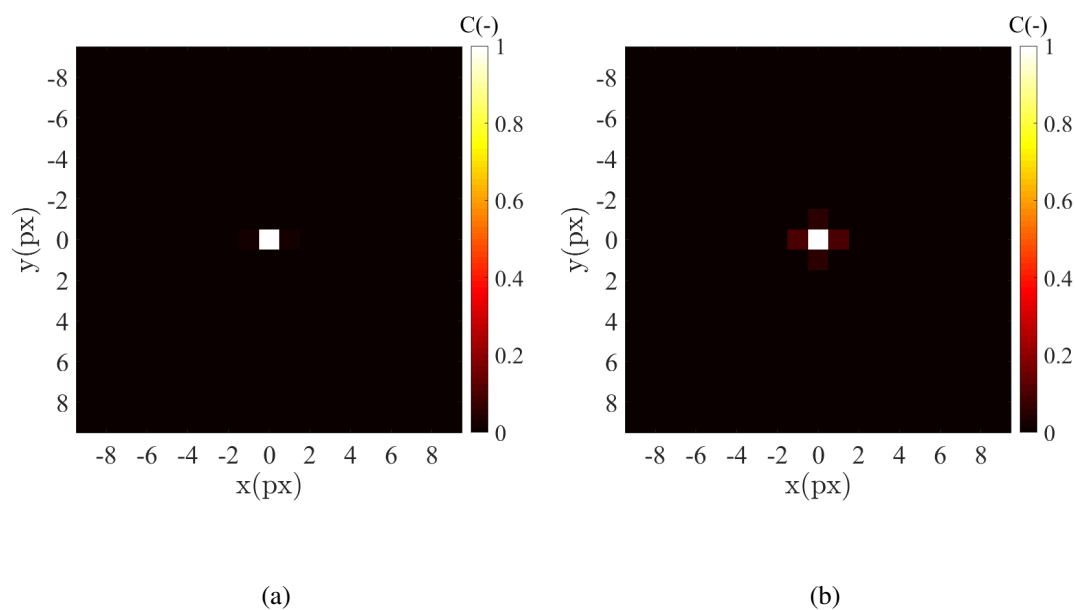


Figure 3.3: Autocorrelation functions for the red field for the first (a) and second (b) images

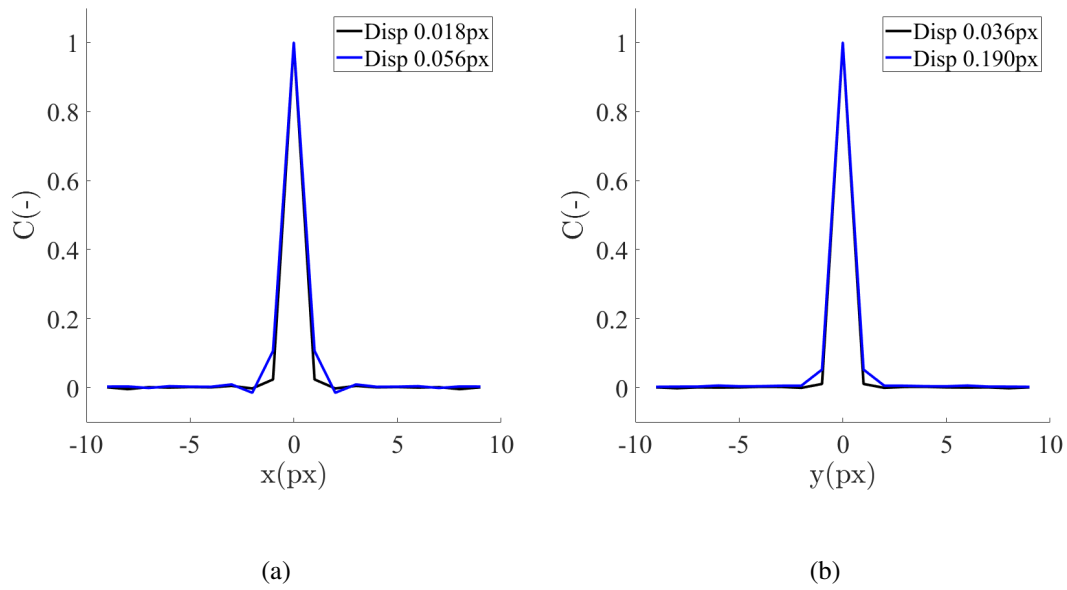


Figure 3.4: Autocorrelation functions along x (a) and y (b) directions

Noise uniformity

To determine the noise amplitude for different brightness levels, pixels are partitioned into 12 classes according to $\hat{f}_i(\mathbf{x})$, the intensity of each color channel of the reference averaged image. The entire encountered brightness range is considered. For each class, the noise variance of $\eta_i^n(\mathbf{x})$ over all pixels \mathbf{x} in the class is calculated for each image n . The latter is plotted as a function of the mean color brightness of the class (for the red channel as an example in Figure 3.5). Figure 3.5(b) shows that a much broader data scatter is observed if the slight motion that occurred during image acquisitions is not accounted for.

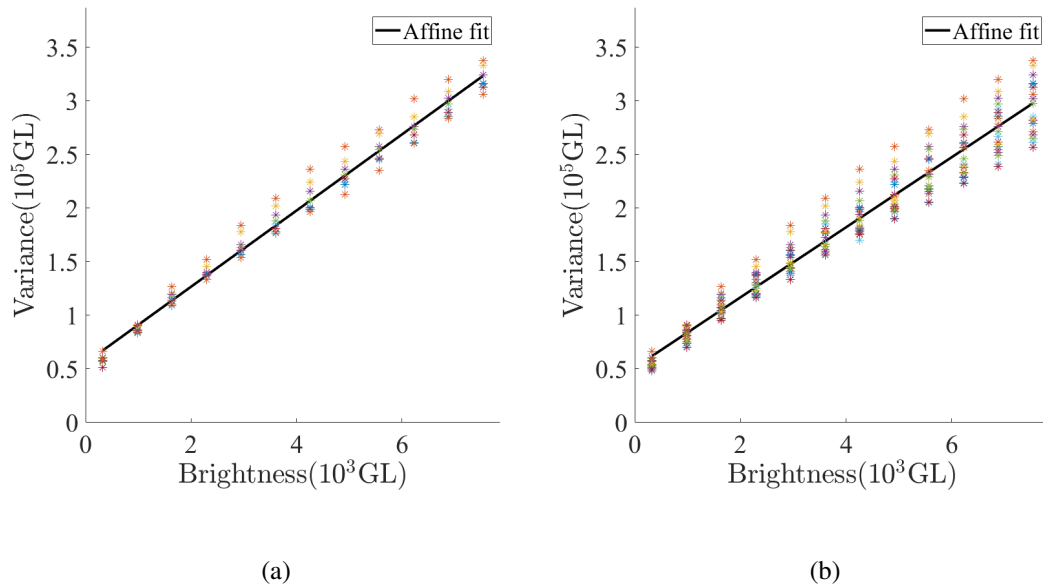


Figure 3.5: Variance of red brightness with (a) and without (b) corrections for rigid body motions. Units are in color levels (GL), encoded over 16 bits. The different symbols corresponds to the different images.

In Figure 3.5, an affine regression is also reported, which accounts quite precisely for the data points. This feature is characteristic of Poisson noise, which is a basic form of noise associated with the counting of independent events [Buades et al., 2009]. Let us note that an offset is introduced here to account for dark field noise. The observed linearity holds also for the other color channels as shown in Figure 3.6. Let us also underline that the color brightness is always high enough so that the Poisson distribution for the noise distribution matches very accurately a Gaussian distribution.

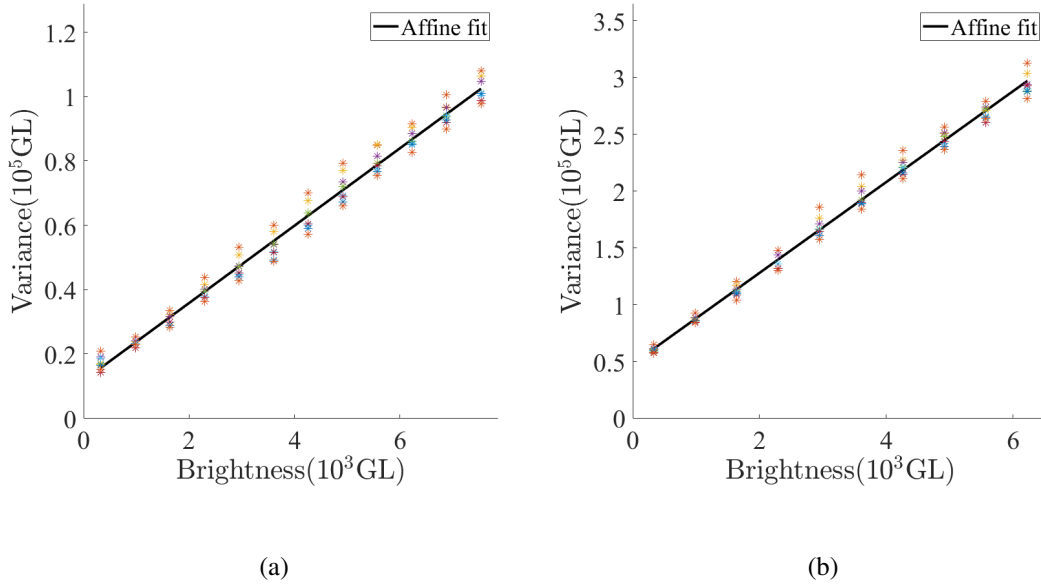


Figure 3.6: Variance for the green (a) and blue (b) color fields as functions of the brightness level

To handle images with Poisson noise, which would require a nonuniform weighting for an optimal DIC treatment, it is also possible to have recourse to the Anscombe transform [Anscombe, 1948, Sur and Grediac, 2014], which is a simple nonlinear transform on the brightness that renders the noise variance uniform

$$f_i \longrightarrow \sqrt{f_i - f_{i0}} \quad (3.38)$$

where f_{i0} corresponds to the offset of the affine regressions shown in Figures 3.5 and 3.6. Thus, after a pre-processing step consisting of the Anscombe transform that re-encodes the brightness, there is no need to weight the residuals non-uniformly, and a plain quadratic difference becomes optimal. Such Anscombe transform is applied to each color channel in the image set. To validate this treatment, a similar characterization of the noise variance after the Anscombe transform is performed. Figure 3.7 shows that indeed most of the systematic variation of the variance with the brightness has been erased or remains within the scatter of data points.

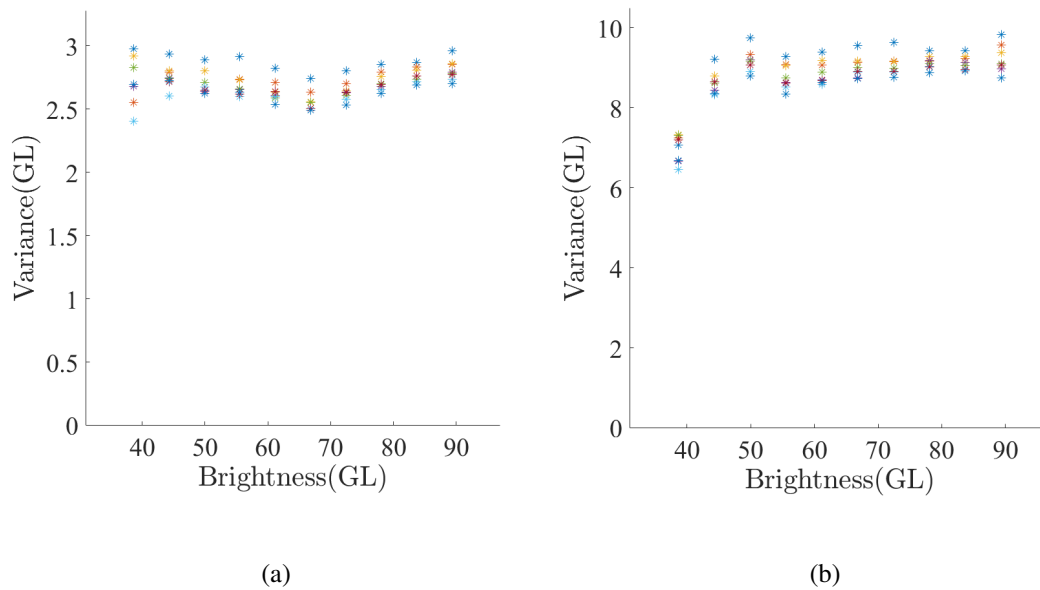


Figure 3.7: Variances for the green (a) and blue (b) color fields after Anscombe transform

Color space correlations

It has been shown, through transformations, that the noise variance can be made uniform with respect to brightness for the three color channels. In addition, if the raw data are used, noise has been shown to be spatially uncorrelated. However, correlations between different color channels after Anscombe transform have not yet been studied. The covariance matrix C (see Equation (3.33)) is now computed over the entire ROI. This symmetric matrix can be diagonalized, a procedure that allows eigenvectors, *i.e.*, “eigencolors,” to be defined as linear combinations of say R, G and B primary colors, which turn out to be uncorrelated. These eigenvectors are shown in Figure 3.8.

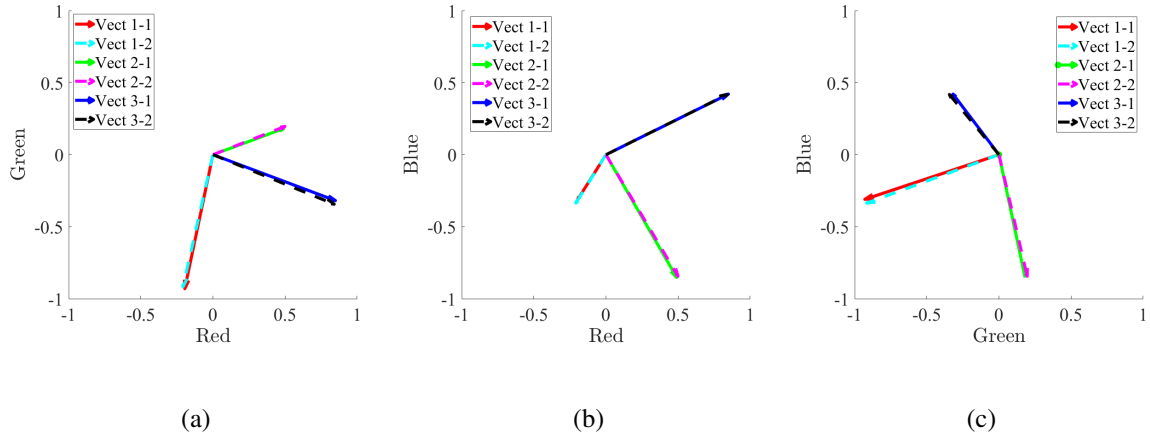


Figure 3.8: Plot of noise covariance matrix eigenvectors in planes (a) Red-Green, (b) Red-Blue and (c) Green-Blue. The eigenvector denoted as “Vect $i - j$ ” corresponds to the i th eigenvector of the j th image

The noise eigenvectors are not oriented along the primary color “directions,” thereby revealing that correlations between those primary colors exist. It is noteworthy that the linear transform $\hat{f}_i(\mathbf{x}) = \mathbf{C}_{ij}^{-1/2} f_j(\mathbf{x})$ allows a novel re-encoded image $\hat{f}_i(\mathbf{x})$ to be obtained for which the noise affecting the different color channels i is *independent*, and the noise variance is uniform and equal to 1. To illustrate this last property, Figure 3.9 shows the three “eigencolors” re-encoding the image displayed in Figure 3.2.

The procedure that consists in applying the above linear transform, left multiplication of the inverse square root of the covariance matrix, allows the noise affecting the re-encoded quantities to become *perfectly white*. This is very general and can be tailored to a large variety of problems. As a consequence, it renders trivial the handling of a Mahalanobis distance [Mahalanobis, 1936], which reduces to a mere Euclidean distance on the re-encoded quantities. The Mahalanobis distance is constructed with the inverse covariance as the metric tensor as in Equation (3.35). It is the optimal metric in the sense of leading to minimal uncertainties.

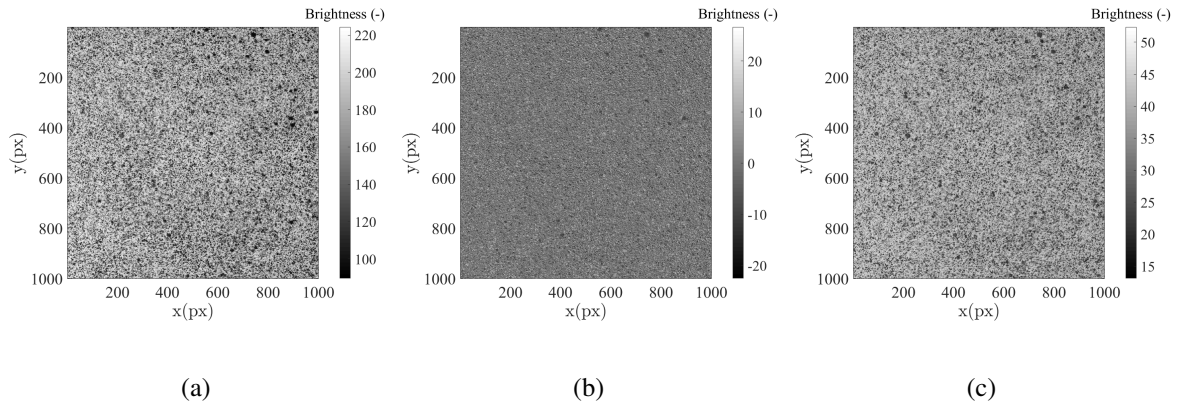


Figure 3.9: Projections of Figure 3.2 onto (a) first, (b) second, and (c) third color modes.

It is remarkable that the ranges of intensity of the *new* colors are markedly different due to the fact that noise has now a normalized variance. This method allows the Signal to Noise Ratio (SNR) to be assessed very quickly on each field. The noise intensity is now constant over all the fields. The SNR is only the logarithm of the L2-norm of each \hat{f}_i field. In the present case, the amplitude ranges from 35 to 120 between the three fields. It is noteworthy that this linear transformation can be applied at the pre-processing stage, after the Anscombe transform. Thus, after this simple color re-encoding (first nonlinear, then linear) the optimal color DIC procedure reduces to the canonical form Q_3 (see Equation (3.36)), which is mathematically equivalent to Q_N (Equation (3.35)), using only the Anscombe transformed image, and the full color covariance matrix.

3.4.4 Uncertainty quantifications

A way of assessing the noise level and measurement uncertainty is to acquire a set of images of a static sample where the reference image is the first one. This procedure was carried out for two different speckles, namely, one with black and white paints (Figure 3.10), and another obtained with red-green-blue paints (Figure 3.2). Let us stress the fact that these two speckles may have slightly different feature sizes (Table 3.1). However, the important point is not to directly compare them or their results, but rather that the trends obtained with different color processings are similar for both speckles.



Figure 3.10: Black and white speckle pattern used herein

The same optical setup as previously described was used (Table 3.1). To evaluate the performance of the DIC algorithm, eight different settings are tested:

- *Monochrome*: correlation with monochrome images issued from direct R-G-B fields summation.
- *Monochrome (rgb2gray)*: correlation with monochrome images issued from R-G-B fields summation with 0.2989, 0.5870, 0.1140 weights. This transform is usually selected to switch from color to grayscale pictures [Kumar and Verma, 2010, Higham and Higham, 2017].
- *Color*: correlation with color images considering the three color channels independent.
- *Poisson color*: correlation of images on three fields obtained with the Anscombe transform and normalized by their own noise variances.
- *Poisson monochrome*: monochrome images obtained by R-G-B field summation of Anscombe transform and normalization by noise variances in each color channel.
- *Eigencolor modes*: correlation with images projected onto noise eigencolor modes.
- *Eigencolor to monochrome*: monochrome image correlation obtained after summation of the three eigencolor mode fields.

The images were processed using the Correli 3.0 software (Table 3.3). It corresponds to global DIC with meshes made of 3-noded (T3) elements. When color images are considered, all color layers have the same kinematics. Therefore, all DIC Hessians (*i.e.*, one per color channel) and all gradients of the DIC cost functions are considered as an overdetermined system

to compute the common displacement field, and the latter is used to similarly correct all color layers of the deformed image.

Table 3.3: DIC analysis parameters

DIC software	Correli 3.0 [Leclerc et al., 2015]
Image filtering	see text
Element length	40 pixels
Shape functions	linear (T3)
Mesh	regular
Matching criterion	see text
Interpolant	cubic
Displacement noise-floor	see Figures 3.11 and 3.12

For each registration, the standard uncertainty is determined. It corresponds to the standard deviation of all nodal displacements in both directions. The results are shown in Figure 3.11 (resp. 3.12) for the black and white (resp. color) speckle pattern. Ten images were selected to show that the reported trends hold for the whole image series.

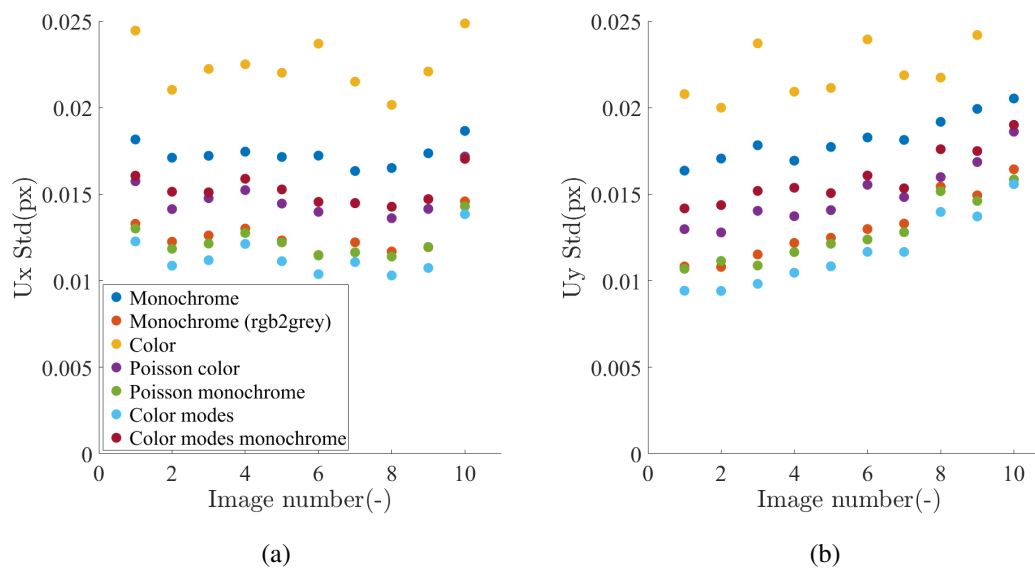


Figure 3.11: Standard displacement uncertainties with a black and white speckle pattern along x (a) and y (b) directions

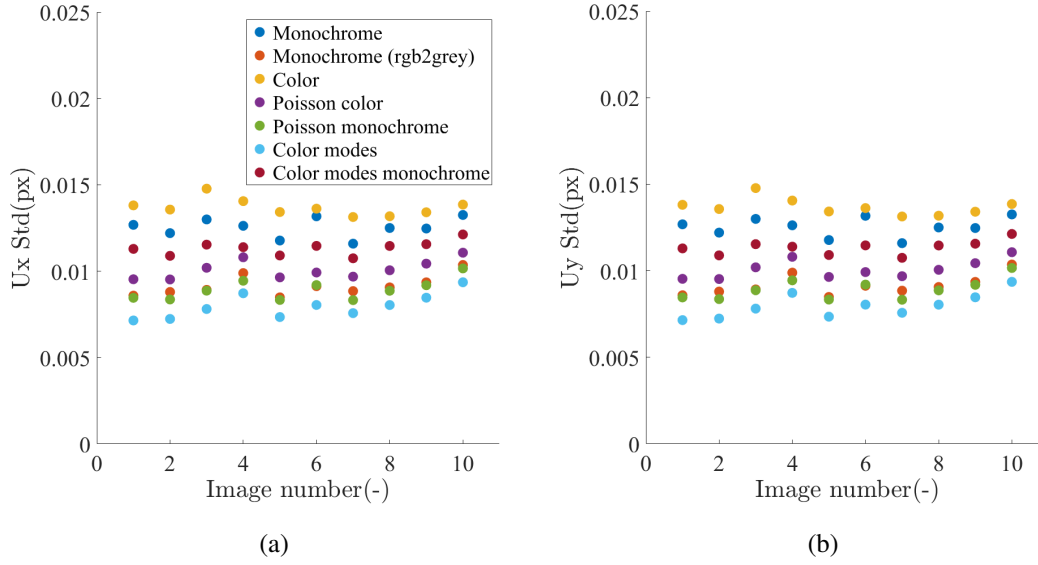


Figure 3.12: Standard displacement uncertainties with a color speckle pattern along x (a) and y (b) directions

The general trends are identical for both speckles. First, the highest uncertainties are observed with raw color images (*i.e.*, when the three fields are considered separately with no transform). The measurement uncertainties with monochrome images are lower than when color fields are considered separately with or without performing Anscombe transform and normalization. This observation is not valid when the transform on color modes is considered. The uncertainties are the lowest among all investigated cases. These results show that many different ways of handling color images may be considered, providing all a satisfactory answer, and only their uncertainties allow their respective merit to be ranked. In the above considered examples, the level of uncertainty varies very significantly (by about a factor of two). Among all possible variants, the optimal one (*i.e.*, theoretically defined as leading to the least uncertainty) indeed displays the lowest values.

Last, the uncertainty levels are lower with the colored speckles. These differences may have two causes. First, the combination of speckle and color sensors provides more information and therefore reduces the uncertainties. Second, the density of the colored speckles is higher than that of the black and white speckles (Table 3.1). No more investigation about this subject was conducted.

3.4.5 Conclusion and outlook

In this work, a consistent treatment of noise affecting color images within a Bayesian framework has led to the definition of an optimally-suited metric to evaluate image differences, thereby defining the *optimal* color DIC procedure. Moreover, the above study has shown that

the combination of two simple transformations, first an Anscombe transform, followed by a linear color combination along “eigencolors,” provided re-encoded images with which the optimal DIC procedure reduces to the canonical form, thereby allowing closed (*e.g.*, commercial) DIC softwares to be used, provided the different layers can be handled. Quantifications of standard displacement uncertainties were carried out using black and white, as well as color speckles. The conclusions were similar in both cases, namely, the color image transformation for DIC applications had a significant influence on the uncertainty levels (*i.e.*, they can vary by a factor of two). The transformation that allows one to benefit from the lowest uncertainties consists in re-encoding each color intensity using the Anscombe transform, and then further perform a rotation in the color space to align with (appropriately scaled) eigencolors.

The noise characterization was performed on three-color images, which are determined from three filters of different wavelengths. This type of analysis can be extended to hyperspectral image processing, which is much more computationnaly involved, by requiring the noise variance to be uniform and unitary over all processed wavelengths. It enables the whole data set to be reformatted in a canonical form for optimal handling.

Chapter 4

Damage detection at the mesoscale

Summary

In this chapter, the method envisioned to detect damage at the mesoscopic scale is presented. First, the details about the algorithm are shown and its performance is illustrated through an experimental case. Then, the industrial system is briefly introduced.

4.1 Structural Health Monitoring with DIC

This section is directly related to a preprint submitted for publication.

4.1.1 Introduction

Over the course of its life, a structure is often subjected to repetitive loading that may lead to the occurrence of damage [Rolfe and Barsom, 1977]. The latter can take the form of local yielding areas, open cracking or diffuse microcracking. Being able to detect these defects is essential to ensure the structural integrity over time. However, when the considered structure has a very large surface area, such as a bridge, it is complicated to monitor it exhaustively. To reduce costs, methods for continuous monitoring of structures and automatic detection of defects have been developed over time. These techniques are often based on the continuous recording of data from sensors that are assumed to reflect the health state of a structure as a whole. A drift of the measured quantities is expected in the event of a defect appearing within a structure [Farrar and Worden, 2007].

The main type of sensor used for structural health monitoring (SHM) applications is the accelerometer, which allows for a modal characterization of a structure (*i.e.*, an eigenfrequency variation over time is investigated [Rytter, 1993]). Other frequently used sensors include strain gauges and optical fibers, which give access to local strains [Benedetti et al., 2011, Bang et al., 2012]. They detect an increase in the measured strains over time, which then allows for damage detection. The main disadvantage of these techniques is that they extrapolate local data to obtain an estimate of the overall health status. A lack of sensitivity is to be feared for defects that remain latent for macroscopic characteristics of the structure until their growth becomes catastrophic. To alleviate that risk, turning to optical methods that allow for exhaustive views has been proposed [Coulthard, 1989, Jia et al., 2004, Bhandari and Deshpande, 2008]. The objective is then to automatically detect the presence of a defect on the structure surface. Such a principle is usually limited to thin structures.

At first glance, visible damage and more particularly cracks implies a local intensity variation on the structure surface. Algorithms exist to detect the contours of objects on images at pixel resolutions [Hildreth and Marr, 1980, Canny, 1986], and sub-pixel scales [Bouchara et al., 2007, Hermosilla et al., 2008, Hagara and Kulla, 2011]. These algorithms have inspired the development of methods for automatic recognition of surface defects on concrete samples [Dare et al., 2002, Yamaguchi and Hashimoto, 2010] or on bridges [Abdel-Qader et al., 2003] for instance. They can be coupled with the use of specific robots equipped with cameras connected to an image processing device for a fast and yet exhaustive inspection [Li et al., 2019].

The disadvantage of these techniques is that they lack robustness, because they are based on a gradient threshold. Its choice will greatly influence the type of detected discontinuity. To make these approaches more robust, couplings with deep-learning algorithms have been proposed. The algorithm is trained on a large number of images to recognize a particular defect [Mohamed et al., 2019, Dung, 2019, Dung et al., 2019]. The automatic detection then becomes more “customized” to a specific structure and/or material, but these techniques do not *ensure* damage detection. In addition, their

training requires a large set of data to be available. To increase their reliability, it has been suggested to train neural networks on several types of materials (assuming that they all share comparable defects) [Alipour and Harris, 2020].

Despite the use of deep-learning algorithms, the important drawback that remains with methods based on contour detection is that damage must be clearly visible on the surface with an apparent crack opening. If it is faintly visible or underlying, it may not be detected and such a risk is not acceptable for SHM purposes. When damage is present, be it apparent or not, it will necessarily have a local signature on the way the surface will deform when subjected to in-service loading. Digital Image Correlation (DIC) is a well known technique in the experimental field to measure surface displacement fields between reference and deformed states [Sutton et al., 2009, Hild and Roux, 2012b, Sutton, 2013]. Such a tool has been largely used to study damage phenomena [Périé et al., 2002, El Bartali et al., 2008, Munier et al., 2010, Roux-Langlois et al., 2015]. More precisely, methods using DIC have been developed to automatically detect damage within a structure, especially cracks. The simplest methods seek to detect large strains due to crack-induced displacement jumps. They have been extended to several fields such as masonry [Bolhassani et al., 2016], composite materials [Nag-Chowdhury et al., 2018] or renewable energies [Wu et al., 2019]. However, such methods may exhibit a poor robustness because, as for contour detection, threshold levels are difficult to estimate, especially if the structure is subjected to multiaxial loading.

The precise quantification of cracks by DIC in mechanical tests has been subject of numerous developments in order to determine the precise position of the crack tip [Roux and Hild, 2006, Yates et al., 2010], to calculate stress intensity factors in post-processing steps [McNeill et al., 1987, Rethore et al., 2005] and via integrated DIC [Roux and Hild, 2006, Hamam et al., 2007], or to study the entire crack path [Mathieu et al., 2012, Cinar et al., 2017]. Many of these techniques were not intended to automatically detect the presence of cracks on a surface, as they require a non-obvious initial calibration. However, they could be diverted to automate the detection. For example, in Ref. [Rupil et al., 2011], the displacement was initially sought on the basis of simple kinematic bases (*e.g.*, accounting for rigid body motions and uniform strains). Damaged areas then are synonymous for higher correlation residuals, which are obtained from image differences after registration. Based on the knowledge of the displacement field around a crack, it was then possible to iteratively adjust the position, orientation and length of several cracks within the area of interest. For this method, it is therefore necessary that the cracks be open, and that the deformations undergone by the structure be not too complex.

In order to gain robustness, methods have emerged based on the knowledge of the displacement field when the structure is sound. If, during the experiment or over time, a defect induces a variation in terms of displacement fields with respect to the *healthy* specimen, it will be detected using specific indicators. In Ref. [Zhao et al., 2019], a concrete sample was subjected to 4-point bending under increasing load over time. At each step, the displacement field measured via DIC was decomposed using wavelets. The comparison between the first load level and the following ones allows an indicator of energy drift to be established over all the decomposition stages. The occurrence of damage induced a variation in the decomposition form, which resulted in an increase in the error indicator. With such

a method, it is difficult to evaluate the sensitivity to the defect, especially since the example dealt with concrete that easily damages under bending. Moreover, the method seems complicated to calibrate because of the many possible variations for the wavelet decomposition. In Ref. [Eleftheroglou et al., 2018], a method for estimating the residual life of a drilled composite specimen in a tensile fatigue test was presented. Strains of the material were estimated by DIC at several instances of time during the test, always at the maximum load level. Through multiple tests, a life estimation model was calibrated using a learning algorithm. Over time, damage indicators were calculated to predict the remaining service life. This type of method using DIC is robust to identify structural damage when the test conditions are well known, and when several samples are available to calibrate the model. Its use in real conditions seems delicate given that model calibration involves complex algorithms. The objective of this work is to introduce a new autonomous structural health monitoring method based on DIC for structures that undergo statistically stationary loading during their lifetime, which is the case of many industrial structures. The idea lies in using very simple model order reduction methods to describe the displacement field viewed by a single or multiple camera(s). Such techniques have already been conducted using DIC data. First, in Ref. [Jailin, 2018] from 350 random time shots of a vibrating plate, 8 main modes of the structure were found by principal component analysis. These modes were orthogonalized with respect to the mass matrix of the finite element model in order to coincide with actual vibration modes. The comparison between these modes and the numerical predictions was conclusive. In Ref. [Wang, 2019], the 3D displacement fields measured during a thermomechanical test, which were initially very noisy, were decomposed on a reduced modal basis in order to reduce unphysical temporal fluctuations. In the case of that test, a unique mode was used to describe almost all the kinematics of the experiment. The idea of restricting the kinematic space has also been pursued for modal analysis [Passieux et al., 2018]. A unique sinusoidal temporal mode, which was related to the vibration mode, was used. The proposed method is decomposed into two steps. First, during the learning stage, a kinematic modal basis is determined from a set of pictures taken on the undamaged structure with a variety of (natural) loadings. In the second stage, namely that of health monitoring, new pictures are acquired, and the measured displacement fields are projected onto the initial modal basis. This second step consists, in fact, in performing a large number of times “integrated DIC”. It utilizes finite element shape functions extracted from a model or inspired by physics. If a defect initiates, differences appear in global error indicators that will highlight it either from displacements or correlation residuals. In order to simplify image processing of this second step, a new “one-step DIC” strategy is introduced, which reduces DIC processing to a mere scalar product of the difference between current and reference images with one extractor field per mode. This DIC scheme is performed on filtered images, where the filter is tailored to the observed displacement field. The method is illustrated on a fatigue crack propagation experiment.

4.1.2 Damage detection via DIC

Model order reduction

Principle Model order reduction techniques are used to reduce the number of degrees of freedom grouping a set of fields. The Principal Component Analysis (PCA) [Jolliffe and Morgan, 1992], which is similar to the Proper Orthogonal Decomposition (POD) [Chatterjee, 2000], is used to bring out the most important information in data sets. Let us consider a problem with n spatial degrees of freedom whose solutions are available at n_t time steps. The matrix $[\mathbf{A}]$ is the concatenation of solutions in time, then its dimension is $n \times n_t$. PCA gives a factorization of a rectangular matrix $[\mathbf{A}]$

$$[\mathbf{A}] = [\mathbf{V}][\mathbf{\Sigma}][\mathbf{U}]^\top \quad (4.1)$$

where $[\mathbf{V}]$ is the $n \times n$ matrix of the orthonormal spatial modes that form a canonical basis $\psi_i(\mathbf{x})$, $[\mathbf{\Sigma}]$ the $n \times n_t$ diagonal matrix where the non-zero terms are considered as the singular values of the matrix, and $[\mathbf{U}]$ the $n_t \times n_t$ matrix of orthonormal temporal modes denoted by $\phi_i(t)$ in the sequel. From this decomposition, the singular values account for the importance of the modes in the decomposition. The higher the value, the more important the mode for the global field description. Such a method is applied to a set of displacements field \mathbf{u} measured via DIC

$$\mathbf{u}(\mathbf{x}, t) = \sum_{i=1}^n \alpha_i \phi_i(t) \psi_i(\mathbf{x}) \quad (4.2)$$

with \mathbf{x} denoting the pixel position, t the temporal index, α_i the i -th singular value, ϕ_i the i -th temporal mode and ψ_i the corresponding i -th spatial mode, where both ϕ_i and ψ_j are normalized.

This set of modes can be truncated and it results in efficient data reduction. The selection of the appropriate number n_a of modes is based on α_i values. If they reach levels close to measurement uncertainty, the mode is no longer relevant to adequately describe the displacement fields. The approximate displacement field \mathbf{u}_a is then defined as

$$\mathbf{u}_a(\mathbf{x}, t) = \sum_{i=1}^{n_a} \alpha_i \phi_i(t) \psi_i(\mathbf{x}) \quad (4.3)$$

Uncertainty consideration It is noteworthy that, implicitly, the metric used for model reduction is the (Euclidean) L_2 norm. A relevant metric in the case of model reduction is that related to measurement uncertainty [Neggiers et al., 2018]. For DIC, this information is contained in the DIC matrix $[\mathbf{M}]$. Its consideration in model order reduction is completed by weighting the mesh nodes displacement values by the square root of the DIC matrix. PCA then gives

$$[\mathbf{M}]^{\frac{1}{2}}[\mathbf{u}] = [\mathbf{\Psi}^*][\mathbf{\Sigma}^*][\mathbf{\Phi}]^{*\top} \quad (4.4)$$

where $[\Psi^*]$ is the matrix related to the spatial modes, $[\Sigma^*]$ the diagonal matrix, $[u]$ the matrix gathering in columns the measured spatiotemporal displacement field, and $[\Phi^*]$ the matrix associated with the temporal modes. It is worth noting that the columns of $[\Psi^*]$ are no longer displacements. The related displacement modes ψ_i become

$$\{\Psi_i\} = [M]^{-\frac{1}{2}}\{\Psi_i^*\} \quad (4.5)$$

with $\{\Psi_i^*\}$ the i -th column of $[\Psi^*]$. The PCA technique is performed based on a truncation of the diagonal matrix $[\Sigma^*]$, thereby leading to a consistent model reduction based on the statistical properties of random uncertainties affecting the processed data (*i.e.*, images).

Damage detection

The modal displacement basis is set up from a large number of images when the structure is subjected to statistically repeated loading. This step is the learning stage of the proposed method, and the structure is assumed to be sound (*i.e.*, undamaged). These images can be pre-processed by “subtracting” rigid body translations by FFT-DIC for instance [Hild et al., 2002]. To account for illumination variations that may occur, brightness and contrast corrections are applied after seeking for the displacement, as these variations remain small. Q8 shape functions are used (see Section 3.2.4). From this data gathering, the statistics about the modal amplitudes and residuals are deduced. A drift in those levels is synonymous for damage occurrence.

During the monitoring phase, new pictures are acquired multiple times and displacements are measured. These fields are projected onto the *sound* (*i.e.*, undamaged) modal basis, and a projection gap is deduced. This error is calculated as the difference between the displacement initially measured by DIC and that resulting from its projection onto the considered modal basis. For damaged states, the error will increase because damage was not integrated into the modal basis. Thus, based on displacement and also DIC projection residuals, error indicators can be set to detect damage onset.

4.1.3 Case study: Fatigue crack propagation

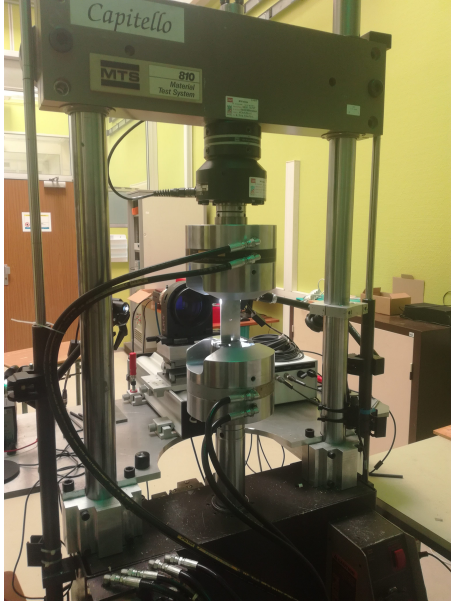
The main features of the proposed method are illustrated in this section, which is based upon an experimental case study dealing with crack propagation.

Mechanical experiment

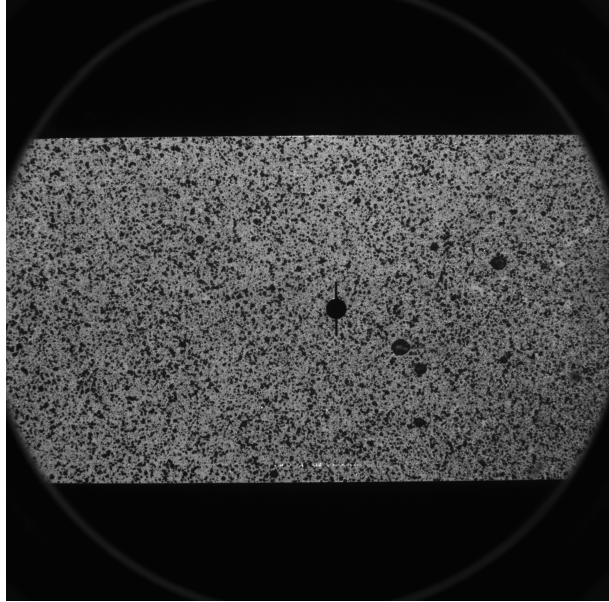
The experiment consisted in testing a Center Cracked Tension (CCT) specimen made of 2024 aluminium alloy. This material is classically used in aeronautics and aerospace industries. The sample size was $150 \times 50 \times 2$ mm with an 8 mm pre-notch machined via EDM from a 3 mm in diameter hole. One side of the sample was speckled with black and white paints for DIC purposes. The same specimen geometry was used in Ref. [Gamot et al., 2019]. The set up is shown in Figure 4.1.

The hardware parameters of the optical setup are reported in Table 4.1.

First, the specimen was subjected to a cyclic loading at 10 Hz with a tensile force of 8 kN for 7,500 cycles in order to initiate two cracks. Then the specimen was sinusoidally loaded at a frequency of



(a)



(b)

Figure 4.1: (a) Experimental set up. (b) Specimen surface monitored by the camera

Table 4.1: DIC hardware parameters

Camera	Allied Vision Manta G-145B
Definition	2048 × 2048 px
Gray Levels amplitude	16 bits
Telecentric lens	Edmund Optics ×0.125
Field of view	100 × 100 mm ²
Image scale	50 μm/px
Stand-off distance	25 cm
Image acquisition rate	1 fps
Patterning technique	sprayed paints
Pattern size	7 px

0.1 Hz with strains up to 5×10^{-4} , which corresponded to 3 kN approximately. 150 images were acquired twice. The frequency of image acquisition was 1 Hz. Thus 10 pictures per period of loading were available. In the following, the initial step will refer to the first 150 images. It corresponds to the *learning stage*, and the modal basis is set up at this step. The second set of 150 images will be referred to as step 1. It will serve as reference to compare to the results obtained at the initial step, because both sets of pictures were acquired for the same damage state. Then, series of 10,000 cycles at a maximum force of 7 kN were conducted at a frequency of 10 Hz and the crack continued to propagate. Between each propagation phase, 150 images were taken under the same loading as for the initial step. 3 new sets of images are available. They are referred to steps 2 to 4.

Figure 4.2 shows the mesh used for this work. It is made of 3-noded triangular (T3) elements. On the right side of the ROI, a (red) box is selected to pre-calculate the rigid body translations of the specimen, thanks to FFT-DIC. The displacements obtained in both directions were stored and removed from the total displacement fields for PCA purposes.

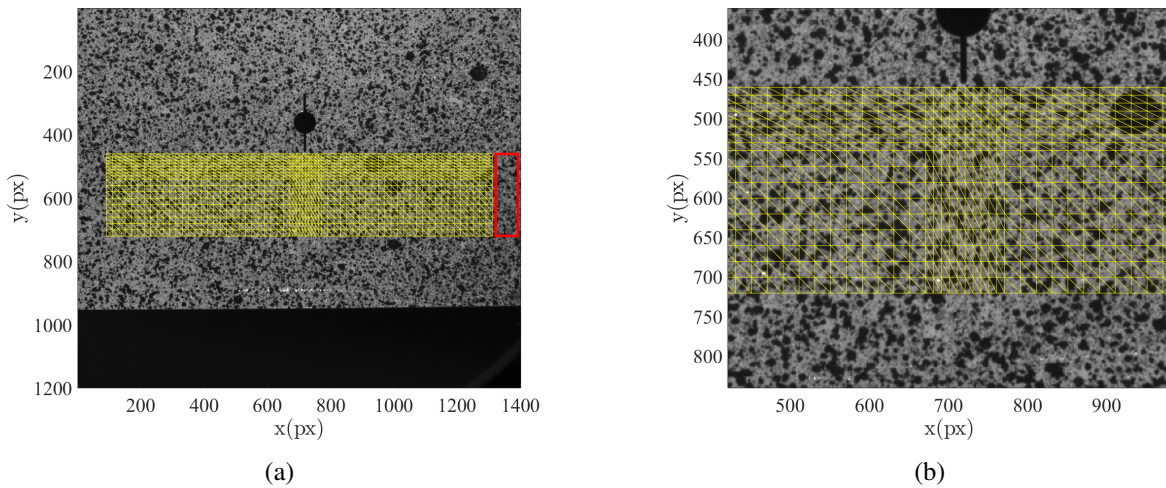


Figure 4.2: (a) Mesh used in T3-DIC analyses. The red rectangle is the region used to pre-calculate the rigid body translations. (b) Zoom of the mesh showing the refinement close to the crack tip.

The DIC analysis parameters are gathered in Table 4.2.

Table 4.2: DIC analysis parameters

DIC software	Correli 3.0 [Leclerc et al., 2015]
Image filtering	none
Element length	10/20 px
Shape functions	linear (T3)
Mesh	regular
Matching criterion	see text
Interpolant	cubic
Displacement noise-floor	0.024 px

Damage detection by DIC

This subsection first presents the results obtained with model order reduction techniques applied to DIC data from the calibration phase. Then, the results on defect identification based on several error indicators are illustrated.

Model order reduction As explained in Section 4.1.2, the mode relevance is related to its singular value. The set of singular values is plotted in Figure 4.3(a) for the analyzed sequence. The singular value associated with the first mode is one order of magnitude higher than the others. This observation means that it contains most of the kinematic information. The loading being unidirectional, the first mode is associated with tension. It will be confirmed in the sequel.

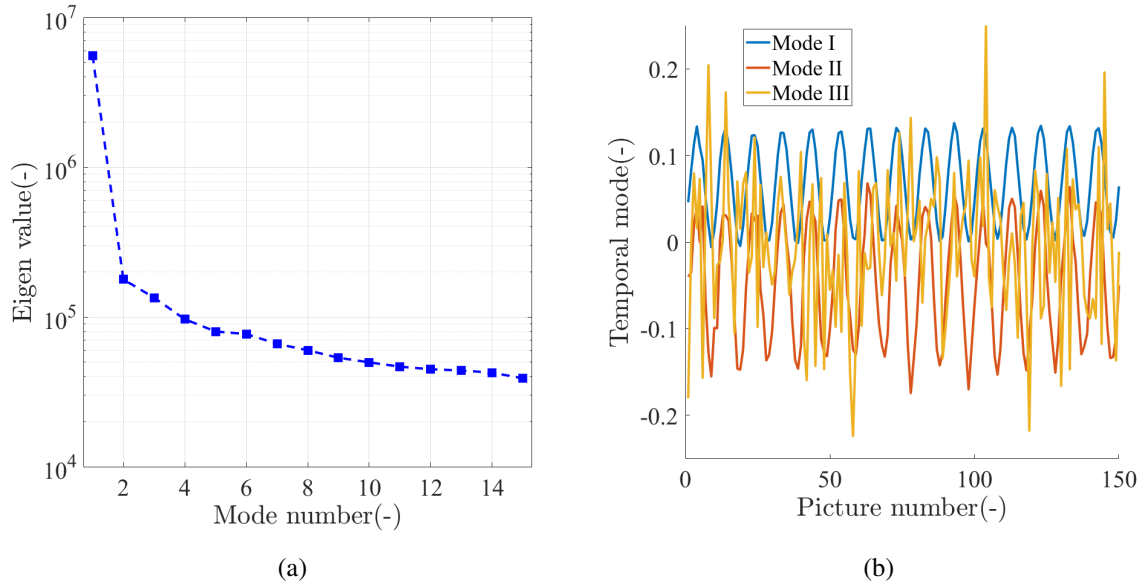


Figure 4.3: (a) Eigen values associated with the first 15 modes. (b) Temporal modes $\phi_i(t)$.

The eigenvalues related to the other modes stabilize from the fourth mode on. Thus, it is concluded that three modes are sufficient to describe the whole kinematics. The first three spatial modes are displayed in Figures 4.4, 4.5, and 4.6 respectively. For the first mode, both raw and corresponding displacement modes are displayed. The raw modes are more difficult to “read” to due to the $[M]^{1/2}$ weighting. As expected, the first temporal mode $\phi_i(t)$ is sinusoidal (Figure 4.3(b)), and its spatial representation is relative to tension. The second temporal mode is also sinusoidal. The third temporal mode is more difficult to interpret.

Only the second and third associated displacement modes are displayed. The physical meanings of these modes are difficult to tell, contrary to the first one.

Error indicators related to displacements In order to automatically detect the presence of damage, error indicators are introduced. The measured displacement field is projected onto the modal

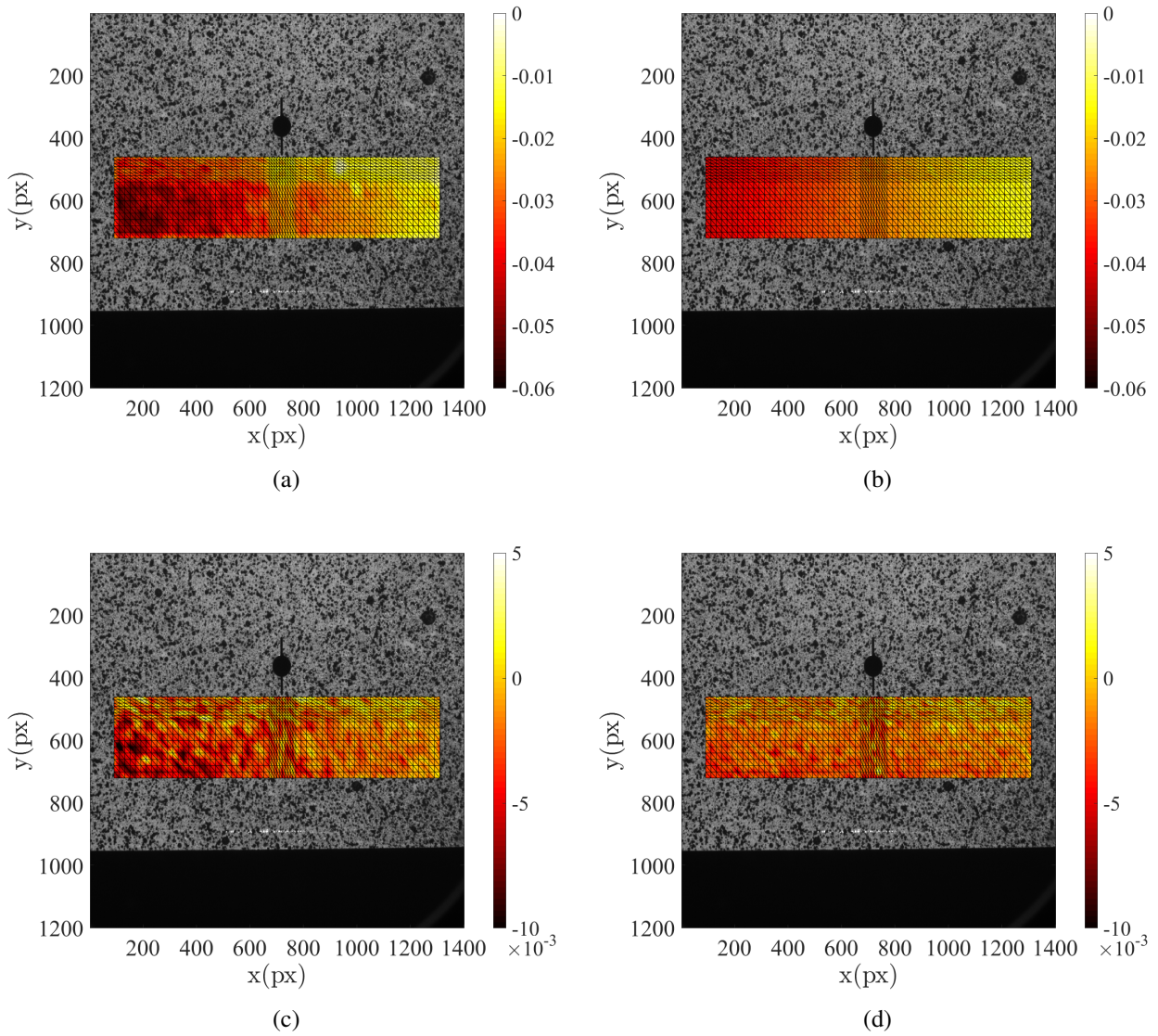


Figure 4.4: (a,c) First spatial mode Ψ_1^* respectively along x and y directions. (b,d) Corresponding displacement modes Ψ_1 .

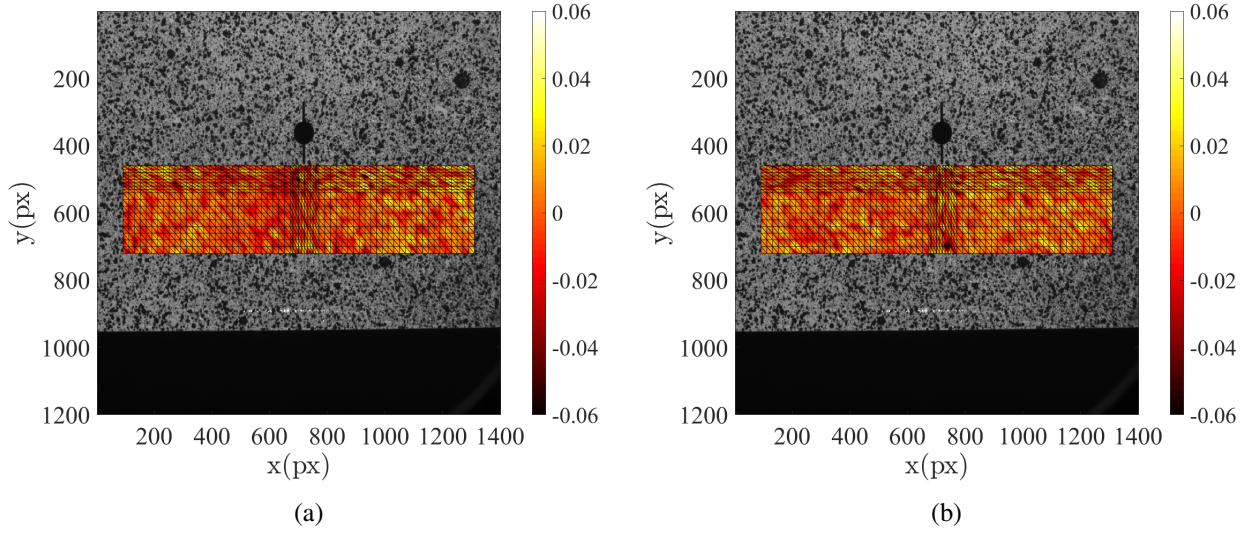


Figure 4.5: Second spatial mode Ψ_2 along x (a) and y (b) directions.

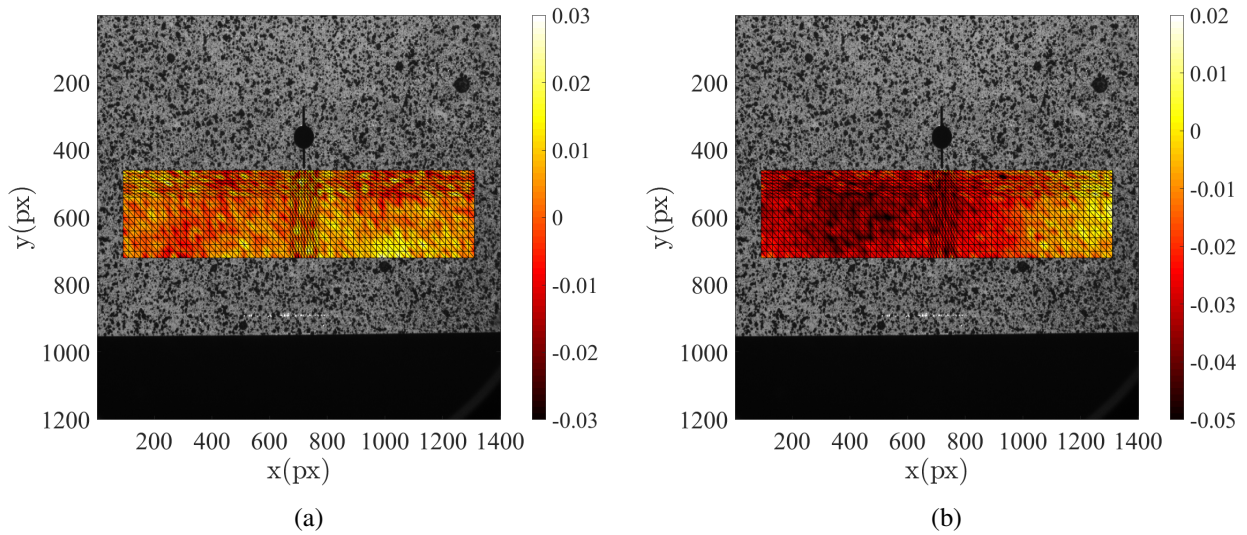


Figure 4.6: Third spatial mode Ψ_3 along x (a) and y (b) directions.

basis determined during the learning phase. Displacement error vectors are obtained by subtracting the projected displacement fields to those initially measured by DIC at mesh nodes. From these error vectors, indicators are constructed, namely, the standard deviation and the maximum level. The indicators are plotted for the initial step and steps 1 to 4 in Figure 4.7. It was found that 3 modes were sufficient to describe the whole kinematics. However, the influence of the number of modes on the error levels is also studied hereafter. The indicators are plotted for 3 and 6 projection modes. For each step, the mean values of the error indicators are reported.

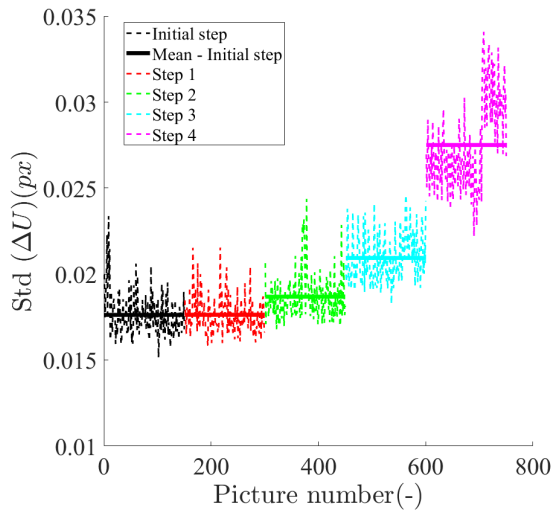
First, the more the specimen is damaged (*i.e.*, the crack propagated), the higher the mean values of the error indicators. The latter ones fluctuated significantly, which stresses the importance of considering mean values over a certain period of time. This observation is even more relevant when the loading is random. The comparison of the results obtained with 3 and 6 modes suggests that the average value and the fluctuation decreases with basis enrichment for the standard deviation. For the maximum error, this trend is less obvious. Thus, a good way to evaluate the indicator drift is to normalize the difference between the mean values over the initial step and the other steps by the fluctuations (*i.e.*, the standard deviation) of the initial step, as shown in Figure 4.8. The higher the number of modes, the more discriminating the presence of a crack for the normalized standard error. It is not the case for the normalized maximum error. For step 1, where the specimen state is the same as at the initial step, the damage indicators are really close to those obtained at the initial step. This observation confirms the ability of the method to apply when the specimen is not damaged.

Displacement error fields In order to ensure that the projection error is localized near the crack tip, the corresponding fields are displayed in Figure 4.9. As the crack propagates, the displacement error around its tip increases. In addition, a residual displacement is observed due to the presence of the crack.

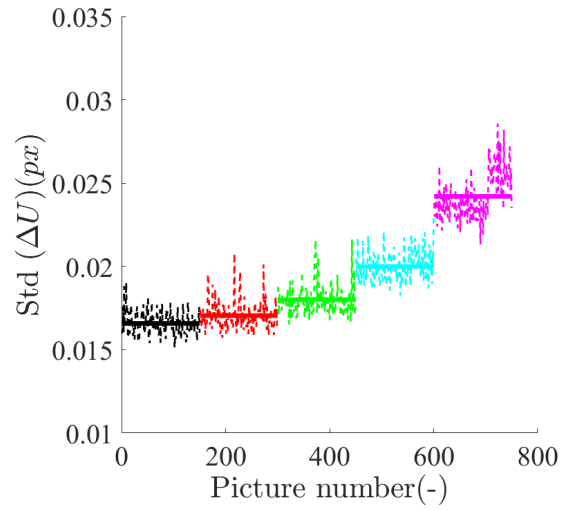
This phenomenon results in repetitive location of the error maximum (Figure 4.10). The two nodes where the maximum errors occurred at step 3 are in the vicinity of the crack tip.

DIC residuals An additional information is available thanks to the DIC residuals. When DIC computations are performed and the solution is close to the actual displacement field, the residuals reduce to intrinsic camera noise. This is true under the condition that brightness conservation (3.1) be fulfilled. To be satisfied, no illumination variations should occur. Otherwise, brightness and contrast (BC) corrections should be performed. If the displacement field is not rich enough to completely account for the gray level variations, its root mean square (RMS) will be higher. It may be due to mesh coarseness with regard to the displacement complexity, or discontinuity in the displacement field.

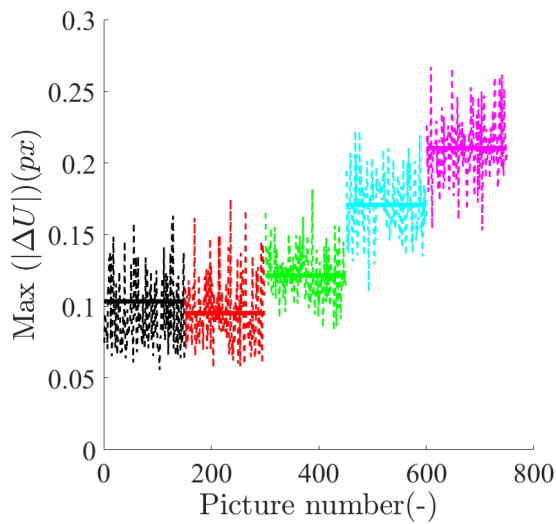
The experiment studied herein lasted 5 hours. Major illumination variations were prevented using artificial lighting but smaller ones unavoidably occurred. Brightness and contrast corrections were applied after the DIC computation was performed. They were performed with one Q8 element over the whole ROI. The RMS residuals before and after BC correction are plotted in Figure 4.11. The correction has little impact on the levels (*i.e.*, about few gray levels for a 16-bit dynamic range), which



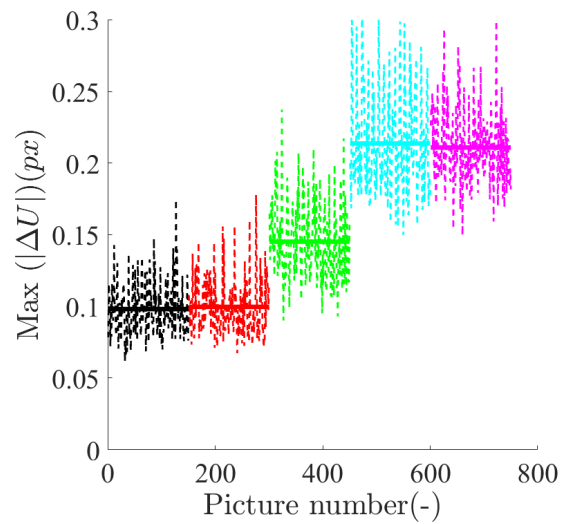
(a)



(b)



(c)



(d)

Figure 4.7: Projection displacement error indicators for all five steps. (a,b) Standard deviation for 3 and 6 modes respectively. (b,d) Corresponding maximum levels.

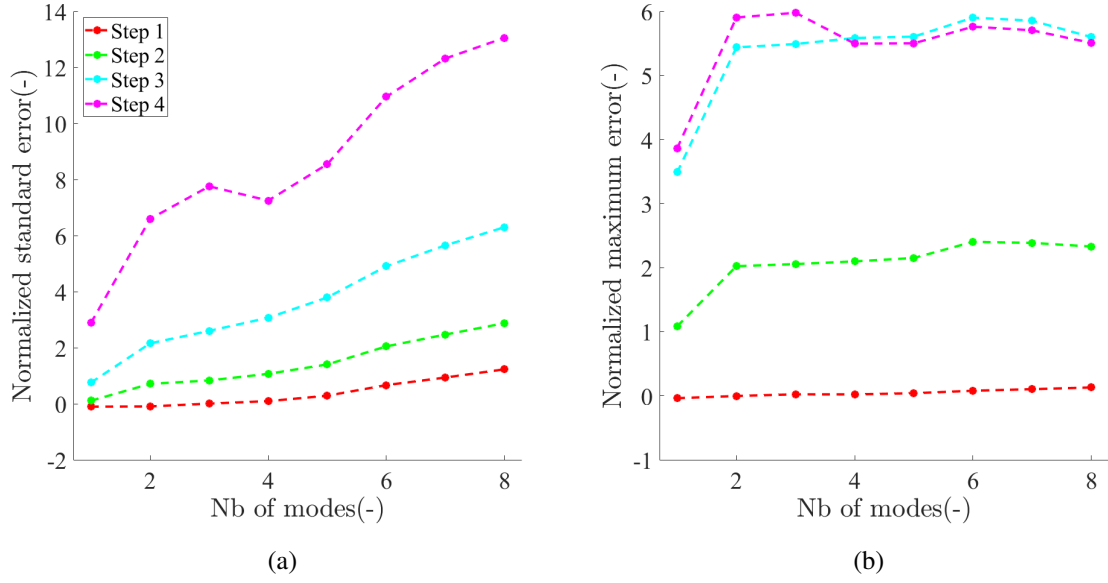


Figure 4.8: Normalized standard deviation (a) and maximum (b) displacement errors as functions of the number of modes.

confirms the very small illumination variations. Along the experimental steps, the RMS residual increases even after BC corrections. This means that the measured displacement field does not fully describe the actual kinematics of the test (*i.e.*, the presence of the crack). The refinement with linear T3 elements in this area is not sufficient for fully describing the local complexity of the displacement field. Thus an increase in the residual norm is also an indicator of damage.

The DIC residual fields were also computed after displacement projection onto the modal basis. The mean and standard deviation of the displacement error indicators decreased as the selected number of modes increased. This is not the case for the RMS residuals. The RMS level is bounded by intrinsic camera noise and by interpolation errors. To evaluate the impact of the projection onto the modal basis, the residual difference before projection and after projection is calculated for the different steps of the experiment and plotted in Figure 4.12. It is observed that damage influenced more the residuals after projection. The higher the damage level, the higher the projection error. For step 2, the influence is really small, the difference with the values obtained at the initial step are largely due to interpolation errors. For step 4, the error due to modal projection is equivalent to that due to interpolation error. Thus, it is concluded that residuals are also a damage indicator, and displacement modal projection highlights it.

4.1.4 New DIC approach based on optimal extractors

In the following, the concept of optimal extractors and “one-step” DIC will be presented.

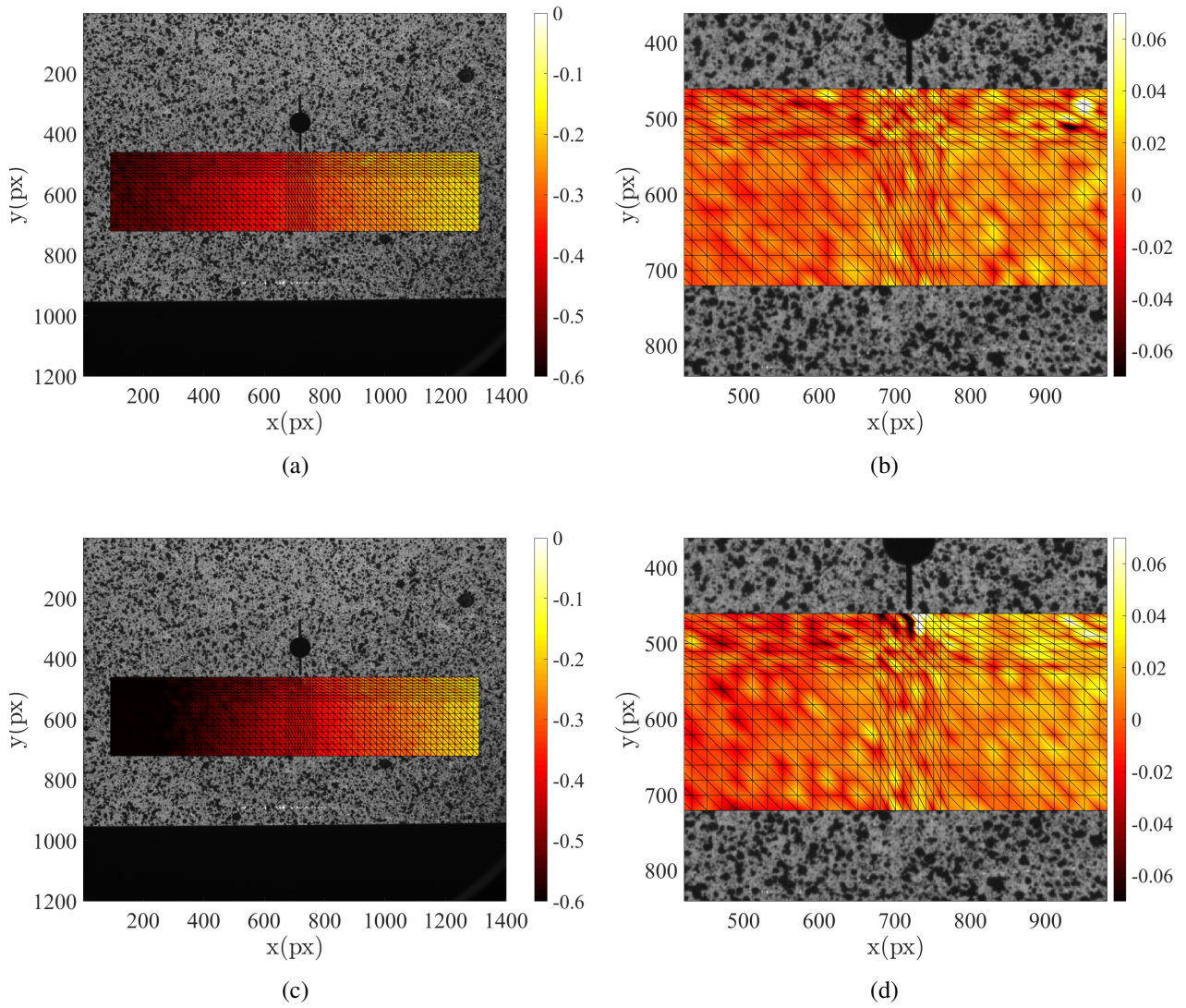


Figure 4.9: Displacements fields (expressed in px) along the x-direction for steps 1 (a) and 3 (c), and the corresponding projection errors (b,d).

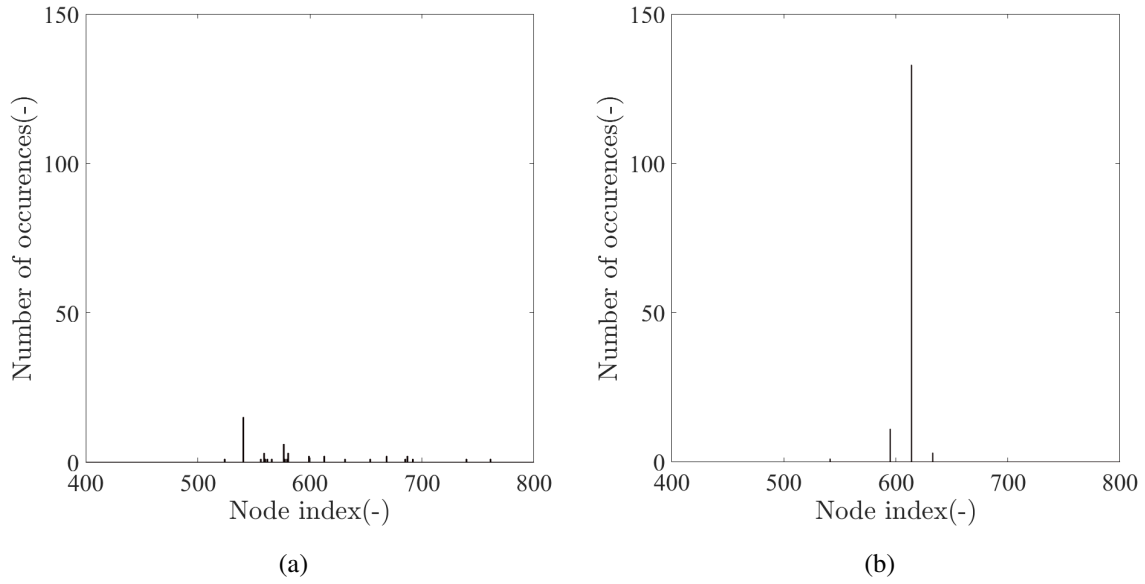


Figure 4.10: Locations of maximum error for the steps 1 (a) and 3 (b).

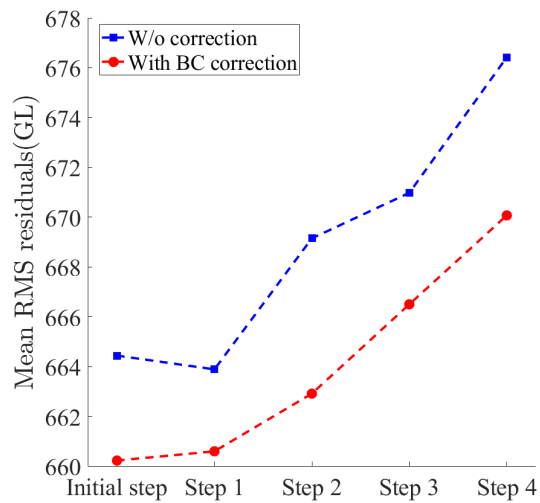


Figure 4.11: Comparison of mean RMS residuals before and after BC corrections for the five steps.

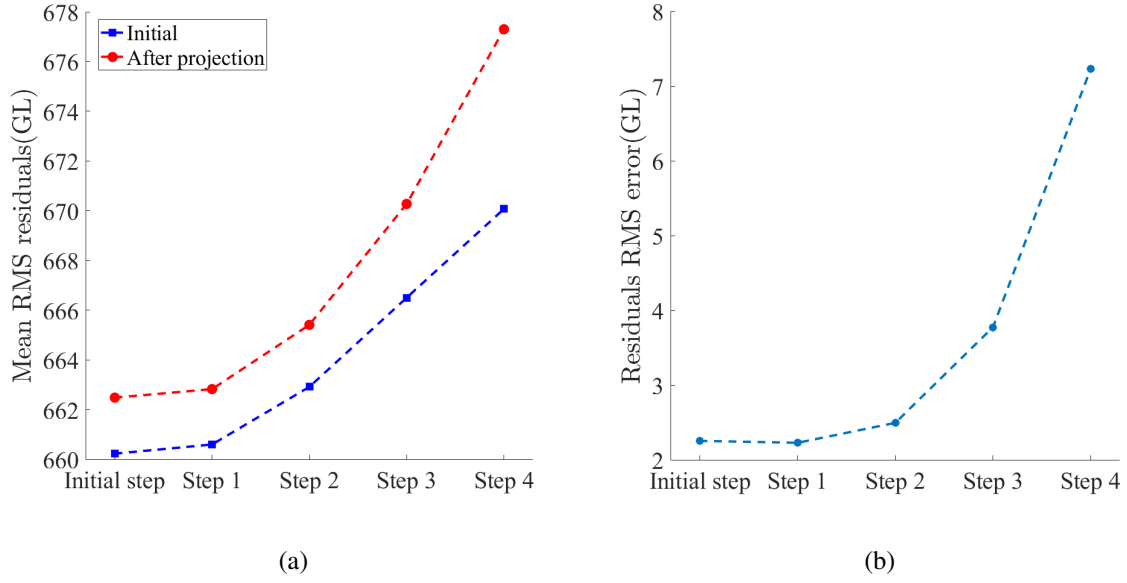


Figure 4.12: (a) Comparison of RMS residuals with direct DIC and after projection onto the modal basis. (b) Error induced by projection onto the modal displacement basis.

Optimal extractors

“Integrated DIC” consists in using as a kinematic basis a space generated by a reduced set of fields motivated by the problem under study [Roux and Hild, 2006]. For instance, the displacement field of Euler-Bernoulli beams subjected to flexural loading is measured with only six degrees of freedom per beam [Hild et al., 2009]. This technique reduces the number of unknowns of the DIC problem, and thus the associated measurement uncertainties. In the first phase, which consists in learning, an appropriate displacement (modal) basis has to be set. This modal basis could be used directly as generalized shape functions. Thus, it is noted that the same reference image and kinematic basis can be used repeatedly. Hence it is worth precomputing all these repetitive aspects with what is called *optimal extractors* to accelerate the calculations. The underlying theory is presented in the following.

For each spatial mode Ψ_i , which was determined during the learning phase, it is possible to determine its sensitivity field s_i

$$s_i(\mathbf{x}) = \Psi_i(\mathbf{x}) \cdot \nabla \hat{f}(\mathbf{x}) \quad (4.6)$$

Introducing the matrix $[N]$

$$N_{ij} = \sum_{k=1}^{N_x} s_i(\mathbf{x}_k) s_j(\mathbf{x}_k) \quad (4.7)$$

with N_x the number of pixels, and k the associated label, it is possible to define an extractor field $\zeta_i(\mathbf{x})$, for each mode i , such that

$$\zeta_i(\mathbf{x}) = \sum_{j=1}^{n_a} N_{ij}^{-1} s_j(\mathbf{x}) \quad (4.8)$$

where N_{ij}^{-1} is the ij component of the inverse of the $[N]$ matrix.

The amplitude $\chi_i(t)$ associated with the modal field $\Psi_i(\mathbf{x})$ is determined by the scalar product of the extractor field with the difference field $\rho(\mathbf{x}, t) = g(\mathbf{x}, t) - f(\mathbf{x})$, which is again the difference in gray level between the deformed image g and the reference image f

$$\chi_i(t) = \sum_{k=1}^{N_x} \zeta_i(\mathbf{x}_k) \rho(\mathbf{x}_k, t) \quad (4.9)$$

The correlation residual η is calculated as the difference between the initial residual and the gray levels variation induced by the modal displacement updates

$$\eta(\mathbf{x}, t) = \rho(\mathbf{x}, t) - \sum_{i=1}^{n_a} \chi_i(t) s_i(\mathbf{x}) \quad (4.10)$$

Thus, the main interest lies in the fact that for any number of deformed images, the extractors are computed once for all. One new image requires a subtraction and a scalar product. These simple operations can be processed very fast (*e.g.*, using GPU).

“One-step” DIC

From the learning stage, the statistics about the displacement amplitudes is also available. With such information, the goal is to speed up further the DIC analyses yielding a good solution in one single step. DIC deals with nonlinear minimizations, based on iterative schemes [Sutton et al., 2009, Hild and Roux, 2012b]. For each iteration, the summand of the cost function is linearized to compute incremental corrections to the sought degrees of freedom. This operation can be rephrased as computing the variation of the local gray level of the image is equal to the scalar product of the displacement by the gradient of the image. When the displacement is too large, the linear gray level variation approximation with the displacement is no longer valid, which implies that several iterations are necessary to converge to a satisfactory result.

One way to reach the right solution in a unique iteration is to perform appropriate image filtering. The filtering of an image consists in erasing details below a certain λ scale, often considered as constant over the whole ROI. This filtering operation is performed by convolving the initial image with a filtering kernel (*e.g.*, a Gaussian), which tends toward zero for a distance to the origin greater than λ . The information is spread over an area covered by the filtering length. The gradient variations of the filtered image are thus attenuated. Such type of approach was already used in multiscale DIC [Hild et al., 2002]. DIC computations were iteratively performed with progressively unblurred images. It enables for rapid convergence toward coarse solutions. Consequently, the following computations are initialized with previous displacement fields and then global convergence is faster as more details are restored in the image and in the displacement field.

Filtering is a way to restore DIC linearity. Estimating the correct displacement field in one single iteration is accessible provided appropriate image filter is used. The needed filtering is directly related

to the displacement amplitude. When displacement amplitudes are small (*i.e.*, less than 1 px), it is assumed that homogeneous filtering is sufficient due to small gray level variations. A simple test case to ensure this assumption consists in calculating the best optimal filtering length to estimate rigid body translations with “one-step” DIC. A smooth Gaussian kernel was used, from the *Matlab* function *imgaussfilt* [Higham and Higham, 2017]. In 2D, an isotropic Gaussian filter G_f has the form

$$G_f(x, y) = \frac{1}{2\pi\lambda^2} \exp\left(-\frac{x^2 + y^2}{2\lambda^2}\right) \quad (4.11)$$

where x and y are the pixel coordinates, λ the “filtering length” as called in this work. The same image and ROI were selected as in the previous section. The “deformed” images are artificially created with bi-cubic gray level interpolation. For each translation amplitude, the optimal filtering length is the one that minimizes the displacement error. Figure 4.13 shows that for subpixel displacement amplitudes, the filtering length is independent of the applied amplitude.

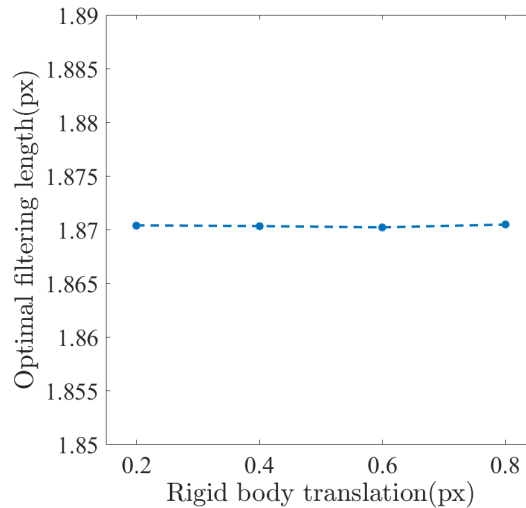


Figure 4.13: Optimal filtering length for subpixel rigid body translations.

In the following, the application of one-step DIC is developed for sub-pixel displacements. In the Appendix B, a virtual application case is set for displacements greater than 1 px. In particular, homogeneous filtering is no longer optimal, and another filtering strategy must be set.

4.1.5 Application of one-step DIC

In this section, first the calibration of the optimal filter length is carried out. Then, the application of “one-step” DIC is performed on the test case.

“One-step” DIC calibration

The method quality is evaluated by measuring the difference between the displacement measured via T3-DIC projected onto the modal basis and that obtained by “one-step” DIC. The objective is to find

the optimal filter length that minimizes the displacement error over the whole set of pictures of the learning step. Several filtering lengths were tested ranging from 1 to 3 px. Three displacement modes were chosen. The results are plotted in Figure 4.14. It is found that the optimal filtering length is about 2.4 px. It is close to the previous (1.9) value found for rigid body translations. Moreover, the error fluctuation over the whole set of images tends to decrease with filter length increase. The error magnitude is correlated with the displacement amplitude. It is seen that excessive filtering with regard to local displacement magnitude may induce a loss of information. Being more accurate with high displacement amplitudes induces to be less accurate with lower amplitudes.

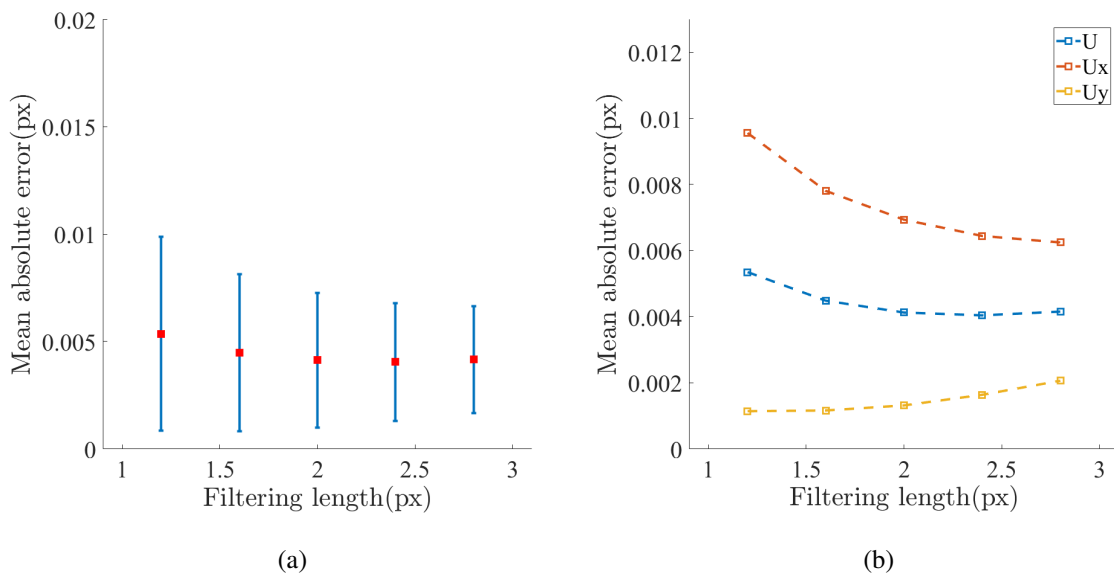


Figure 4.14: (a) Mean “One-step” DIC absolute error and its standard deviation over the whole set of images from the learning step. (b) Results detailed along each direction.

Regarding the error along both directions, it is higher in the x -direction, along which the tensile load is applied. The error increases with filtering length along the y -direction. The overall absolute error is about 4×10^{-3} px, and 7×10^{-3} px in the x -direction. These levels are comparable with those of DIC uncertainties [Sutton et al., 2009, Hild and Roux, 2012b]. Such observation validates the implementation of this new technique. The fluctuations represented by the standard deviation are about 2×10^{-3} px for the displacement amplitude, and 5×10^{-3} px along the x -direction.

4.1.6 Example of extractor

The extractor defined in Equation (4.8) associated with the first mode and an original image optimally filtered are displayed in Figure 4.15. The extractor is directly linked to its corresponding mode shape. For example, for mode 1, the highest values of the extractor are on the left part where the displacement mode amplitudes are the highest.

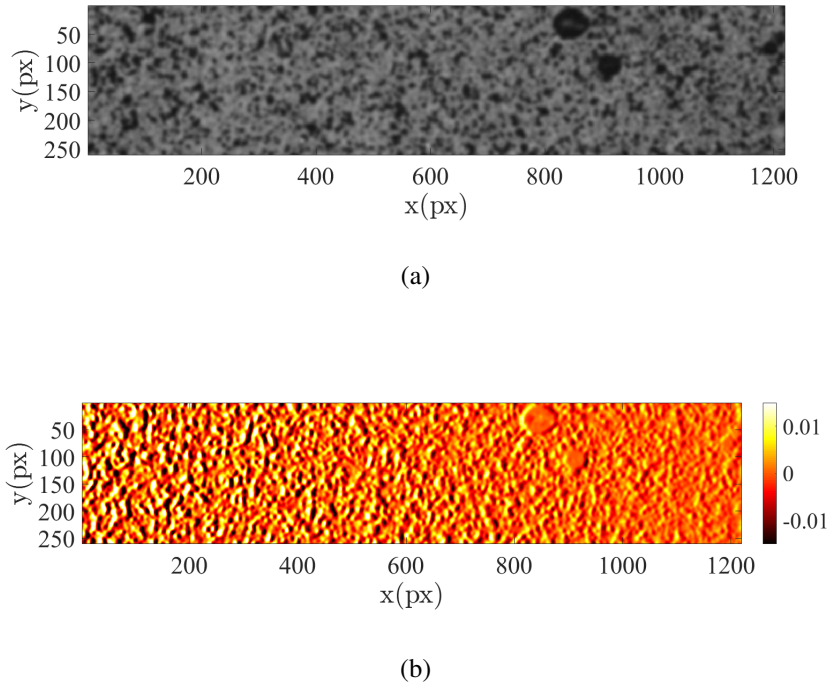


Figure 4.15: Filtered image (a) and extractor (b) for the first mode.

“One-step” DIC application

The one-step DIC calculation was performed over the full sets of homogeneously filtered images. The filtering length was equal to 2.4 px as explained in the previous section. The mean values of RMS residuals are shown in Figure 4.16. The difference between the residuals levels obtained at the initial step and the other steps are compared for both T-3 DIC and “one-step” DIC are also reported. First, the mean RMS level is approximately six times lower and its standard deviation is two times lower after filtering. It is due to the information local averaging. However, the residual difference between the initial step and the others is nearly the same with T3-DIC and one-step DIC. Thus, by weighting the residuals levels difference by their mean values, the jump to damage would be easier to spot.

4.1.7 Conclusion

In this work, a new method of structural health monitoring by DIC was proposed. This technique applies to structures that undergo the same loads repeatedly or statistically over time. Thus the deformations undergone by the surface of the structure depend on a limited number of parameters. All the measured displacement fields were condensed on a reduced kinematic basis. The method consisted of two steps:

- First, the kinematic basis was established. The selection criterion for the number of modes was based on the eigenvalues extracted from singular value decomposition of the measured spatiotemporal displacement field.

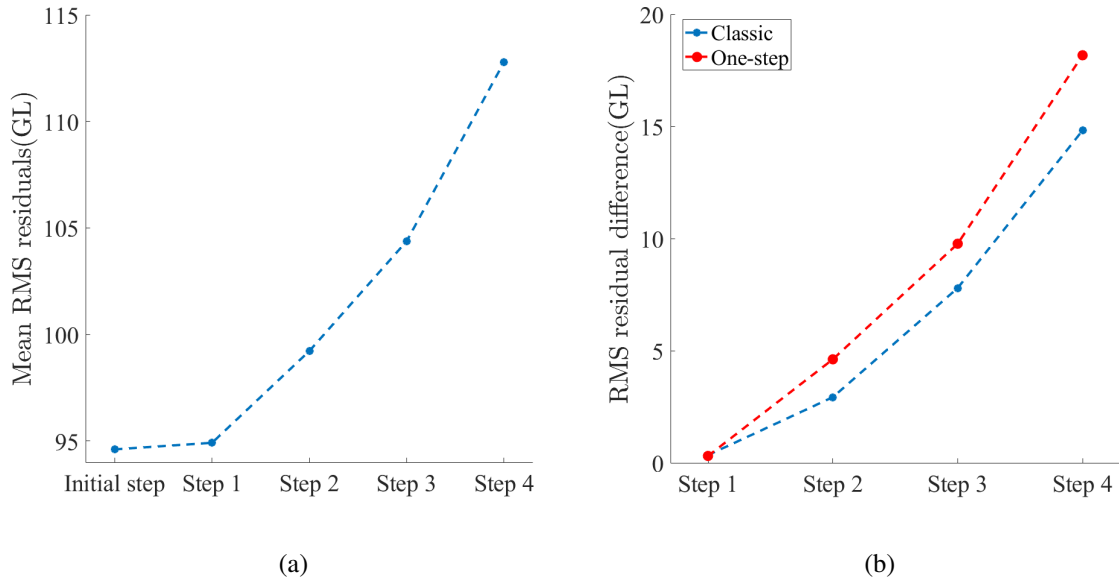


Figure 4.16: Mean RMS residuals after one-step DIC (a). RMS residuals differences between the initial step and the other steps for both T3-DIC and “one-step” DIC.

- Then, over time, the displacement fields measured by DIC were projected onto the kinematic basis. Global error indicators made it possible to determine, over a large sample of images, whether an error was present in the displacement field, and thus a defect that would be the source of this error.

The application case of this method also led to the establishment of the development of fast (*i.e.*, “one-step”) DIC. The idea is to perform the DIC process in one single iteration. Starting from the calibration step of the kinematic basis, global modes and a map of maximum displacements were available. The use of an adapted filter allows the validity of the linear tangent operator of DIC to be extended. Hence, convergence is expected in a single iteration. This method was improved by pre-calculating image extractors based on kinematic modes. Then the error indicator coincided with the correlation residuals.

In terms of perspectives, it is envisaged to use this SHM technique in more complex situations. Multi-directional tests would be interesting to carry out because the modal basis would be of higher dimension. It may also be interesting to study the accuracy of one-step DIC on more complex deformations. In terms of error indicators, global values (standard deviation) and local values (maximum) for the displacement were reported, but only global values for the residuals (RMS). The ROI may be divided into squares or rectangles, and the RMS residuals may be evaluated over these smaller zones. Damage may be detectable earlier than with global indicators.

4.2 Logistical aspects

This part is dedicated to discussing about the practical implementation of the DIC method to a wind turbine tower. The presented system is patented.

4.2.1 Device

It has been explained that cracks are found at some material-weld junction. For classical towers, there are welding lines every 3 meters approximately. The stress is not equally distributed over the whole section. Generally the hot spot area lies between 10 and 40 m from the base. Thus, it represents approximately ten welding sections to check exhaustively. It is possible to set the cameras circumferentially on each section. A wind turbine tower diameter is about 10 meters, if each camera covers about 1 m^2 of surface area 10 cameras will be needed per section. It can also be assumed that a camera be put onto a rotating stage and take photos over 360 degrees.

4.2.2 Needed measurement resolution

In this subsection, a simple illustration case is presented to estimate the measurement uncertainty to spot damage before it becomes critical. To be detected, the damage must have a sufficient kinematic signature with regard to measurement uncertainty. The tension of a bi-dimensional cracked specimen is simulated with several crack lengths with a 50 MPa loading. Such stress level is approximately the maximum recorded on site under normal operation [Gao et al., 2019, Tibaldi et al., 2016]. From the results of Section 2.4, a 30 cm long crack can be critical under storm conditions. The displacement jumps are plotted in Figure 4.17.

The simulation parameters are gathered in Table 4.3.

Table 4.3: Simulation parameters .

l_{crack}	10 to 40 cm
L	1.5 m
σ	50 MPa

The influence of a 30 cm long crack is about 0.2 mm. To be conservative, a factor 2 is taken to ensure the capacity of detection between measurement uncertainty and displacement perturbation. It means that a measurement uncertainty of 0.1 mm is needed to make the system reliable. Generally, one would mention the uncertainty directly in pixels [Hild and Roux, 2012b]. As already explained, the expected field of view with such a set up is about 1 m^2 . Considering a camera with a definition of 1000×1000 pixels, the needed measurement uncertainty is about 0.1 px. 0.05 px would be needed to spot crack with a 25 MPa load, which is more common. Such values can easily be reached with classical scientific cameras [Hild and Roux, 2012b, Curt et al., 2020b].

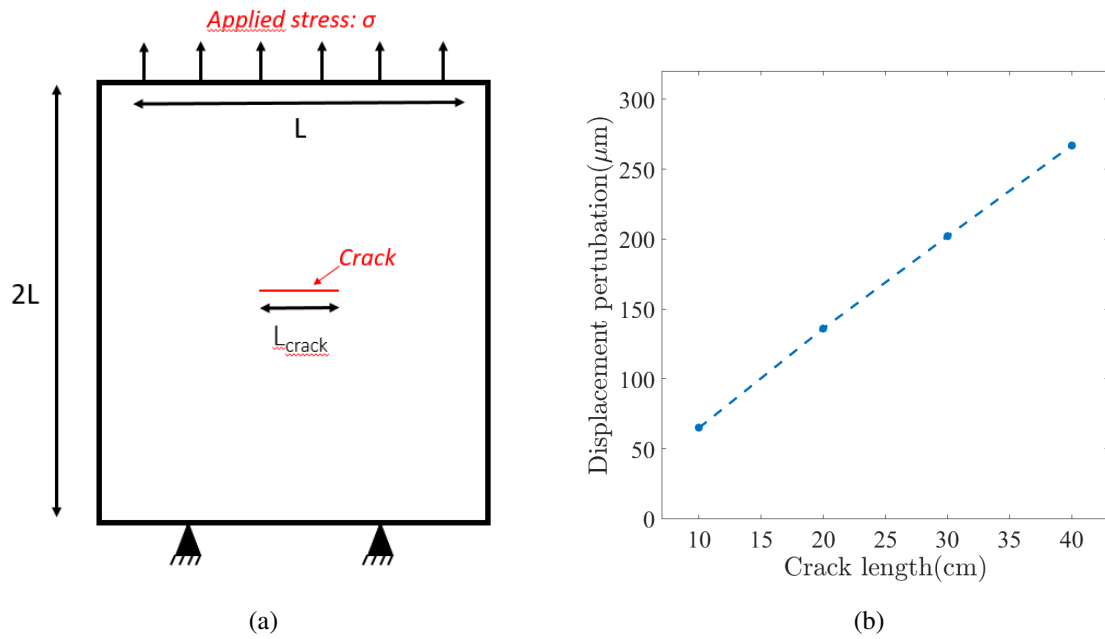


Figure 4.17: Modeling schematic of the displacement perturbation induced by a crack (a) and associated results (b). The displacement jump is recorded at the crack middle, where it is maximum.

4.2.3 Camera

The aim is to be able to simultaneously check between 50 and 100 spots in the wind turbine tower. A mono channel scientific camera can cost between 2000 to 10000 euros. Commercial cameras are about 300 to 1000 euros. This cost prohibits the use of classical devices to make it affordable from an industrial point of view. Thus, a quick state of the art of available cheap cameras on the market was conducted. The first family of devices was commercial webcams. Their price ranges from around 10 euros to several hundred euros approximately. The webcams have most of the time integrated firmwares that directly process images, before being send out to a computer. To get the original image is generally not possible. Thus, the available image is not the raw data but is filtered and degraded. Moreover, the acquisition parameters are automatically determined by the firmware and not the user. Finally, the quality of webcams are not good, they are utilized to take videos and not high quality images. In conclusion, using a webcam is not recommended for DIC purpose. The best solution is to use an easy to handle camera with good quality images. There are nano computers, of the Raspberry Pi brand [Arducam, 2020], to which all kinds of devices, such as cameras, can be connected. The available models use the same sensors as cell phones, as the Sony IMX219. Its price is very appealing: 15 €. The properties of the Pi Camera are summarized in Table 4.4.

This camera has been tested inside a wind turbine tower under operation. It enabled the measurement uncertainty to be evaluated under real conditions. The experimental set-up and the picture taken by the camera are displayed in Figure 4.19.

The experimental conditions are gathered in Table 4.5.

Table 4.4: Pi Camera properties . [Arducam, 2020]

Sensor	IMX219 8 Mega pixels
Definition	1640 × 1232 Bayer pixels
Intensity Levels amplitude	8 bits
Sensor size	3.664 × 2.760 mm
Pixel size	1.12 × 1.12 μm

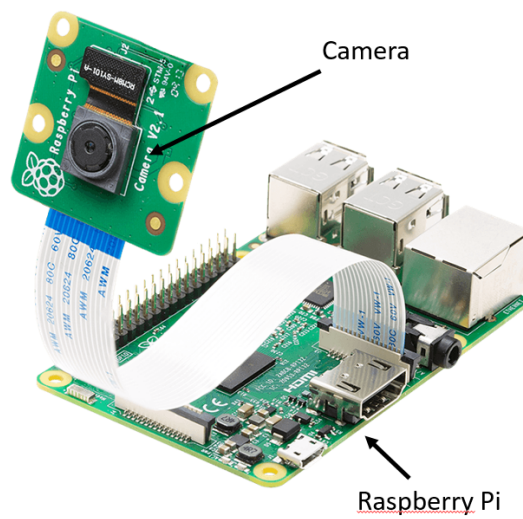


Figure 4.18: Picture of a Raspberry Pi and the associated camera.

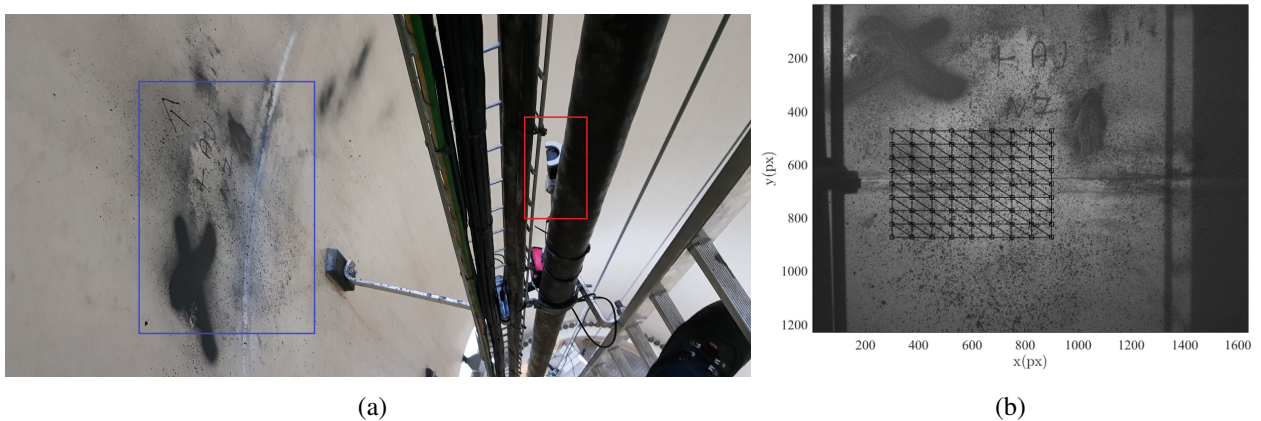


Figure 4.19: Experimental set-up (a). The camera is inside the red rectangle, and the observed zone is in the blue rectangle. Camera field of view with DIC mesh (b).

Table 4.5: DIC hardware parameters.

Camera	Pi camera
Field of view	$45 \times 60 \text{ cm}^2$
Image scale	0.3 mm/pixel
Stand-off distance	55 cm
Image acquisition rate	1 fps
Patterning technique	sprayed paints
Pattern size	6 pixels

The device is an RGB camera. In Section 3.4 the optimal way to process digital color images has been developed. It needs some image processing and very stable conditions for an optimal quality. In this situation, the use of such a process is complicated. It has been shown that using an RGB to gray transformation gives really good results in terms of measurement uncertainty. This particular treatment has been chosen. The experiment results in an uncertainty of $3 \cdot 10^{-2}$ pixel, which is equivalent to 0.02 mm. It is remarkable how small is the absolute value in pixels with regard to the cost of the camera used herein. When comparing to the computation of the damage influence it can be concluded that a 30 cm crack would be detectable under a 25 MPa load. It shows that cheap and sensitive devices are available on the market to achieve the sought goals. However, some other experiments have been conducted with this camera during the this work. It turned out that displacement artifacts appeared when taking pictures over a long period of time. The most likely cause is the appearance of thermal induced strains over time. Considering their envisioned use, it may be proposed that these artifacts are integrated into the displacement modal basis. If this method coupled with this device would be pursued industrially, one should elaborate an integrated DIC approach to remove such artifacts. No more investigation has been carried out about the optimal device.

4.3 Conclusion and perspectives

A new type of damage detection algorithm, based on DIC measurements, has been set up. The conclusions relative to the method are to be found in Section 4.1.7. The accuracy was shown on a simple laboratory case. For further industrial application, a real system should be designed and tested on site. A low price camera was tested and showed encouraging results.

Chapter 5

Damage detection at the macroscale

Summary

In Chapter 4, the development of a damage detection strategy at the mesoscopic scale has shown opportunities to be developed at the industrial level. However, a problem remains because the proposed technique is invasive. This observation motivates the development of a non-invasive damage detection method was also developed at the macroscopic scale. First, state of the art concerning optical measurements for large structures is carried out. Then a strategy to measure tower displacement is explained, based on integrated DIC. Two applications are discussed. First, an innovative modal analysis is proposed. The first two frequencies of the tower are identified. Second, a technique to quantify tower damage is proposed.

5.1 Introduction

Two main subjects are addressed in this chapter, namely, measuring displacements of large structures in an outdoor environment and performing operative modal analysis with DIC. Literature reviews are carried out about these topics.

5.1.1 Measurement of large structures in an outdoor environment

Measuring the displacement or vibrations of large structures is a major subject for their characterization, to optimize the operations and maintenance costs, and avoid catastrophic scenarios [Farrar and Worden, 2007]. Two types of methods exist. First, "intrusive" ones consist in deploying sensors within the structure such as accelerometers [Rytter, 1993], tiltmeters [Yigit et al., 2010] or Global Positioning Systems (GPS) [Moschas and Stiros, 2011]. These methods are accurate but have the disadvantage that the devices are not easy to install and the measurement remains local. In this context, non-intrusive methods are more and more developed in order to overcome these issues, especially optical methods. They are becoming increasingly popular for carrying out measurements, whether in the laboratory or outdoors on large structures. They have the advantage of being non-intrusive and full-field [Baqersad et al., 2017, Camp et al., 2013]. Such methods include lasers and cameras working in the visible range. Robotic total stations (RTS) have been designed. They operate from a transmitting base and a receiving point that is fixed on the studied structure. It enabled to measure displacements of a power transmission line [Moschas and Stiros, 2014], or to characterize the modal parameters of a bridge [Stiros and Psimoulis, 2012]. This type of device is interesting because it is simpler to install than the devices mentioned above, but it is still necessary to place a receiving target at a structure point. A second way to carry out non-intrusive measurements is possible through radar or lidar techniques [Gentile and Bernardini, 2010, Zendehbad et al., 2017]. No target is necessary and the Doppler effect is used [Post and Cupp, 1990]. The relative velocity between the emitting zone and the moving structure is calculated by measuring the frequency shift between the incident and reflected waves. However, the displacement measurement remains local. To overcome this drawback, multiple emission sources pointing at different locations can be used. It allows for a more complete description of the whole structure dynamics. A more powerful technology consists in coherent LIDAR scanning systems [Gueguen et al., 2010, Valla et al., 2015] which enables the modal characteristics of a structure to be extracted. The method is based on two wave beams, namely, a fixed beam that serves as reference and one that scans the structure to capture its deformations over its entire height. This method has shown good correlation with velocimeters [Valla et al., 2015]. Yet, the acquisition noise prevented from measuring high frequency modes. This method is interesting, yet its cost remains high and the system calibration is complex. To overcome the high cost problem, the implementation of methods using standard cameras working in the visible range has been considered. The first publications using photogrammetry go back in the early 1990s. First, it was proposed to place particular targets such as black crosses on structures and to follow them over time using edge tracking methods [Stephen et al., 1993]. The use of multiple targets and multiple cameras enabled for techniques that erased rigid body

motions [Olaszek, 1999]. The use of DIC has also been considered in some works. However, its use remains very limited outdoors. The resolution of DIC is based on the contrast, naturally present or painted, on the studied structure [Hild and Roux, 2012c]. It allowed bridge displacements to be measured under random loadings [Yoneyama and Ueda, 2012, Pan et al., 2016]. A further complication of using DIC outdoors is to ensure the brightness conservation principle. Such variations can induce displacement artifacts [Sciuti et al., 2020]. It has been proposed to overcome the problem of illumination variations by working at night and lighting the structure with a monochromatic source [Pan et al., 2012]. Depending on the size of the studied structure and its location, the use of such method is logistically very complicated. The application of these methods to the measurement of the wind turbine tower displacements is not widespread. A notable work that was done in the course of Ozbek's thesis [Özbek, 2013]. The author proposed an innovative method to measure tower and blades displacements, by using two cameras. Reflective patches were placed on the top of the tower and on the blades. The rigid body motions of these patches were tracked over time. High-speed cameras, located about 200 m away from the wind turbine, were used. The final objective was to perform an operational modal analysis of the structure. The measurement uncertainty for each patch was about 50 mm. The natural frequencies and vibration modes of the structure were estimated from the displacement measurements. Seven modes could be identified from 20 second measurements. The difficulties of this method were the installation of patches, the required camera calibration for stereo-imaging, and finally the acquisition of images that are to be performed at night to exploit patch reflectiveness, since the turbine was illuminated with an LED based flash system. It can be noted that multiple works have been devoted to characterizing wind turbine blades by DIC [Le Blanc et al., 2011, Baqersad et al., 2012], even with drones to carry out health monitoring [Khadka et al., 2019, Khadka et al., 2020]. For all these works, the experiments were performed in laboratory conditions onto painted and scaled prototypes. In Ref. [Poozesh et al., 2014] a real 50 m long painted blade was used to show the benefits of DIC to detect damage, but it was carried out in a laboratory. One notable experiment has been carried out in real conditions with a stereo-correlation system [Winstroth et al., 2014]. Some black patches were put onto the blade tips.

5.1.2 Operative Modal Analysis (OMA)

A modal analysis aims at identifying mechanical parameters that primarily include natural frequencies, damping ratios and mode shapes [Lembrechts, 1988]. One should distinguish the modal analysis with and without proper knowledge of the excitation. The latter case refers to operative modal analysis (OMA) [James et al., 1995, Reynders, 2012]. Outside of laboratories, the ambient condition are difficult, in many cases impossible to control. In the wind turbine industry, such analysis is required because of the loading complexity undergone by the structure, originating from aeroelastic phenomena [Özbek, 2013, Hansen, 2003, Chauhan et al., 2011]. Such an analysis can, for instance, help monitoring the structure health [Farrar and Worden, 2007]. The condition to perform operative analysis is to assume that the excitation sources are broadband random temporally and spatially [Reynders, 2012]. Generally, wind excitation is considered to obey perfectly the OMA assumptions. How-

ever, the aeroelastic phenomena due to rotor rotation can alter the applicability of OMA to wind turbines [Tcherniak et al., 2011]. In the following, the measurement is carried out for a shut down turbine, thus the applicability of OMA is not to be questioned.

5.1.3 Modal analysis with DIC

DIC is increasingly used to perform modal analyses of structures, especially in laboratory conditions. The main limiting factors were the acquisition frequency and data storage [Beberriss et al., 2012]. The development of high-speed and high-resolution cameras opens new possibilities. Two types of methods have been proposed without and with *a priori* knowledge about the structure.

Classical methods

From a set of images and displacement fields calculated by DIC, the modal parameters of a structure can be extracted. There are two types of methods for modal analysis. First the time domain ones which use time response data. In Ref. [Rizo-Patron and Sirohi, 2017] the Ibrahim time domain method was used to perform an operative modal analyses of a scaled rotating helicopter wing based on DIC measurements. These methods are known to be efficient for damping parameters identification, but less accurate for natural frequencies and mode shapes [Hoa et al., 2010]. The second class, frequency methods, consist in passing through the Fourier domain in order to deduce the modal parameters of a structure. The simplest method is to measure the maximum peaks "by hand" to identify natural frequencies [Fu and He, 2001]. More sophisticated methods are needed when multiple points are simultaneously recorded. Most of them are based on the simple principle of trying to match a mathematical model that is supposed to describe the frequency response of an N degrees of freedom structure under random loading to what is actually measured in the frequency domain. The number of sought eigenmodes is a prerequisite for the determination of modal parameters. Such a method has been used to determine the modal parameters of a simple beam [Régal et al., 2017], a membrane [Hu et al., 2019] or a wing [Ha et al., 2015]. They are more widely used and are known to be more accurate for measuring natural frequencies and mode shapes [Hoa et al., 2010].

A priori based methods

With the previously described methods, no a prior information about the structure is necessary to carry out the modal analysis. Hereafter, some examples are given about the interest of having the knowledge about the studied specimen or what is sought. Two works are detailed, and in these cases the main interest is to overcome the problem of low camera frame-rate. It has been a major limitation for the use of DIC for modal analysis applications, even with the constant improvement of camera technologies. In Ref. [Passieux et al., 2018], a spatio-temporal PGD algorithm was proposed to determine the modal characteristics of a beam and a perforated plate. The solution of the PGD problem is spatio-temporal, the displacement field is sought under the form of a sum of multiplications of multiple spatial functions and one temporal function. More precisely, it is a sine function whose unknowns are the phase and frequency. Searching for the displacement field on such a basis reduces the number of unknowns, which leads to smooth the displacement fields and lower the measurement uncertainties.

Such a method enabled the natural frequency and the mode shape to be determined. It has also been shown that these characteristics could be estimated with a lower framerate thanks to adapted formulation. However, by only regularizing temporally it is needed to control the frequency range applied to the structure. If multiple natural frequencies are encountered in the vibration range the determination would become very difficult. In Ref. [Jailin, 2018], the modal analysis of a plate was performed using a single camera and a reflection device useful for capturing out-of-plane deformations. The plate was impacted with a hammer, images were acquired at irregular intervals, about 1 frame per second. From 350 images, a PCA analysis was performed on all measured displacement fields in order to extract the main modes of deformation and vibration. From such a decomposition, the extracted modes are orthonormal with regard to the norm L2. An orthogonalization by the Gramm-Schmidt process, with respect to either the finite element mass or stiffness matrix, is needed to properly compare to finite element vibration modes. The natural frequencies can be calculated thanks to Rayleigh coefficients. The main advantage of this method is to enable for modal analysis of a structure with a simple commercial camera. The acquisition frame rate is no longer a problem. However, it is necessary to have a really good knowledge about the studied structure. In the following, an innovative method to measure displacement fields of a wind turbine tower will be presented. The results of a modal analysis on a shut down turbine will be discussed together with a strategy to carry out a damage detection thanks to a displacement field. More precisely, the sensitivity to damage detection will be questioned, regarding the real damage influence on structure dynamics.

5.2 Wind turbine tower displacement measurement

In this section, the experimental set-up to measure tower displacements and the integrated DIC strategy are presented.

5.2.1 Experimental set-up

Pictures of the wind turbine tower are acquired with a camera positioned 170 m away from the structure (Figure 5.1(a)), along the perpendicular axis to the Rotor Nacelle Assembly (RNA) orientation.

One of the resulting pictures (cropped here to the region of interest) acquired by the camera is displayed in Figure 5.1(b). The hardware parameters of the optical setup are reported in Table 5.1.

Table 5.1: DIC hardware parameters.

Camera	PCO-edge CMOS 5.5
Stand-off distance	180 m
Frame rate	56 fps
Number of pictures	1150
Lens	50 mm
Pixel size	3 cm

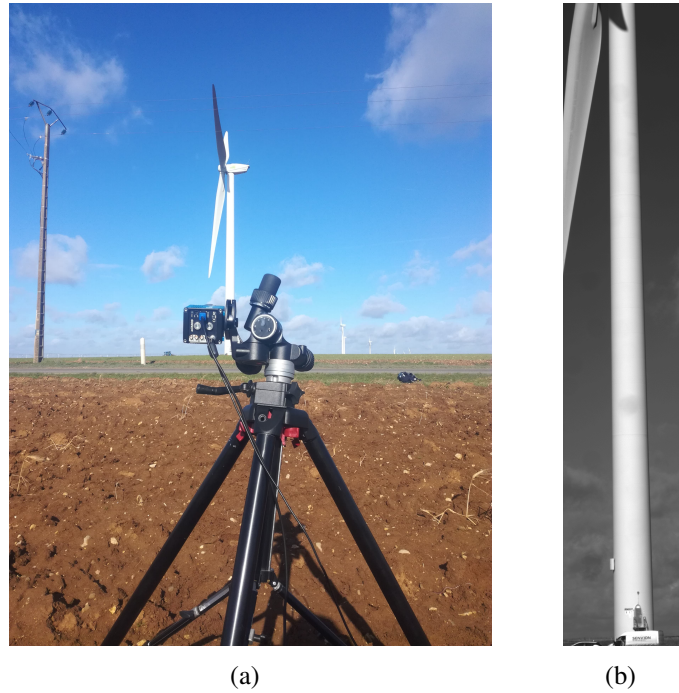


Figure 5.1: (a) Set-up for image acquisition of the wind turbine tower. (b) Picture of the wind turbine tower taken by the camera.

The parameters of the wind turbine are gathered in Table 5.2.

Table 5.2: Turbine parameters.

Height	76 m
Diameter	2.96-4.3 m
Thickness	1.8-2.3 cm
Rated power	3 MW

The gray level and the associated gradient of a horizontal line (1000 pixels from the image top) crossing the image are plotted in Figure 5.2. It is observed that the gradients are maximum at the interface between the sky and the tower. Acquisitions are carried out under in-service condition. The Supervisory Control And Data Acquisition (SCADA) system enables the RNA to always be in the wind direction thanks to data collected from anemometers. A single camera is used to record the scene. The envisioned applications are damage detection and modal analysis. Thus, it is preferable that the dynamics related parameters (like RNA inertia) do not change during an experiment, from the camera field of view. It is therefore proposed, for the sake of robustness, to perform the measurements on a shut down wind turbine with locked rotor, pitch and yaw. Keeping the yaw fixed for a wind turbine in operation is not allowed by park operators. Even if it was possible, issues are likely to arise

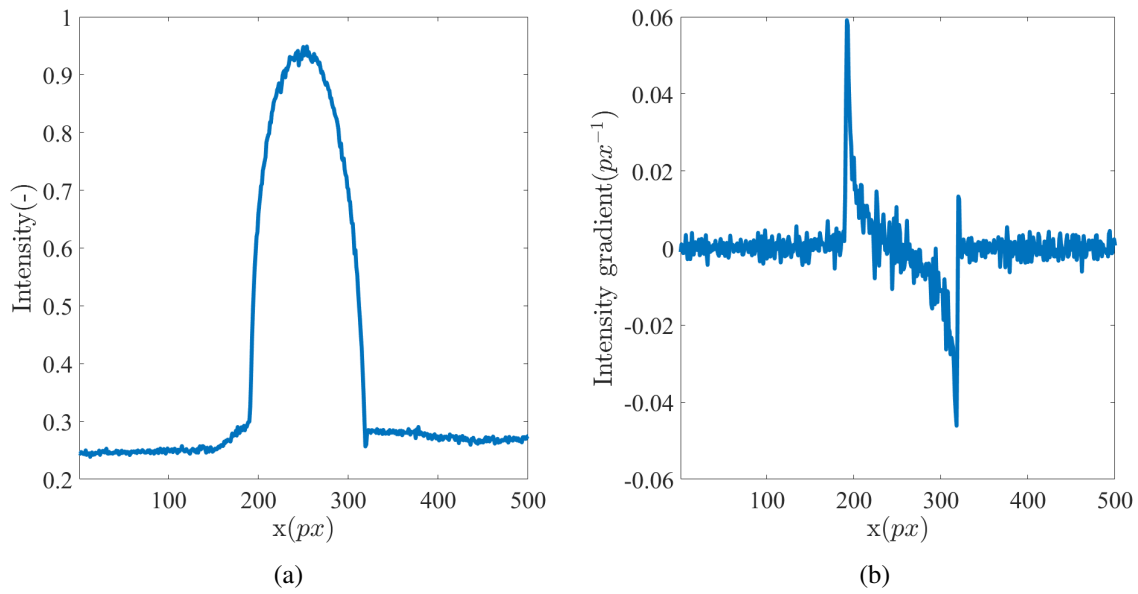


Figure 5.2: Gray level through a horizontal line (a) and corresponding gradient (b).

when using DIC, if the turbine was functioning. The brightness conservation must be ensured at best. Depending on the sun orientation, the blade shadow could appear on the tower and may disqualify the DIC procedure itself, as shown in Figure 5.3.



Figure 5.3: Images acquired with a E70D camera of wind turbines without (a) and with blade shadow (b).

Although brightness and contrast corrections could be considered to mitigate these effects, they would increase the number of unknowns and in turn the uncertainties. From simulations, under normal conditions, *i.e.*, with wind at 10 m/s, the expected vibration amplitude is of the order of few millimeters for a 80 m high tower. The size of one pixel is about 3 cm. The motion amplitude to be captured (about 1 decipixel) is very challenging.

5.2.2 Strategy

The uncertainty of displacement measurement depends on several parameters:

- The quality of the camera, *i.e.*, the “noise” in the acquired images.
- The contrast of the observed surface.
- The “complexity” of the displacement field to be measured (the more numerous the degrees of freedoms, the higher the displacement uncertainty).

Under classical conditions, typically in laboratory, the uncertainty of displacement measured by DIC is of the order of 10^{-2} pixel [Hild and Roux, 2012c]. The structure displays very low contrast and the expected motion amplitudes are less than one pixel. It is not possible to apply paint on the tower, from logistics and environmental reasons. To overcome this drawback it has been chosen to exploit the only accessible information, namely, the boundary between the tower and the sky, where gray level gradients are the highest and well oriented to measure transverse displacements. The selection of pixels for DIC application is illustrated in Figure 5.4.

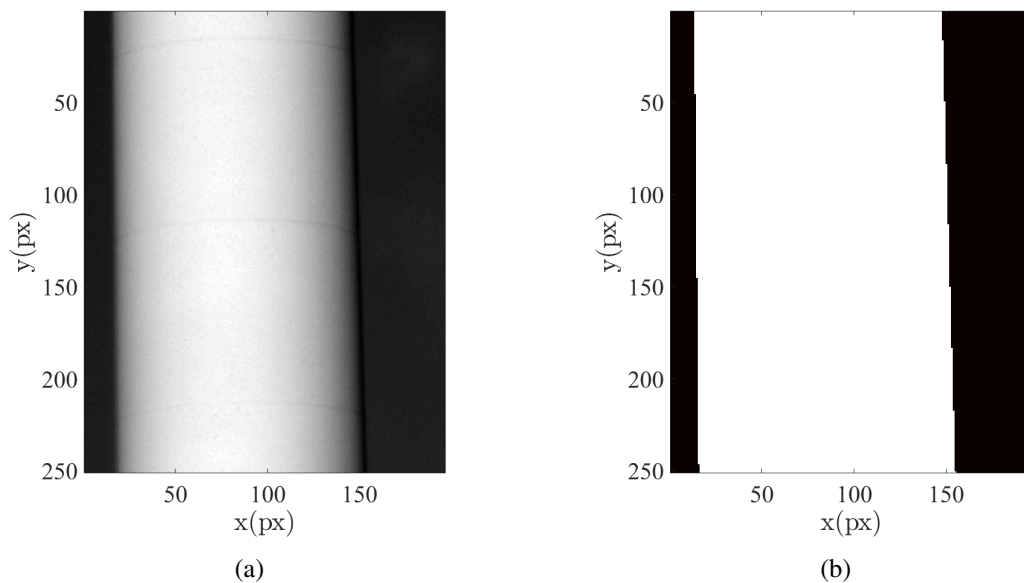


Figure 5.4: Zoom of the turbine (a) and corresponding selection of pixels (of white color) for DIC application (b).

As previously mentioned, the measurement uncertainty is related to the complexity of the displacement field. Generally, hundreds of degrees of freedom are necessary to accurately measure displacement fields during mechanical experiments [Hild and Roux, 2012c]. One possible way to lower the number of degrees of freedom is to integrate *a priori* knowledge about the physical description. It is one feature of global DIC philosophy. It is referred to as *integrated DIC*. It has been used, for instance, to measure stress intensity factors [Roux and Hild, 2006, Rethore et al., 2005, Hamam

et al., 2007] or beam deflection [Hild et al., 2009]. It is interesting to emphasize that for the latter work, the number of degrees of freedom has been drastically reduced to six, sufficient to describe the beam element kinematics. The measurement uncertainty has been evaluated to 10^{-3} pixel, which is one order lower than ordinary values. The integrated approach can also be used to pre-process images in order to erase displacement field artifacts due to optical distortions [Dufour et al., 2014, Charbal et al., 2016a]. The integrated approach philosophy has also been extended to other imaging systems such as high-angular-resolution electron backscattered diffraction (HR-EBSD) to study local elastic strains in crystals [Vermeij and Hoefnagels, 2018, Shi et al., 2019]. For the tower, the general known inputs are the tower geometry and the approximate rotor mass. The measurement is carried out under dynamic loading with no knowledge about it. Thus, it has been chosen to select as displacement basis the vibration modes calculated from a Finite-Element (FE) code. The model of the chosen tower is based on beam elements with variable cross-sections, namely, 100 beam elements are used in the present situation. The RNA is modelled as an added mass with inertia and stiffness. The approximate values of these parameters are obtained with a 3D model from the DIEGO tool [Milano et al., 2019], which is the aeroelastic code for wind turbines developed at EDF R&D. The whole modelling is implemented in *Matlab* [Higham and Higham, 2017]. The first three modes are shown in Figure 5.5.

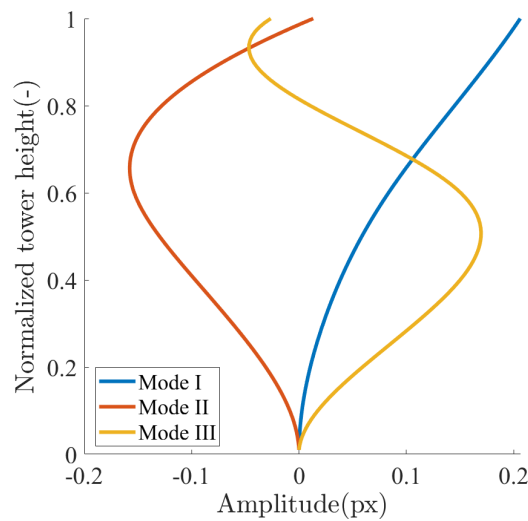


Figure 5.5: Three first modes of the wind turbine tower model calculated with a multiple beam FE code. The y-axis is dimensionless with respect to the tower height.

The DIC analysis parameters are summarised in Table 5.3.

5.2.3 Displacement measurement

In the following, the shape functions amplitudes are expressed with no dimension. They must be related to the vibration mode shapes plotted in Figure 5.5. In the present study, one has the choice to select the appropriate number of vibration modes that will be used as generalized shape functions.

Table 5.3: DIC analysis parameters

DIC software	<i>Matlab</i> code
Image filtering	none
Number of elements	1
Element length	2000 pixels
Shape functions	FE model based (integrated)
Mesh	No mesh
Matching criterion	Quadratic differences
Interpolant	cubic
Displacement noise-floor	see text

It influences the measurement uncertainty associated with each mode amplitude. The measurement takes place outdoors with windy conditions, thus, some rigid body motions must be taken into account. Generally, one considers rigid body translations in both directions and rotation. At the tower base, there is no horizontal motion possible. Likewise, the clamped condition prohibits any rigid rotation, and therefore position and tangent to the deformation of the tower are known at the base. However, when acquiring pictures, it can give rise to additional rigid body motions. The camera's tripod induces that the instantaneous center of rotation is far from the optical axis, and therefore a rigid body translation mode is more relevant than a rigid body rotation mode. With the lack of gray level gradients along the vertical direction, the search for the vertical rigid displacement is compromised. One solution is to pre-correct all images by performing FFT-DIC [Hild et al., 2002] with a ROI restricted to the bottom of the tower. In the following, only the lateral rigid body translation mode is considered. The measurement uncertainties (Section 3.2.3), relative to the shape function amplitudes, are plotted for 1 to 3 selected modes (Figure 5.6).

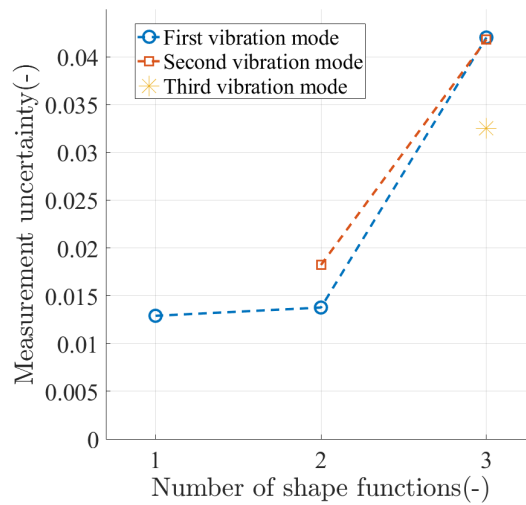


Figure 5.6: Measurement uncertainty associated with each degree of freedom depending on the number of vibration modes.

It is observed that, considering 1, or 2 modes does not affect the uncertainty level. However, integrating the third vibration mode increases the uncertainty by a factor 3 for the first mode and 2 for the second mode. It is of great importance, considering the expected displacement amplitudes. Only one DIC element is considered over the whole ROI. The kinematic basis related to degrees of freedom is minimal and correlations can exist between their contributions. The perfect case would be to consider only two orthogonal shape functions, then no interference would appear. Thus, adding new degrees of freedom over the same ROI increase the likelihood of correlations between the DIC unknowns. The same displacement field can then be reproduced with several shape function combinations. It can be emphasized that taking into account only the first vibration mode leads to a maximum displacement uncertainty of 0.1 mm at the tower top, approximately. In comparison, the method proposed in Ref. [Özbek, 2013] reported a measurement uncertainty of 20 to 50 mm. The developed technique enables very low measurement uncertainty levels to be reached as compared to standard techniques. Four sets of acquisitions have been performed with 1150 pictures acquired for each sequence.

5.3 Wind turbine tower modal analysis

Some of the results presented in this section have already been published [Curt et al., 2020a].

In this section, the results obtained for the modal analysis of the tower are presented. More precisely, two natural frequencies are measured, using instantaneous and spatio-temporal DIC approaches.

5.3.1 First frequency measurement

For the first frequency measurement, an instantaneous DIC approach is used. The first vibration mode and the rigid body translation mode are considered. The frequency calculation is carried out from the FE vibration mode amplitude of the temporal signal. With this method the mode shapes are inputs of the problem, not outputs like other classical methods. This knowledge integration in the calculation is of paramount importance to lower measurement uncertainty. The amplitudes of both degrees of freedoms are plotted as functions of time in Figure 5.7(a) for a single series of pictures. The results obtained with two other series of pictures are shown for comparison purposes in Figure 5.7(b). A significant drift of the camera is seen, thereby confirming the need for including such rigid body translations as relevant degree of freedom. For the first vibration mode, oscillating amplitudes are clearly visible. Depending on the image series, the amplitudes of oscillations differ. With series # 1 the corresponding amplitude is about 15 mm at the tower top, where it is maximum. This change is attributed to the fluctuating wind excitation during the 20 s acquisitions. However, the vibration frequencies look similar. To further investigate this point, the displacement is band-pass filtered in the range 0.15-3 Hz in order to suppress very low and very high frequency components that are irrelevant (reflecting respectively unsteady wind conditions and measurement uncertainties).

For the four series, the power spectra of the vibration mode amplitudes are plotted in Figure 5.8(a). The experiment duration is about 20 seconds. Thus, the frequency step is 0.05 Hz, which is important considering the needed precision. The power spectrum was interpolated using the zeros-padding

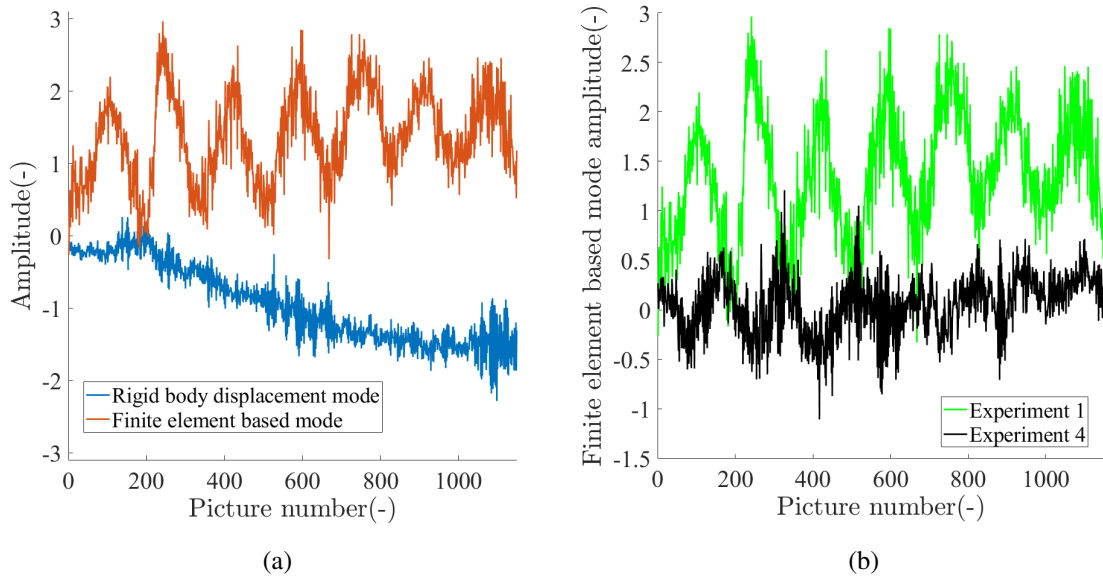


Figure 5.7: (a) Time history of the amplitudes of the two degrees of freedom (translation in blue, and first vibration mode in orange) considered in the DIC analysis for series # 1. (b) Time amplitude of the first vibration mode for series # 1 and # 4 showing similar oscillations although with different amplitudes depending on series.

technique [Zivanovic and Carlosena, 2002]. The peak frequency (at about 0.35 Hz) is in the expected range. Indeed it has not been possible to perform a measurement with accelerometers. The turbine provider estimates the first frequency at 0.4 Hz. Differences between design and real on-site frequencies are common, the cause can be due to foundation particularities.

Figure 5.8(b) shows the four peak frequencies as measured independently for each series. Despite the variable in-service conditions, and the small duration of each series (no more than 7 periods are captured) the standard deviation of the peak frequency is 0.006 Hz, which is remarkably low. Such scatter is greater than what would be expected from an accelerometer (i.e., typically of the order of 0.001 Hz), but this level is regarded as satisfactory given the equipment used herein. It is expected that the scatter would be lowered if acquisitions were performed for a longer duration. Such a tool can thus be used for rapid estimations of a turbine first resonance frequency with very minimal instrumentation.

5.3.2 Second frequency measurement

As mentioned previously, adding the second vibration mode to the kinematic space does not impact the uncertainty associated with the first mode. It has been found that the measured amplitudes are not changed and the resulting frequencies are equal, concerning the first vibration mode. An example of temporal signal, and the power spectra deduced for the four experiments, are plotted in Figure 5.9. The same FFT analyses have been carried out for the temporal signal related to the second vibration mode.

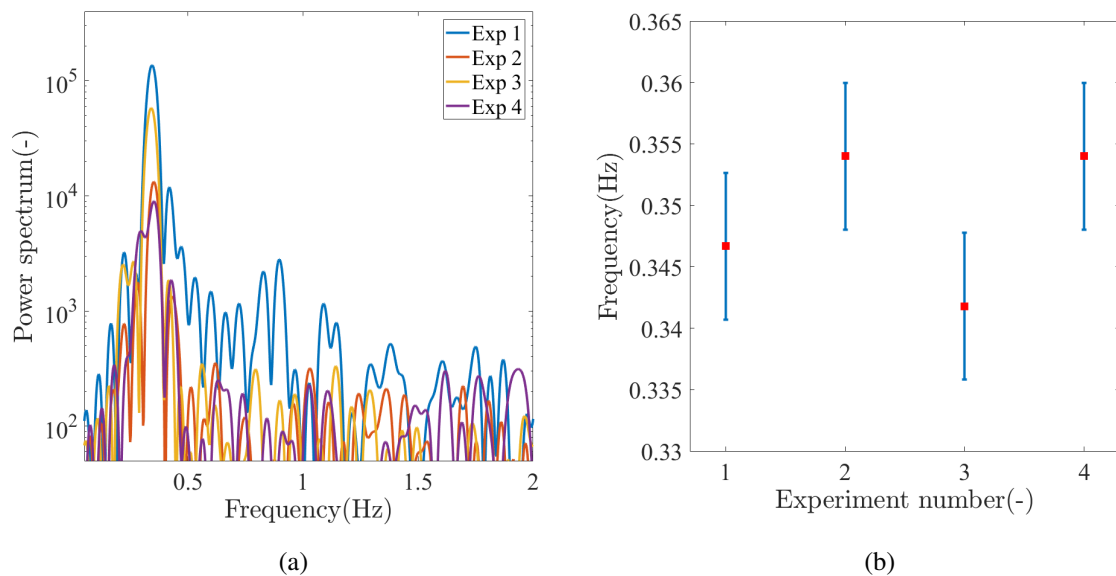


Figure 5.8: Power spectrum (a) and estimated peak frequency values with corresponding error bars (b) for the four pictures sets. The power spectrum is the squared Fast Fourier Transform.

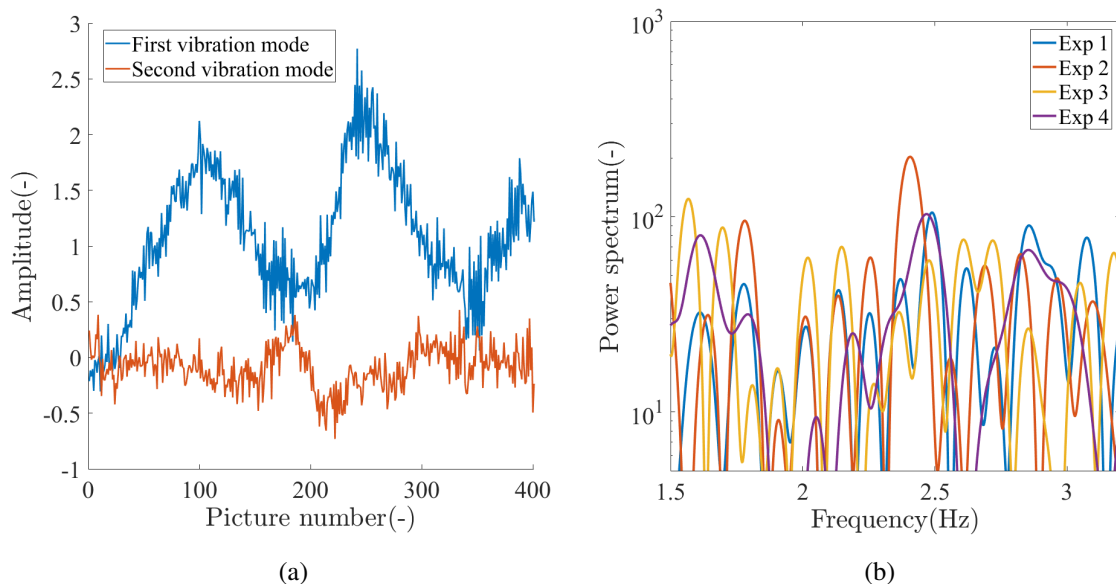


Figure 5.9: Temporal amplitudes obtained for experiment #1 (a) and power spectra obtained for the second mode temporal signal (b).

It is seen that the amplitude related to the second vibration mode is small in comparison to the first one. Moreover, no obvious temporal pattern is distinguished, contrary to the first mode. The expected second natural frequencies should be in the range 2-3 Hz. From the power spectra, the frequencies cannot be determined, likely due to the low temporal contribution of the second mode with respect to the measurement uncertainty. Then, an innovative strategy has been set, relying on the advantage of working in a spatio-temporal framework [Besnard et al., 2011]. As already explained in Section 3.3, the calculation can be performed with or without *a priori* knowledge about the expected temporal histories.

Results with spatio-temporal PGD-DIC

Spatio-temporal PGD-DIC has been introduced in Section 3.3.3. This method has an interest because the framework enables temporal regularization to be added and not choosing the whole set of temporal shape functions. This approach has been tested in order to get a filtered displacement field. Then, it was hoped that the second natural frequency would be easier to determine from the power spectrum. No improvement has been noted for this purpose. However, the spatio-temporal PGD framework, coupled with temporal regularization, has shown again its capability to lower measurement uncertainty [Berny et al., 2018]. In Figure 5.10, the results, with only the first vibration mode, are plotted for several regularization lengths. Five PGD modes were used to fully capture the vibration mode amplitudes.

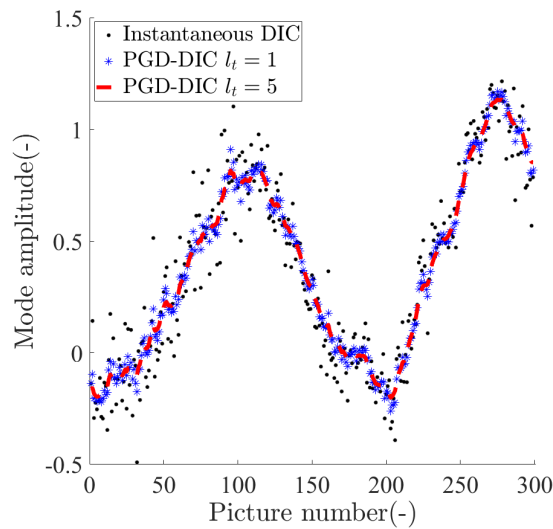


Figure 5.10: Amplitude of the first vibration mode with a PGD approach of experiment #1.

For a temporal regularization duration of 5 images the measurement fluctuation is quasi annihilated. Another strategy has been pursued to get the second frequency.

Results with classical spatio-temporal DIC

The strategy adopted for this part is inspired from Ref. [Passieux et al., 2018], described in Section 5.1.3. The associated theory is presented in Section 3.3.2. It consists in directly exploiting the har-

monical description of the spatio-temporal displacement field. To measure the second frequency, the temporal shape functions are forced to fit this harmonical description, and the allowed spatial description is only reduced to the second vibration mode. The previously calculated displacement field based on a rigid body translation mode and the first FE vibration mode are used as initial displacement field. Thus, one way to proceed is to consider only three temporal shape functions, namely, a sine, a cosine and a mean offset. The associated amplitudes, $[a_s, a_c, a_{off}]$ respectively, are the unknowns of the spatio-temporal DIC problem. The three temporal shape functions are plotted in Figure 5.11. Sev-

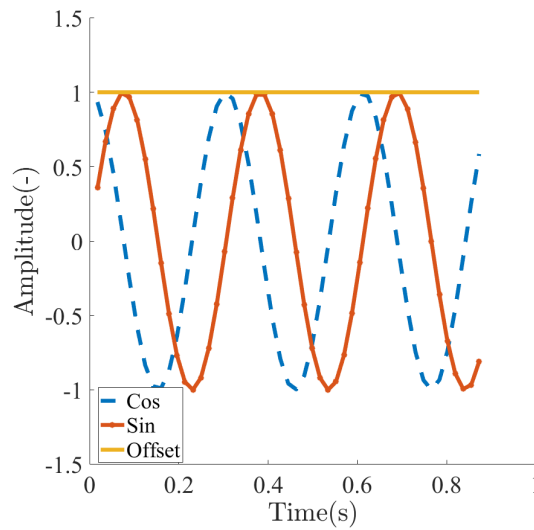


Figure 5.11: Temporal shape functions used for the spatio-temporal approach.

eral frequencies are tested, the selected natural frequency is one that maximizes the temporal norm $\sqrt{a_s^2 + a_c^2}$. Here, a set of 50 images is considered for each experiment. It is assumed, on one hand, that this amount of data is sufficient to get the contribution of the mode. On the other hand, if a larger amount of images is considered, the three temporal shape functions will not be sufficient to account for all temporal fluctuations. The results are plotted in Figure 5.12 for the four experiments. It is observed that determining the natural frequency is easier for experiments #1 and #2 than for experiment #3. No frequency could be measured from experiment #4 with this method, even by increasing the number of images from 50 to 100. The aeroelastic loadings were low during the recording, thus this mode was presumably not excited enough to show any contribution. This remark emphasizes the fact that the ability to measure the second frequency is highly related with the environmental conditions. This approach has also been used to measure the third natural frequency, with no success. The determined frequencies are gathered in Table 5.4. Selecting 50, 75 or 100 images induces less than 0.05 Hz variation for frequency measurements for the three experiments.

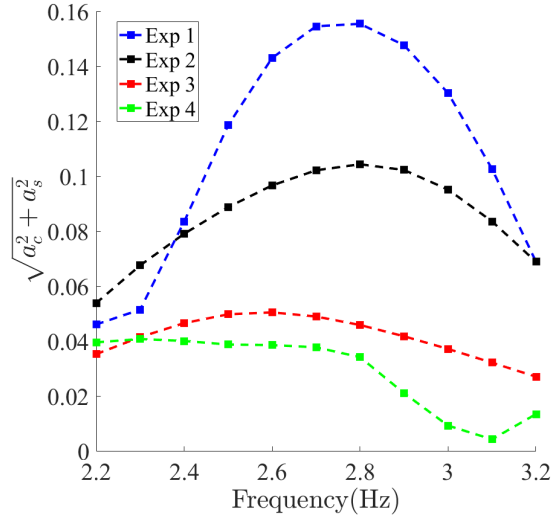


Figure 5.12: Temporal norm for several frequencies of the second vibration modes for all four experiments.

Table 5.4: Results for the measurement of the second natural frequency.

Experiment	1	2	3	4
Frequency (Hz)	2.76	2.80	2.58	-

5.3.3 Influence of the FE model

The considered vibration mode was directly extracted from a simple FE model. Several parameters are not known with high accuracy. In this part, it is proposed to study the influence of the most uncertain parameter, namely, the RNA stiffness. Five values are tested about the initial guess K_0 .

The impact on the first and second mode shape, as shown in Figure 5.13, is visible but modest for large variations of the stiffness. In turn, the resonant frequencies measured with DIC display minor variations (i.e., less than 1 mHz over the entire range of variation for the RNA stiffness). Because the chosen displacement basis has been very limited, even an approximate mode shape is sufficient to capture its contribution in the displacement field over time. These results show that the proposed methodology for measuring the frequencies of the first two vibration modes is *extremely robust*. It can be emphasized that normally, a transformation between the real world frame and the camera should be taken into account. The vibration mode used as input should be modified spatially. It is shown in Appendix C that such optical parallax induced are very small and are not an issue problem for the modal analysis.

5.3.4 Summary

In this work, an innovative optical method, based on integrated DIC has been set to carry out a wind turbine tower modal analysis. From the wind industry point of view, this method is interesting due to its non-intrusiveness. Moreover, the needed hardware to perform such analysis is restricted to a scien-

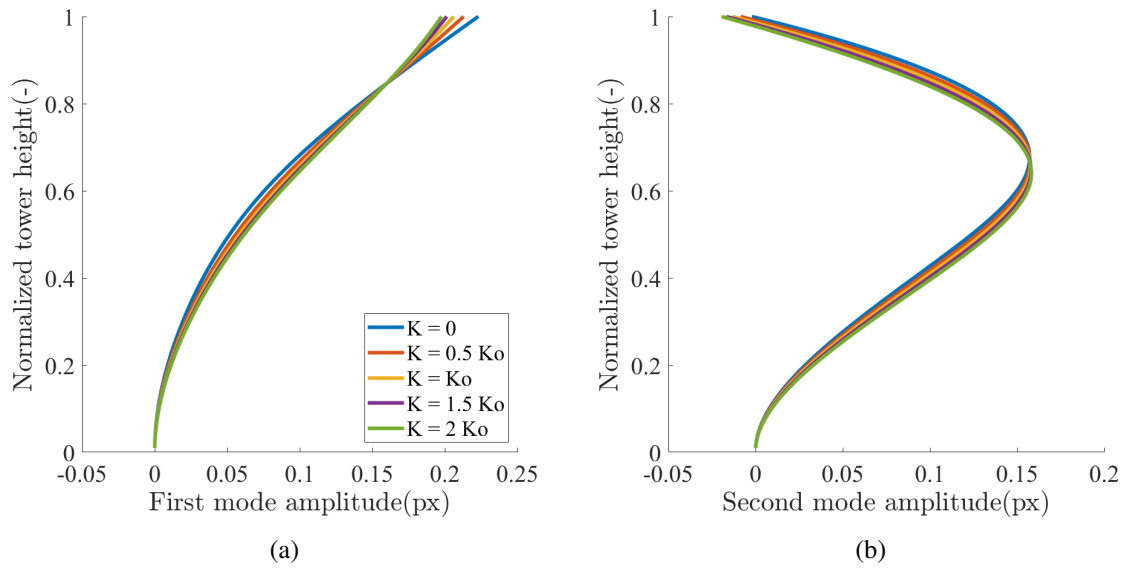


Figure 5.13: Influence of the RNA stiffness on the first (a) and second (b) mode shapes. The y-axis is dimensionless with respect to the tower height.

tific camera. Concerning modal analyses with DIC, new approaches have been introduced. Integrated DIC coupled with an FFT analysis enabled the first resonant frequency to be measured. From 4 sets of images, a very small scatter (i.e., less than 0.01 Hz) was found on the estimate of the fundamental frequency, which is considered very low given the extreme simplicity of the optical set-up. Moreover, no optimisation has been performed about duration of the recording for instance. The second resonance frequency determination has been carried out thanks to a spatio-temporal approach. In addition to integrated DIC for the spatial part, the temporal shape functions fit the harmonical description of the displacement field. The natural frequency is directly sought in the spatio-temporal problem. Reducing drastically the unknowns over a set of images leads to the detection of the contribution of the second mode. This method relies on prior knowledge of geometrical structure characteristics and approximate mechanical parameters such as rotor-nacelle assembly inertia, mass and stiffness. Yet, it was shown that the measurement was very robust to even important parameter changes of the models since only the spatial shape of the fundamental vibration mode matters. The determination of the third natural frequency has been tested, with no success. Under normal conditions, the contribution of high order modes is not sufficient to be captured with this method. As a perspective to this work, it could be interesting to optimize the accuracy of the method. The duration of the recording could be a good parameter to improve the results. In this case, the measured frequencies have not been compared to those obtained with more common systems such as accelerometers. It should be done to completely validate the results, even if they were in the expected range.

5.4 Damage identification

In this section, the theory about damage identification at the macroscopic scale is presented. The results are then discussed and the feasibility of the detection is questioned, based on FE simulations.

5.4.1 DIC based methods to calibrate FE models

The development of DIC, especially in its global setting, has enabled FE models to be compared to measurements. The logical next step was to develop several model calibration strategies. Multiple techniques have emerged in the literature for the solving of inverse problems. For the particular DIC application, the most popular are the Finite Element Model Updating (FEMU) method [Guery et al., 2016, Schmaltz and Willner, 2011], the virtual fields method [Grediac et al., 2006, Toussaint et al., 2006] and the equilibrium gap method [Claire et al., 2004, Claire et al., 2007]. FEMU is based on sensitivity fields determined by FE calculation. The FE model is updated at each iteration by minimizing a functional related to the displacement and loading error. The corrections are calculated based on the sensitivity fields of the displacement field and loading with respect to the calibration parameters. The i^{th} displacement sensitivity field S_i associated with the calibration parameter ζ_i is numerically calculated as follows

$$S_i = \frac{\partial \mathbf{u}}{\partial \zeta_i} \quad (5.1)$$

As an extension to FEMU, integrated methods have been developed [Mathieu et al., 2015]. The novelty lies in the fact that the displacement measurement and the calibration are carried out in a unique step. The new Hessian matrix is a combination between the DIC matrix and the sensitivity matrix. In the present case, this type of calibration is not possible. The aeroelastic loading is not known, which prevents from comparing displacement fields with an FE model. However, the concept of sensitivity field will be used, following a FEMU solving scheme, to try to detect damage. The underlying principle is presented in the sequel.

5.4.2 Damage quantification via DIC

The DIC shape functions are the vibration modes calculated with an FE code, based on beam elements. In Ref. [Hild et al., 2009], a damage law was set up to account for local beam buckling based on integrated DIC measurements. The damage variable was homogenized over a whole beam cross-section, and was represented as a lateral moment of inertia loss. This approach was inspired from lumped damage mechanics [Marante and Flórez-López, 2003, Marante et al., 2012]. For this case study, the same route is followed. Damage is represented by a single variable D , which varies between 0 and 1. When $D = 0$, the cross section is undamaged. When $D = 1$, the cross-section is fully damaged. The damage, homogenized over a beam FE, is thus assumed to be present at a single position along the height. Normally, its location is also a problem unknown. Two routes can be followed to handle this problem. First, several unknowns relative to damage at multiple locations can be considered. It would induce the measurement uncertainty to be increased, due to sensitivity fields

correlations. The second route consists in performing the same computation for several pre-assumed damage locations. In the following, the unknown relative to damage will be kept to a single variable. To take this damage into account, the shape functions are no longer suitable to describe the tower displacements. The modes ψ_i^D are now relative to damage. The previous modes ψ_i are in this new framework equal to ψ_i^0 . By linearization, the ψ_i^D modes are decomposed as

$$\psi_i^D \approx \psi_i^0 + D \frac{\partial \psi_i^0}{\partial D} = \psi_i^0 + D \phi_i \quad (5.2)$$

with ϕ_i the i -th sensitivity field relative to damage. The sensitivity field related to the first vibration mode is plotted in Figure 5.14. The abrupt change in the slope of the sensitivity field indicates the position of the damaged element.

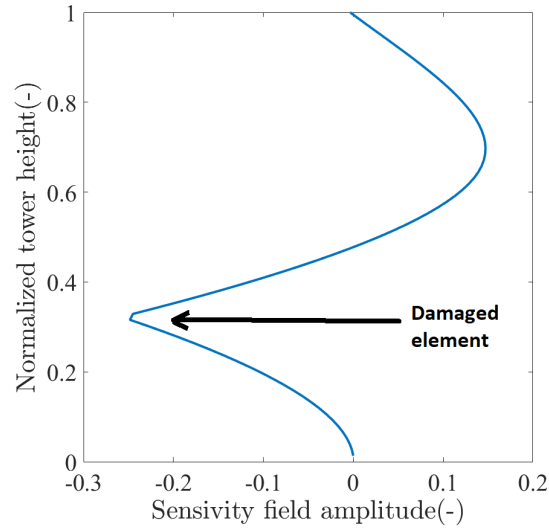


Figure 5.14: Sensitivity field relative to damage for the first vibration mode (a). It is calculated by considering a damage level $D = 0.01$ at 25 m height (0.31% of the total tower height).

Then, the sought displacement field is written as

$$u(\mathbf{x}) = \sum_{i=1}^{N_{dof}} \alpha_i \psi_i^D(\mathbf{x}) = \sum_{i=1}^{N_{dof}} \alpha_i (\psi_i^0(\mathbf{x}) + D \phi_i(\mathbf{x})) \quad (5.3)$$

where N_{dof} is the number of degrees of freedom. To the unknown amplitudes α_i is added only the unknown damage level D to solve this problem, which is non-linear. Two steps are then necessary to solve it. First, the convergence about the coefficients α_i is sought, without taking into account damage. The considered modes are ψ_i^0 . Then, the vibration mode sensitivity fields to D are set up, and their amplitudes are sought. The minimisation can be iterative between those two steps, or direct. It depends on the D level. If it is small, it is expected that the damage influence on the kinematics will be small. Then, a unique evaluation of D is sufficient. The matrix, here a scalar, relative to the

damage sensitivity is written as

$$M_D = \sum_{k=1}^{N_x} \left(\sum_{i=1}^{N_{dof}} \alpha_i \phi_i(\mathbf{x}_k) \cdot \nabla f(\mathbf{x}_k) \right)^2 \quad (5.4)$$

where N_x is the number of pixels. The right hand side reads

$$b_D = \sum_{k=1}^{N_x} \left(\sum_{i=1}^{N_{dof}} \alpha_i \phi_i(\mathbf{x}_k) \cdot \nabla f(\mathbf{x}_k) \right) (f(\mathbf{x}_k) - \tilde{g}(\mathbf{x}_k)) \quad (5.5)$$

where $\tilde{g}(\mathbf{x})$ represents the updated image with the displacement field $\mathbf{u}(\mathbf{x}) = \sum_i \alpha_i \psi_i^0(\mathbf{x})$.

Thus the damage variable is calculated as follows

$$D = M_D^{-1} b_D \quad (5.6)$$

Lowering measurement uncertainties can be achieved by considering more information, thus multiple images. They are indexed by the variable t . The sensitivity matrix relative to damage is now written

$$M_D = \sum_{t=1}^{N_t} \sum_{k=1}^{N_x} \left(\sum_{i=1}^{N_{dof}} \alpha_i(t) \phi_i(\mathbf{x}_k) \cdot \nabla f(\mathbf{x}_k) \right)^2 \quad (5.7)$$

and the right hand side reads

$$b_D = \sum_{t=1}^{N_t} \sum_{k=1}^{N_x} \left(\sum_{i=1}^{N_{dof}} \alpha_i(t) \phi_i(\mathbf{x}_k) \cdot \nabla f(\mathbf{x}_k) \right) (f(\mathbf{x}_k) - \tilde{g}(\mathbf{x}_k, t)) \quad (5.8)$$

where $\tilde{g}(\mathbf{x}, t)$ represents the updated image with the displacement field $\mathbf{u}(\mathbf{x}, t) = \sum_i \alpha_i(t) \psi_i^0(\mathbf{x})$.

5.4.3 Sensitivity to damage detection

The concept of measurement uncertainty has been developed in Section 3.2.3. Here, the measurement uncertainty variance Var_D is

$$Var_D = 2\sigma_\eta^2 M_D^{-1} \quad (5.9)$$

where σ_η is the noise level, deduced after a DIC calculation. A factor 2 is taken into account for the noise covariance matrix because the reference image is noisy.

The sensitivity to damage detection is a key element to conclude about the method feasibility. In Chapter 2, damage was assimilated to cracking. Thus, a parallel must be drawn between damage at the beam element level, and damage assimilated to a crack. It is conducted by evaluating the impact on kinematics with both modellings. The tower is fully modelled with 3D FEs with *Code_Aster* and

the crack is inserted into the mesh with *Zcracks* (see Figure 5.15).

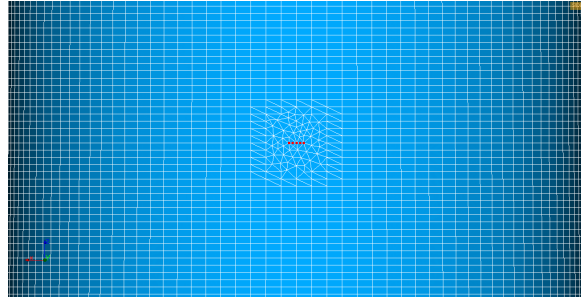


Figure 5.15: Zoom of the 3D FE mesh of the tower with a crack.

The chosen comparison case is done by simulating in statics a horizontal load at the tower top of 1 MN (*i.e.*, the induced displacement is about 30 cm) with both models. For the 3D FE model, the crack is located on the tensile side. Then, the relative displacement differences at the tower top between a healthy and a damaged structure are compared. It enables a parallel to be drawn between crack length and a corresponding beam element damage. Damage is located at 25 m height, and 1 meter long beam elements are considered. The results are presented in Figure 5.16.

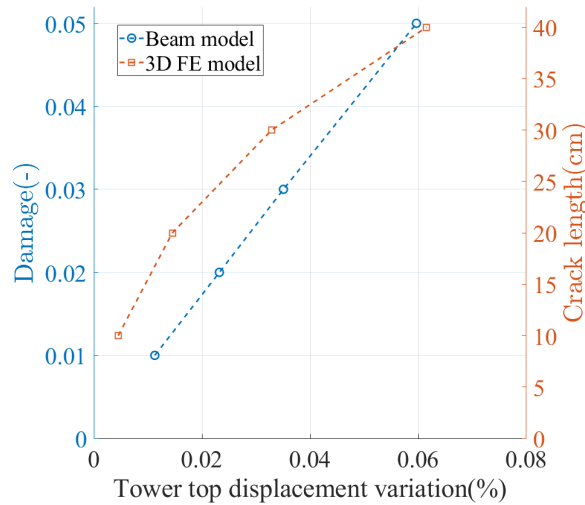


Figure 5.16: Comparison between 3D FE model and a beam model about kinematic impact of damage. The graph has two ordinates: the homogenised damage variable for the beam model and the crack length for the 3D model.

In Section 2.4, it has been concluded that a 30 cm crack could drastically lower the resistance of a wind turbine tower in case of storm, for instance. From the graph, it is seen that the corresponding beam element damage to a 30 cm long crack ranges between 0.025 and 0.03 (0.03 will be kept). The normalized displacement variation is nearly 0.02 %, which is very small. The corresponding beam element damage for a 40 cm long crack is about 0.05. These two values are taken as references. The

measurement uncertainties are plotted for the four experiments in Figure 5.17. Only the amplitudes relative to the first vibration mode are used to set up the sensitivity matrix M_D .

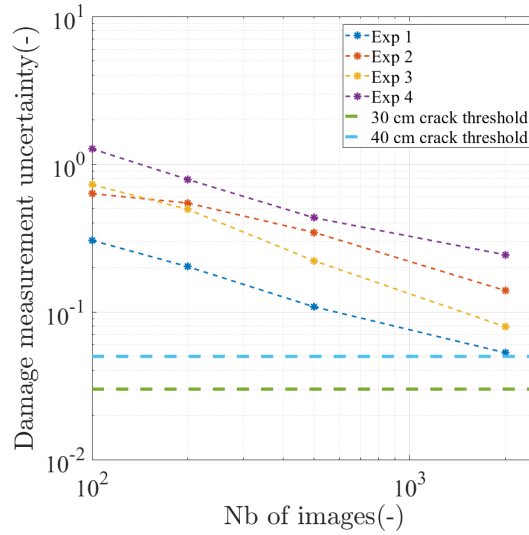


Figure 5.17: Measurement uncertainty relative to damage variable.

First, it is seen that even with considering 2000 images, the targeted measurement uncertainty is reached only with one experiment out of four. A factor 5 appears between the experiments in terms of damage determination uncertainty. It comes from the displacement amplitude ranges that differ between the experiments. The damage sensitivity field is calculated based on a damage level $D = 0.01$. This explains the unphysical uncertainty values, greater than 1, when less than 100 images are taken for the calculation. It shows the difficulty to spot damage from the tower kinematics. Even with drastically lowering the measurement uncertainty by adopting an integrated approach, it is still a priori not possible. Moreover one problem must be pointed out, that penalizes the use of the method in an industrial context. Here, it is assumed that damage can be seen from the camera field of view. However, the accuracy of the method also depends on the RNA direction. Damage can be invisible at the recording time if the RNA is not oriented along the damage orientation. The wind direction, coupled with the weather conditions are difficult to predict.

5.5 Conclusion and perspectives

In this chapter, an innovative way for measuring tower displacements has been set. Several challenges have been tackled, like working in an outdoor environment, and the lack of contrast of the structure. An integrated approach has been used, based on FE vibration modes so that enables very low measurement uncertainty levels can be reached (i.e., less than one millimeter). From this framework two applications have been carried out. First, the tower modal analysis, exploiting the integrated DIC. The first natural frequency has been measured easily with instantaneous DIC and frequency analysis of the associated temporal amplitude. The spatio-temporal framework has been used to extract the second natural frequency. Such a tool can help engineers to quickly determine natural frequencies of wind

turbine towers. As a perspective, this method should be optimized by customizing the recording time and the frame rate. The second application is about damage detection at the macroscopic scale. Damage is considered as a lateral stiffness loss, according to lumped damage mechanics theory. However, it has been shown based on finite element simulations, that the sensitivity of the method to damage detection is too small, regarding a damage influence on the kinematics. As a perspective, it could be interesting to test the algorithm onto damaged towers or export this methodology to other structures. The capacity of the optical methods and more particularly, DIC, is very attractive. Whatever accurate and solid is the background theory, working in an outdoor environment can be very complicated. The sites accessibility and the weather conditions are not controllable. Thus, to foresee interventions is very difficult. An other thing must be pointed out, the modelling of the tower with beam elements is carried out with assumptions about the RNA characteristics, modelled as an added mass. Its stiffness and inertia are approximated. One other uncertain parameter is the steel Young's modulus. One could expect that welds and bolts make the tower apparently more stiff. It was envisioned to perform model calibration, with the same strategy as the one for damage detection. But, at the end the same conclusion was drawn, namely, the sensitivity was too small to be able to calibrate the tower model properly.

Chapter 6

Conclusion and Perspectives

This PhD work took place in the context of maintenance optimization of onshore wind turbines. It was more particularly focused on the most critical element, namely, the tower. Two major topics related to this theme were addressed in this PhD work. First, structural aspects related to the assessment of the residual life of a damaged wind turbine tower were discussed. Then, methods of damage detection by DIC were proposed at the mesoscopic and macroscopic scales. The main highlights of each chapter are summarised in the following

- **Chapter 1:** It is assumed that the tower lifetime is driven by fatigue due to repetitive aeroelastic loadings. The expected tower lifetime is calculated thanks to a Miner damage rule. The undergone stresses, over the whole operation lifetime, are calculated with aeroelastic codes, and are dependent on meteorological predictions. It is influenced by uncertain parameters related to the environment and materials. Thus, safety factors are included in these predictions. However, around the world, a few wind turbines have already collapsed, each time during extreme climatic events. Academic and industrial sources have also reported the discovery of cracks on some turbines at the weld-material interfaces. To prevent catastrophic events, structural health monitoring techniques have been developed. They are generally carried out using sensors extrapolating a global state of health from local data (accelerometers, strain gauges). The risk is that a defect remains invisible yet critical for the structure.
- **Chapter 2:** The two identified tower failure causes are the local buckling of the tower and the tearing off of its upper part. A study was carried out to determine the impact of the presence of a crack regarding the structure strength to both failure mechanisms. FE simulations showed that the tower buckling was weakly impacted for cracks up to 40 cm in length. The critical load is lowered by about 10 %, at the most. Experiments and simulations carried out in the literature with similar aspect ratio cylinders as wind turbines corroborate these results. The critical load corresponding to a 30 cm long crack is about three times less than the buckling load. A test case of rotor misalignment with respect to the wind direction in a storm was simulated. The loads required to tear off the upper part of a tower, damaged by a 30 cm long crack, were reached at

a misalignment of 20 degrees and a wind velocity of 60 m/s. The simultaneous combination of different factors such as high wind, bad control of nacelle orientation and the presence of a crack, leads to the most critical situation. Such wind conditions have already been reported in France.

- **Chapter 3:** The principles for instantaneous and spatio-temporal DIC, which were used in Chapters 4 and 5 were presented. One motivation during this PhD work was to lower measurement uncertainties, to be able to detect damage as early as possible. Therefore, a mathematical framework of the *optimal* DIC with N channels has been proposed and validated with color images. A specific image process has been set up. First, the Poissonian noise of each field is normalized thanks to an Anscombe transformation. Then, the eigen-colors relative to noise are determined. The color channels are transformed to the frame of eigen-colors so as to give them an appropriate weight to perform the DIC calculation. For a standard color camera, the measurement uncertainties varied by a factor of 2 depending on the chosen transformation and minimised functional, with respect to the optimal framework.
- **Chapter 4:** An innovative algorithm was set up for damage detection at the mesoscale, with DIC. The idea is to establish for each camera, when the structure is considered sound, a displacement modal basis using model reduction techniques. Over time, if an underlying or through defect appears, it will induce a disturbance in the displacement field which can be detected using global indicators such as displacement deviation or DIC residuals. Moreover the concept of *extractors* was introduced, to perform "one-step" DIC, based on a suited image filtering designed to ensure robustness. The envisioned industrial system was patented. It is based on a low-cost camera device, inside the wind turbine, covering circumferential welds in the regions of highest stress.
- **Chapter 5:** An integrated DIC framework was set up to measure tower displacements in its entirety. The camera was located 200 m away from the turbine. The lack of structure contrast motivated this choice, aiming to reduce the number of unknowns in the DIC problem and to lower the measurement uncertainties. FE vibration modes were used as degrees of freedom. Such a measurement is performed under dynamic loadings, even if the turbine is shutdown. Two specific applications were conducted. The first one was the tower modal analysis, using a scientific camera. The first natural frequency could be measured directly from the temporal signal thanks to the integrated DIC framework. The second natural frequency was measured by using a specific spatio-temporal approach. This method is very innovative due to its non-intrusiveness and low cost. The second intend application was damage detection. However, the measurement uncertainty compared to the modeled kinematic impact of damage led us to conclude that this application was out of reach.

A lot of work remains in the field after this PhD work. In the following, some research topics that

would deserve to be further investigated is given (and is not meant to be exhaustive). First, concerning DIC developments:

- The optimal N channels DIC framework was validated with color images. The process could be applied to hyperspectral images. The reduction of measurement uncertainty could also be achieved for experiments that use "images" from different devices, like visible and infrared cameras [Charbal, 2017, Wang, 2019].
- Damage detection at the mesoscale was shown on a simple laboratory case. For further industrial application, a real system should be designed and tested on site. In this work, a low price camera was tested and showed encouraging results.
- The tower displacement measurement carried out within an integrated framework based on FE vibration modes is innovative. In the end, the damage detection was not possible but the approach could inspire damage detection for other structures. The proposed framework does not require any knowledge of the external load. This method could be tried with more accessible structures, in laboratories or outdoors.
- The modal analysis should be customized by recording again with variable acquisition frequency and time ranges. This method could be extended to measure other structures natural frequencies.

Then, about operations and maintenance of wind turbine towers:

- As previously explained, cracks have been spotted at the material-weld interface. It is certainly due to high residuals stresses from the welding process. Some variability about the mechanical properties of the welds can be expected. It could be interesting to carry out exhaustive tests to characterise those made under real site conditions.
- Crack fatigue propagation could be simulated by accounting for residual stresses.
- In this work, the simulated extreme event was simulated with a RNA misalignment coupled to high winds. It could be interesting to make statistics about these events in order to take them into account in fatigue life calculation. Or, to evaluate the possible crack propagation due to such repetitive but unexpected events.
- Very few publications are devoted to forensic analysis of collapsed wind turbines. In the future, turbine collapses should be investigated and more thoroughly documented to help understanding the true failure causes.
- In this work, visible cameras were used to measure displacement and natural frequencies of a wind turbine tower. Performing DIC outdoor can be difficult due to illumination variations. The scanning Radar or Lidar are, maybe, interesting solutions for the future if their costs would drop.

Appendix A

Description of aeroelastic simulations

At EDF R&D, the aeroelastic loading computation are performed by an in-house full aero-hydro-servo-elastic solver, DIEGO [Milano et al., 2019]. The calculation is split into two parts: the determination of the aerodynamic effort and the turbine structural response. For the first part, blades are discretized in sections along their wing section chord. With respect to the wind vector, one knows the angle of attack for each section. Pitch and twist of each section are taken into account as the angles between the chord of the section and the plan of the rotor disk. Once the angle is known, the lift and drag forces are evaluated by considering the airfoil polar curves of each section of each blade. For the considered wind turbine, the polar curves are plotted in Figure A.1.

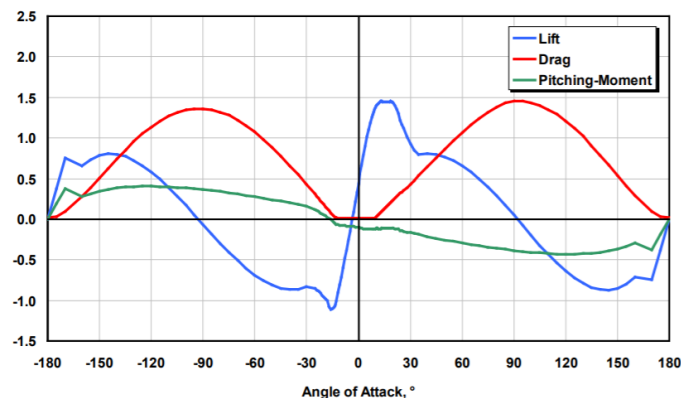


Figure A.1: Corrected coefficients of the NACA64 airfoil [Jonkman et al., 2009].

Those forces are integrated and projected on the rotor disk, giving the thrust force and a lateral force on the tower. These aerodynamic forces are calculated with the Blade Element Momentum Theory (BEMT) [Glauert, 1935]. The flow is considered steady, which means no turbulence is considered. This theory does not account for wake expansion and tip losses. It also assumes that each section is independent from another, but correction factors can be used. On the other hand, the tower and the blades are modelled with beam elements. Then, the fluid-structure interaction is ensured at each time step by projecting the aerodynamic loads on a structural model at the scale of the entire wind turbine. The structural response of the whole structure is also considered for the aerodynamic

loading. The whole system is solved thanks to a Newmark time integration scheme. It must be noted that the RNA mass is taken into account at the tower top. This element has a significant influence on the turbine dynamics due to the high mass concentration and tower top accelerations. A rendering of the NREL 5MW wind turbine model in DIEGO is shown in Figure A.2.

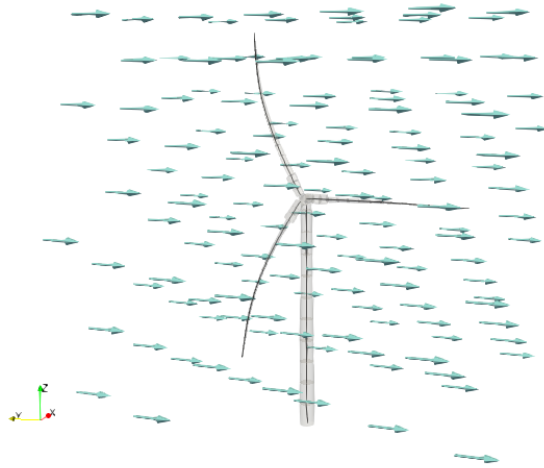


Figure A.2: NREL 5MW model rendering in DIEGO. The arrows represent the wind velocity at multiple points.

Appendix B

One step DIC with large displacements

In the previously presented work, the encountered displacement amplitudes were less than 1 px. Thus a simple homogeneous filtering was sufficient. In this appendix, the problem of using “one-step” DIC is addressed with larger displacements. More particularly, an optimal inhomogeneous image filtering is proposed to better estimate displacement fields. It is assumed that the local filtering length λ is linked with the local displacement statistics. It can be the maximum, or the average weighted by a multiple of its standard deviation. In this case, it is linked with the maximum recorded displacement, $\xi(\mathbf{x})$. The theory about this particular filtering is first described. Then, an artificial application case is set to illustrate the method interest.

B.1 Inhomogeneous filtering

This section describes inhomogeneous filtering of an image. From a $\lambda(\mathbf{x})$ filter length field defined at each point of the ROI, N filter lengths $\hat{\lambda}_i, i = 1, \dots, N$, are chosen to cover the range of λ values. The distribution of the lengths can be made equally between the two extreme values, or follow a power law for instance.

For each of these lengths $\hat{\lambda}_i$, a homogeneous filtering of the image $f(\mathbf{x})$ denoted $\tilde{f}_i(\mathbf{x})$ is carried out by convolution with a Gaussian of standard deviation $\hat{\lambda}_i$. These different filtering lengths will be used to create N homogeneously filtered images. It is proposed to approach image filtering at any scale λ by linear combination of images $\hat{f}_i(\mathbf{x})$ and $\hat{f}_{i+1}(\mathbf{x})$

$$\hat{f}_\lambda(\mathbf{x}) \approx \alpha \hat{f}_i(\mathbf{x}) + (1 - \alpha) \hat{f}_{i+1}(\mathbf{x}) \quad (\text{B.1})$$

where α is a weighting coefficient to be determined. The minimization of the quadratic difference between the two members of this equation, on a small scale, provides the curvatures at the origin of the two convolution operators, Gaussian of standard deviation λ on the one hand, and weighted sum of the two filters of lengths $\hat{\lambda}_i$ and $\hat{\lambda}_{i+1}$. This leads to the weighting coefficient

$$\alpha = \frac{\hat{\lambda}_{i+1}^2 - \lambda^2}{\hat{\lambda}_{i+1}^2 - \hat{\lambda}_i^2} \quad (\text{B.2})$$

The advantage of this approximation is that it is performed in the real space. For each pixel position, it is easy to identify the weights $\alpha_i(\mathbf{x})$ to be assigned to the N filtered images, and to calculate the inhomogeneously filtered image by mere linear combination.

B.2 Calibration of the filter

In this part, the appropriate filtering coefficients are set depending on the locally encountered displacement. To achieve such goal, it is chosen to select the best homogeneous filtering length that minimizes displacement errors with artificial rigid body translations. Then, the function that associates the filtering length to the displacement amplitude is set. The same specimen and ROI as previously considered were selected. The results are plotted in Figure B.1. First, it is observed that for translation amplitudes less than 1 px, the filtering length is independent of the translation amplitude. Above 1 px, the ratio between the optimal filtering length and the translation amplitude is about 4. No explanation is proposed to explain this sudden gap.

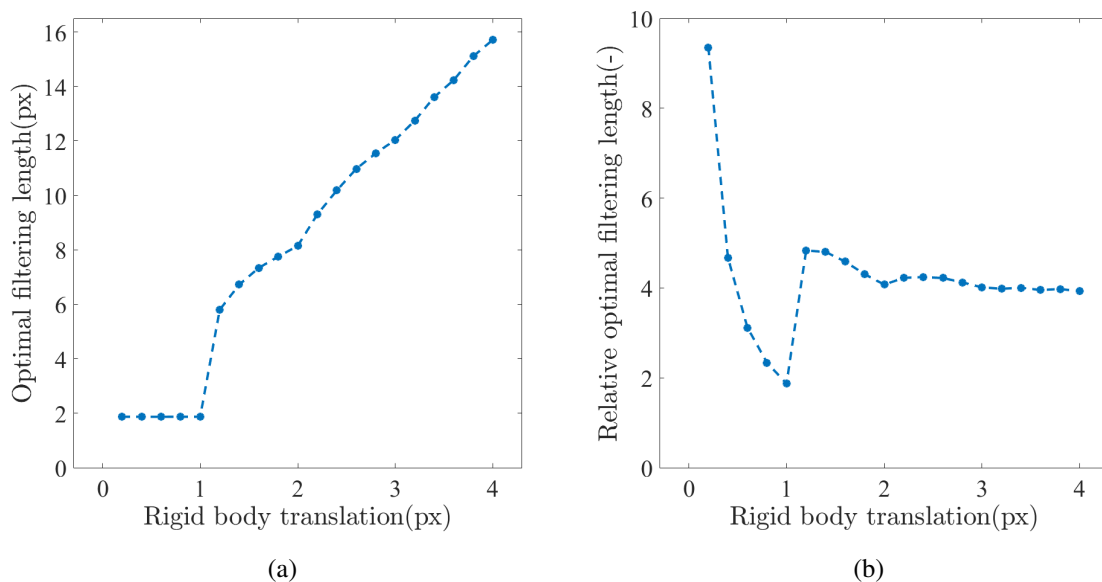


Figure B.1: Absolute (a) and relative (b) optimal filtering lengths.

B.3 Application to heterogeneous displacement fields

In this subsection, the interest of inhomogeneous filtering is shown when large displacement amplitudes (*i.e.*, greater than 1 px) are encountered. Displacement fields related to tensile tests were tested:

- One relative to uniform strain over the whole ROI. It will be referred to as Case 1 in the following.
- One related to the first displacement mode found in Section 4.1.2. It will be referred to as Case 2.

The performance of the filtering strategy is tested for maximum amplitudes ranging from 0.4 to 4 px, by steps of 0.4 px. The displacement map used as reference for filtering is based on a maximum amplitude of 4 px. The inhomogeneous filtering is carried out based on the results observed in Section B.2. Depending on the local maximum amplitude, different filtering lengths are selected. For pixels where the maximum encountered displacement is less than one pixel, the filtering length is equal to 1.9 px. For pixels where the maximum amplitude is greater than 1 px, the filtering length is equal to 4 times the amplitude. As explained above, an approximation based on few homogeneously filtered images is performed. Four filtering lengths are chosen, namely, 1.9, 4, 8, 12 and 16 px. This choice is arbitrary.

The reference displacement map and the corresponding filtered image are displayed for case 1 in Figure B.2. The effect of inhomogeneous filtering is visible between the right part (*i.e.*, small displacement amplitudes) and the left part (*i.e.*, higher displacement levels).

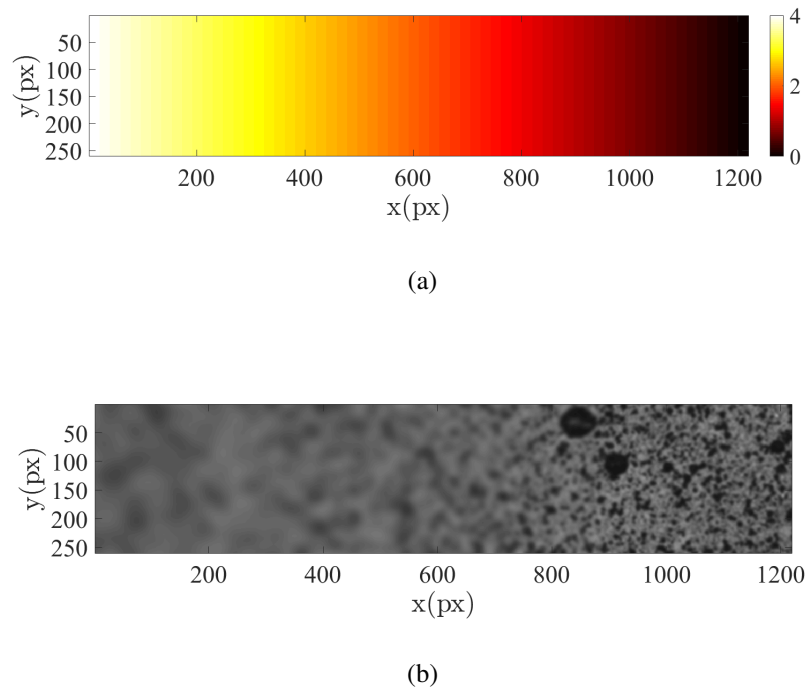


Figure B.2: (a) Displacement map along x -direction in pixels. (b) Corresponding adaptively filtered image.

There are two ways to evaluate the approach performance. First, one can look at the one-step DIC error over the whole range of displacement amplitudes. The RMS of the error vector is thus a good indicator. Second, the prediction error is studied for the largest magnitude. The comparison between homogeneous and inhomogeneous filterings for both indicators are plotted in Figures B.3 and B.4 for cases 1 and 2.

The results are better with inhomogeneous filtering for both indicators and both cases, for any filter length. This innovative way of filtering is more adapted. This new technique yields lower dis-

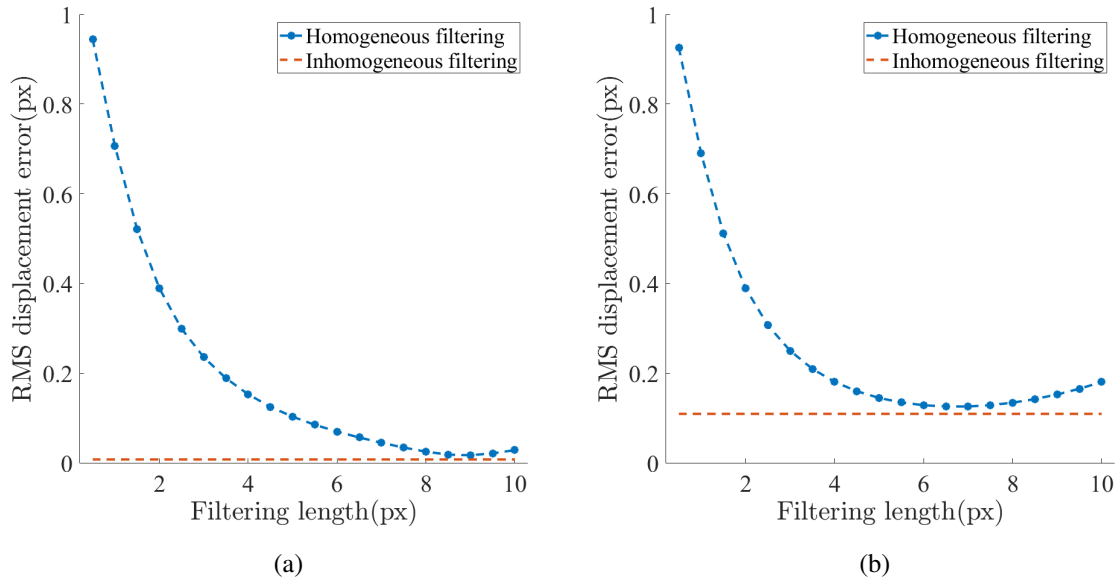
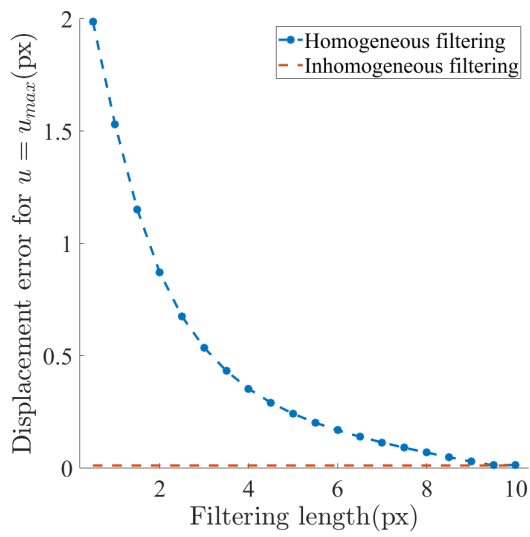
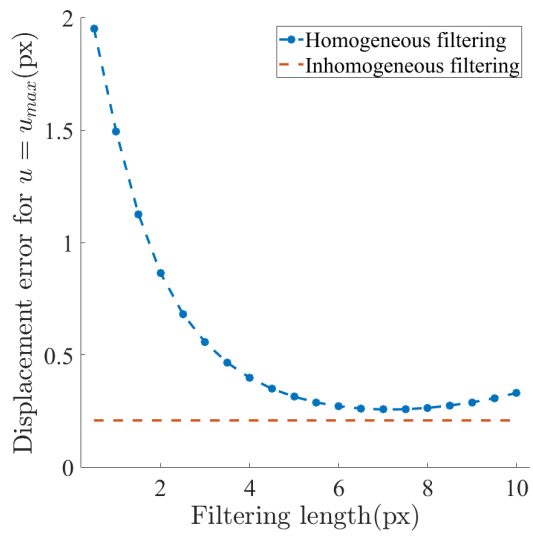


Figure B.3: One-step DIC error with homogeneous and inhomogeneous filtering over the whole set of displacement fields, for case 1 (a) and case 2 (b).

placement errors, when large ranges of displacements occur. Moreover, with a generic calibration, the results are relevant for two different artificial cases, while the best respective homogeneous filtering lengths differ.



(a)



(b)

Figure B.4: One-step DIC error with homogeneous and inhomogeneous filtering for the larger displacement magnitude, for case 1 (a) and case 2 (b).

Appendix C

Transformation between the real world and the camera frame

In Figure C.1, the experimental scheme is shown, and the relative parameters are presented in Table C.1.

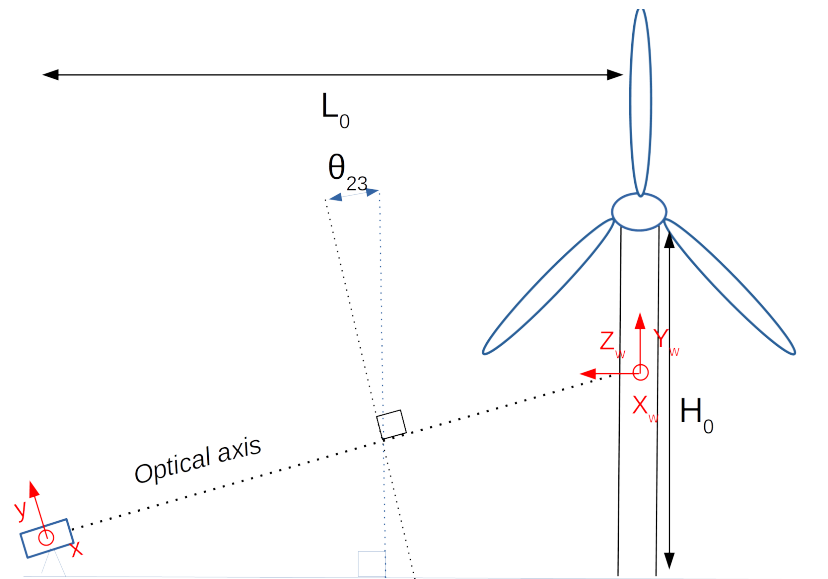


Figure C.1: Experimental scheme relative to the tower displacement measurement.

Table C.1: Experiment parameters

L_0	200 m
H_0	80 m
θ_{23}	10°

The shape functions used for DIC were calculated with an in-house finite element code. Between the observed reality and the calculated vibration modes, two different systems are considered. Indeed

a model describing the camera is needed to properly move from the "real" world to the camera system [Sutton et al., 2009]. Multiple transformations, through projection matrices, are to be taken into account. The geometric model for a camera is based on a pinhole projective model [Sutton et al., 2009, Dufour, 2015]. Let us consider a point in the real world frame R_w with coordinates (X_w, Y_w, Z_w) . The camera, associated to the system R_c has its origin at the camera center and the coordinates are denoted by (X_c, Y_c, Z_c) . The sensor system has coordinates (x, y) in pixels. Homogeneous coordinates are considered. The following transformation between R_w and R_c are considered first

$$\{\mathbf{X}_c\} = [\mathbf{F}] \cdot \{\mathbf{X}_w\} \quad (\text{C.1})$$

with

$$[\mathbf{F}] = \begin{bmatrix} [\mathbf{R}_{rot}] & \mathbf{t} \\ [\mathbf{0}^F] & 1 \end{bmatrix} \quad (\text{C.2})$$

where \mathbf{R}^{rot} is a rotation tensor and \mathbf{t} a translation vector. Then the projection from the camera system to the sensor system is related to a transformation matrix \mathbf{L}

$$\{\mathbf{x}\} = [\mathbf{L}] \cdot \{\mathbf{X}_c\} \quad (\text{C.3})$$

so that

$$[\mathbf{x}] = \begin{bmatrix} f_x & s_{xy} & x_0 & 0 \\ 0 & f_y & y_0 & 0 \\ 0 & 0 & 1 & 0 \end{bmatrix} \{\mathbf{X}_c\} \quad (\text{C.4})$$

where f_x and f_y are parameters including the scale factors and the focal length of the pinhole system along x and y directions, x_0 and y_0 the projections of the structure center point taken as reference, s_{xy} is relative to the consideration of skewed pixel. Thus, the global transformation between the real world and the camera frame is expressed as

$$\{\mathbf{x}\} = [\mathbf{L}] \cdot [\mathbf{F}] \cdot \{\mathbf{X}_w\} \quad (\text{C.5})$$

Considering the experimental set-up, the relative transformations between the real world and the camera frame then reduce to

$$\begin{Bmatrix} x \\ y \end{Bmatrix} = \begin{Bmatrix} f_x \frac{R_{11}^{rot} X_w}{Y_w R_{32}^{rot} + L_0} \\ f_y \frac{R_{22}^{rot} Y_w}{Y_w R_{32}^{rot} + L_0} \end{Bmatrix} \quad (\text{C.6})$$

The only rotation to consider is due to the inclination of the optical axis with respect to the ground. This angle is about 10° , thus the assumption $\sin(\theta) \approx \theta$ is valid.

The optical distortions between both systems are related to the $Y_w R_{32}^{rot}$ term with respect to L_0

term. They are maximum for the pixels situated on the, upper or lower, image extremity. The corresponding real world points are located at the upper and lower tower extremities. For them $Y_w = \pm \frac{H_0}{2}$, considering that the real world origin is at the middle height of the tower. Thus, relative distortions of 3.5 % are to be accounted for. It is very small, and it has been shown in Section 5.3.3 that the modal analysis gave the same results with small modifications of the vibration modes inputs. Thus, these distortions were not taken into account.

Appendix D

Résumé étendu en Français

Avec le vieillissement des parcs éoliens dans le monde entier, la certification de l'intégrité des turbines devient un enjeu industriel majeur pour optimiser la gestion des actifs et garantir la sécurité du public et des techniciens travaillant sur site. En particulier, la prolongation de la durée de vie des fermes et le *repowering* sont envisagés pour amortir les coûts et rendre l'énergie éolienne plus compétitive [Loraux, 2018]. La tour est un élément essentiel puisqu'un incident fatal ne peut en aucun cas se produire. Le calcul de la durée de vie des tours d'éoliennes est basé sur le calcul de l'endommagement au sens de Miner [Miner et al., 1945] en utilisant les courbes de Wohler [Wöhler, 1867]. Des logiciels aéroélastiques [Milano et al., 2019] couplés à des algorithmes de comptage *rainflow* [Musallam and Johnson, 2012] permettent de calculer la fréquence de répétition d'une gamme de contraintes. Les normes exigent que la durée de vie dépasse la durée d'exploitation, qui est actuellement de 20 ans [IEC, 2005]. Cette forme de calcul reste approximative et devrait nécessiter un recalibrage à partir des données de site pour une estimation plus certaine. Cependant, les marges étant importantes, les conceptions actuelles des tours d'éoliennes ne doivent normalement pas être remises en question. Des incidents structurels ont déjà été signalés, notamment des ruptures de boulons, de la corrosion ou des fissures dans les soudures [Lacalle et al., 2011, Chou and Tu, 2009, Chou and Tu, 2011, Chen et al., 2015]. Ce dernier type d'incident est principalement dû à une fatigue prématurée induite par un mauvais alignement des joints de soudure, des charges sous-estimées ou une concentration de contraintes due à un mauvais refroidissement des soudures [Lacalle et al., 2011]. Même si leur nombre est très faible par rapport au nombre de turbines installées, des tours se sont déjà effondrées dans le monde entier. Les effondrements ne se produisent presque jamais dans des conditions de fonctionnement nominales, mais toujours dans des conditions de vent particulières. On peut supposer que la présence d'une fissure la rendra alors beaucoup plus susceptible de s'effondrer. Les deux modes de défaillance induits sont le flambage prématuré et la propagation fatale des fissures. Les analyses post-mortem permettent d'envisager les deux causes : des zones déformées ainsi que des parties fissurées sont souvent présentes. La première question à laquelle nous avons tenté de répondre dans ce travail de thèse est :

Comment l'intégrité de la tour d'une éolienne est-elle affectée par la présence d'un défaut ressemblant à une fissure ? Quel est le premier mode de défaillance correspondant ?

Une étude a été réalisée pour déterminer l'impact de la présence d'une fissure sur la résistance de la structure aux deux phénomènes d'effondrement mentionnés. Des simulations par éléments finis ont montré que le flambage de la tour était faiblement impacté pour des fissures allant jusqu'à 40 cm. La charge critique est abaissée d'environ 10 %, au maximum. Des expériences et des simulations effectuées dans la littérature avec des cylindres de même rapport d'aspect que les éoliennes corroborent ces résultats. La charge critique correspondant à la propagation fatale d'une fissure de 30 cm de long est environ trois fois inférieure à la charge critique de flambage. Un cas test de désalignement du rotor par rapport à la direction du vent lors d'une tempête a été simulé. Les charges nécessaires pour arracher la partie supérieure d'une tour, endommagée par une fissure de 30 cm de long, sont atteintes avec un désalignement de 20 degrés et une vitesse de vent de 60 m/s. De telles conditions ont déjà été signalées en France, par exemple. Ce cas test montre l'intérêt de détecter rapidement des fissures au sein de la structure. Une telle étude n'a jamais été faite dans le monde de l'éolien. Elle répond à une problématique cruciale du prolongement de la durée de vie d'une structure en se basant sur les retours d'expérience d'effondrement de tours.

Pour s'assurer de l'intégrité des structures des techniques de suivi de santé ont été développées. Deux types sont disponibles sur le marché industriel : les essais non destructifs ponctuels (magnétoscopie, ultrasons, courants de Foucault) et les techniques de surveillance en continu (accéléromètres, jauges de contrainte). Les premières ont l'avantage de permettre un contrôle exhaustif mais sont coûteuses, complexes à utiliser et non autonomes. Les secondes sont autonomes mais coûteuses et extrapolent un état de santé global de la structure à partir de données locales. Le risque est qu'un défaut reste *invisible* mais soit tout de même critique pour la structure. Il est donc essentiel de revisiter les outils de prédiction à partir de données de sites relatives à l'endommagement de la tour et des structures les supportant. Le compromis coût/bénéfice est un obstacle à la surveillance généralisée des tours d'éoliennes. Par conséquent, comme souligné dans la Réf. [Wymore et al., 2015], la recherche de nouvelles méthodes optiques pour la surveillance de ces structures fait sens afin de réduire les coûts et être non intrusif. La suggestion faite dans l'étude porte sur la détection des surfaces endommagées, comme la corrosion. Ces méthodes ont été explorées pour les pales de turbines [Wang and Zhang, 2017], mais aucun travail n'est à mentionner pour les tours. Dans le cadre exposé, la Corrélation d'Images Numériques [Sutton et al., 2009, Besnard et al., 2006] (CIN) est la technique choisie pour développer de nouvelles méthodes qui permettraient de surmonter les limites des méthodes précédemment citées. La CIN fournit une mesure de champ en termes de déplacement, dont l'exploitation peut permettre une interprétation plus directe de la nature de tout endommagement mécanique observé [Hild et al., 2015]. Ainsi, la deuxième question à laquelle nous avons tenté de répondre au cours de ce travail est :

Comment la CIN peut-elle être utilisée afin de certifier l'intégrité d'une tour d'éolienne ?

Pour aborder ce problème, deux approches à différentes échelles ont été considérées. La première, à échelle macroscopique, consiste à reconstruire le champ de déplacement de l'éolienne dans sa globalité. La présence d'un défaut pourra être assimilée à une perte d'inertie géométrique [Marante et al., 2012], et donc une discontinuité dans le champ de rotation. Les défis relatifs à cette partie étaient doubles : l'absence de contraste sur la tour et la prise de photos en extérieur sur une grande structure dont les mouvements sont faibles par rapport à la résolution de la caméra. Dans la littérature, peu de dispositifs optiques ont été proposés pour mesurer les déplacements de tours d'éoliennes [Özbek, 2013]. La CIN a été utilisée seulement pour des applications portant sur les pâles d'éoliennes, pour la caractérisation modale [Baquersad et al., 2012] ou l'identification de défaut [Le Blanc et al., 2011].

Une approche par CIN intégrée a été utilisée [Hild et al., 2009, Dufour et al., 2014] afin de diminuer le nombre d'inconnues du problème et réduire les incertitudes de mesures. Les fonctions de forme considérées étaient les modes de vibration d'un code éléments poutres, la mesure étant faite sous sollicitations dynamiques. A cela s'ajoutait une fonction de forme de mouvement latéral de corps rigide. En ne considérant que les deux premiers modes de vibration et le mouvement de corps rigide, l'incertitude de mesure associée à l'amplitude du premier mode est de 0.15 mm en haut de tour (ce mode est associée à la flexion de la tour). La prise de vue était faite à 200 m environ, un pixel correspondant à 3 cm. Une formulation adaptée à la détection d'endommagement a été développée, basée sur son champ de sensibilité associé. Un cas de comparaison entre un modèle éléments finis 3D et le modèle poutre a permis de réaliser une équivalence longueur de fissure, endommagement. Il a été montré que l'endommagement équivalent à une fissure de 30 cm, ne serait pas détectable même en considérant 2000 images. Cependant, le cadre établi a permis de mesurer directement les fréquences propres de la tour en s'intéressant directement aux amplitudes associées aux modes de vibration. La première fréquence propre a été mesurée en couplant DIC instantanée et analyse fréquentielle du signal. La contribution du deuxième mode de vibration étant très faible, le cadre spatio-temporel de la CIN a été exploité. Le champ de déplacement mesuré par DIC instantanée, avec premier mode de vibration et mouvement de corps rigide, a été utilisé comme initialisation du déplacement. La contribution du second mode de vibration a été directement recherchée temporellement sous forme harmonique. La fréquence de vibration est celle qui maximise la contribution de ce second mode. Pour trois expériences sur quatre, cette seconde fréquence propre a pu être déterminée.

La détection de défaut étant difficile à l'échelle macroscopique, une stratégie de contrôle de la structure à l'échelle mésoscopique a été proposée. Celle-ci se base sur un dispositif de caméras bon marché à l'intérieur de l'éolienne couvrant les soudures circonférentielles au niveau des zones de plus fortes contraintes.

La plupart des techniques de détection d'endommagement par caméra sont basées sur des méthodes de suivi de contour [Dare et al., 2002, Abdel-Qader et al., 2003] afin d'identifier des fissures qui apparaissent en surface. La réussite de ces techniques suppose que le défaut soit traversant, et que la fissure soit clairement visible, ce qui présente des difficultés de robustesse. La CIN est connue pour

permettre de caractériser les fissures de manière précise [Roux et al., 2009]. Les chargements subis par une éolienne sont répétitifs dans le temps. Cet aspect statistique est exploitée dans une nouvelle méthode de détection d'endommagement afin de gagner en robustesse. Lorsque la structure est considérée comme saine, chaque caméra mesure des champs de déplacements par CIN au cours du temps. Grâce à des techniques de réduction de modèle, type PCA ou POD, une base modale caractéristique du déplacement est établie. Le champ de déplacement peut alors être réduit à un petit nombre de degrés de liberté. Après établissement de ces modes représentatifs lors d'une phase de calibration, les champs de déplacement sont mesurés au cours du temps et projetés sur la base modale. Si un défaut sous-jacent ou traversant apparaît, celui-ci induira une perturbation du champ de déplacement qui pourra être détecté grâce à l'erreur de projection en déplacement. La norme des résidus de corrélation après projection est également un bon indicateur pour la détection d'endommagement. Si les valeurs des indicateurs sont supérieures à une certaine valeur définie lors de l'étape de calibrage, une alerte sera donnée par le système. Cette méthode est robuste par le fait que même un défaut sous-jacent induira une perturbation sur le champ de déplacement en surface et pourra donc être détecté. L'étape de projection du champ de déplacement étant réalisé de nombreuses fois, et celle-ci s'apparentant à de la CIN intégrée (les fonctions de forme spatiales étant les modes déterminés lors de l'étape de calibration), il a été imaginé de ramener cette étape à une unique itération. Le concept d'*extracteurs* associés à chaque mode de déplacement a été introduit. Un simple produit scalaire entre ceux-ci et les résidus permet d'obtenir directement les amplitudes modales. La statistique des amplitudes du champ de déplacement est disponible pour chaque pixel de la région d'intérêt. A partir de cette information, un filtrage optimisé des images est réalisé afin d'être en mesure de réaliser cette CIN en une seule itération.

L'une des motivations de ce travail de doctorat était de réduire les incertitudes de mesure, afin de pouvoir détecter l'endommagement. Par conséquent, un cadre mathématique de la CIN optimale avec N champs a été proposé et validé pour des images en couleur (trois champs). Un traitement spécifique des images à N champs a été mis en place. Tout d'abord, le bruit de Poisson de chaque champ est normalisé grâce à une transformation d'Anscombe. Ensuite, les espaces propres relatifs au bruit d'acquisition sont déterminés. Les champs sont projetés sur l'espace propre pour se placer dans le cadre mathématique optimal et effectuer le calcul de la CIN. Pour une caméra couleur standard, les incertitudes de mesure varient d'un facteur 2 selon la transformation et le schéma de corrélation choisis, par rapport au cadre optimal.

Ainsi dans le cadre de cette thèse plusieurs problématiques concernant la maintenance des tours d'éoliennes ont été abordées. D'un point de vue structurel, une nouvelle méthode de certification de l'intégrité a été étudiée pour une tour endommagée. Ensuite, des méthodes optiques innovantes non intrusives ou autonomes ont été proposées pour caractériser l'état de santé structurel basées sur la CIN. Ceci a permis le développement de nouveaux algorithmes permettant la détection automatique de défauts et la minimisation d'incertitude de mesure lorsque plusieurs champs d'information sont disponibles.

Bibliography

- [Abdel-Qader et al., 2003] Abdel-Qader, I., Abudayyeh, O., and Kelly, M. E. (2003). Analysis of edge-detection techniques for crack identification in bridges. *Journal of Computing in Civil Engineering*, 17(4):255–263.
- [Akrami and Erfani, 2017] Akrami, V. and Erfani, S. (2017). An analytical and numerical study on the buckling of cracked cylindrical shells. *Thin-Walled Structures*, 119:457–469.
- [Alipour and Harris, 2020] Alipour, M. and Harris, D. K. (2020). Increasing the robustness of material-specific deep learning models for crack detection across different materials. *Engineering Structures*, 206:110157.
- [Anscombe, 1948] Anscombe, F. J. (1948). The transformation of Poisson, binomial and negative-binomial data. *Biometrika*, 35(3/4):246–254.
- [Anuta, 1970] Anuta, P. E. (1970). Spatial registration of multispectral and multitemporal digital imagery using fast fourier transform techniques. *IEEE transactions on Geoscience Electronics*, 8(4):353–368.
- [Arducam, 2020] Arducam (2020). Arducam website. "<https://www.arducam.com/raspberry-pi-camera-pinout/>".
- [Baldi, 2018] Baldi, A. (2018). Digital image correlation and color cameras. *Experimental Mechanics*, 58(2):315–333.
- [Bang et al., 2012] Bang, H.-J., Ko, S.-W., Jang, M.-S., and Kim, H.-I. (2012). Shape estimation and health monitoring of wind turbine tower using a fbg sensor array. In *2012 IEEE International Instrumentation and Measurement Technology Conference Proceedings*, pages 496–500. IEEE.
- [Baqersad et al., 2012] Baqersad, J., Carr, J., Lundstrom, T., Niezrecki, C., Avitabile, P., and Slattery, M. (2012). Dynamic characteristics of a wind turbine blade using 3D digital image correlation. In *Health Monitoring of Structural and Biological Systems 2012*, volume 8348, page 83482I. International Society for Optics and Photonics.

- [Baqersad et al., 2017] Baqersad, J., Poozesh, P., Niezrecki, C., and Avitabile, P. (2017). Photogrammetry and optical methods in structural dynamics—a review. *Mechanical Systems and Signal Processing*, 86:17–34.
- [Barsoum, 1974] Barsoum, R. S. (1974). Application of quadratic isoparametric finite elements in linear fracture mechanics. *International Journal of Fracture*, 10(4):603–605.
- [Bassett et al., 2010] Bassett, K., Carriveau, R., and Ting, D. S. K. (2010). Vibration analysis of 2.3 mw wind turbine operation using the discrete wavelet transform. *Wind Engineering*, 34(4):375–388.
- [Bayer, 1976] Bayer, B. E. (1976). Color imaging array. *US patent 3,971,065*.
- [Beard and Lowe, 2003] Beard, M. D. and Lowe, M. J. S. (2003). Non-destructive testing of rock bolts using guided ultrasonic waves. *International journal of rock mechanics and mining sciences*, 40(4):527–536.
- [Beberriss et al., 2012] Bebernis, T., Eason, T., and Spottswood, S. (2012). High-speed 3D digital image correlation measurement of long-duration random vibration; recent advancements and noted limitations. In *ISMA Biennial Conference, Lueven, Belgium*.
- [Beganovic and Söffker, 2016] Beganovic, N. and Söffker, D. (2016). Structural health management utilization for lifetime prognosis and advanced control strategy deployment of wind turbines: An overview and outlook concerning actual methods, tools, and obtained results. *Renewable and Sustainable Energy Reviews*, 64:68–83.
- [Benedetti et al., 2011] Benedetti, M., Fontanari, V., and Zonta, D. (2011). Structural health monitoring of wind towers: remote damage detection using strain sensors. *Smart Materials and Structures*, 20(5):055009.
- [Beremin et al., 1983] Beremin, F. M., Pineau, A., Mudry, F., Devaux, J.-C., D’Escatha, Y., and Ledermann, P. (1983). A local criterion for cleavage fracture of a nuclear pressure vessel steel. *Metallurgical transactions A*, 14(11):2277–2287.
- [Berny et al., 2018] Berny, M., Jailin, C., Bouterf, A., Hild, F., and Roux, S. (2018). Mode-enhanced space-time DIC: applications to ultra-high-speed imaging. *Measurement Science and Technology*, 29(12):125008.
- [Besnard et al., 2011] Besnard, G., Guérard, S., Roux, S., and Hild, F. (2011). A space-time approach in digital image correlation: Movie-DIC. *Optics and Lasers in Engineering*, 49(1):71–81.
- [Besnard et al., 2006] Besnard, G., Hild, F., and Roux, S. (2006). “Finite-element” displacement fields analysis from digital images: application to Portevin–Le Châtelier bands. *Experimental Mechanics*, 46(6):789–803.

- [Bhandari and Deshpande, 2008] Bhandari, S. H. and Deshpande, S. M. (2008). A simple approach to surface defect detection. *2008 IEEE Region*, 10:8–10.
- [Bolhassani et al., 2016] Bolhassani, M., Rajaram, S., Hamid, A. A., Kontsos, A., and Bartoli, I. (2016). Damage detection of concrete masonry structures by enhancing deformation measurement using DIC. In *Nondestructive Characterization and Monitoring of Advanced Materials, Aerospace, and Civil Infrastructure 2016*, volume 9804, page 980411. International Society for Optics and Photonics.
- [Bouchara et al., 2007] Bouchara, F., Bertrand, M., Ramdani, S., and Haydar, M. (2007). Sub-pixel edge fitting using b-spline. In *International Conference on Computer Vision/Computer Graphics Collaboration Techniques and Applications*, pages 353–364. Springer.
- [Brazier, 1927] Brazier, L. G. (1927). On the flexure of thin cylindrical shells and other "thin" sections. *Proceedings of the Royal society of London. Series A, containing papers of a mathematical and physical character*, 116(773):104–114.
- [Bruck et al., 1989] Bruck, H. A., McNeill, S. R., Sutton, M. A., and Peters, W. H. (1989). Digital image correlation using newton-raphson method of partial differential correction. *Experimental mechanics*, 29(3):261–267.
- [Buades et al., 2009] Buades, T., Lou, Y., Morel, J.-M., and Tang, Z. (2009). A note on multi-image denoising. In *2009 International Workshop on Local and Non-Local Approximation in Image Processing*, pages 1–15. IEEE.
- [Bui, 1978] Bui, H. D. (1978). *Mécanique de la rupture fragile*, volume 109. Masson Paris.
- [Bushnell, 1974] Bushnell, D. (1974). Bifurcation buckling of shells of revolution including large deflections, plasticity and creep. *International Journal of Solids and Structures*, 10(11):1287–1305.
- [Camp et al., 2013] Camp, G., Carreaud, P., and Lançon, H. (2013). Large structures: which solutions for health monitoring. In *International Archives of the Photogrammetry, Remote Sensing and Spatial Information Sciences. XXIV ICIPA Symposium*, volume 5, page W2.
- [Canny, 1986] Canny, J. (1986). A computational approach to edge detection. *IEEE Transactions on pattern analysis and machine intelligence*, 8:679–698.
- [Capaldo et al., 2020] Capaldo, M., Orsatelli, J.-B., Curt, J., and Julan, E. (2020). Influence of cracks on the buckling of wind turbine towers. In *Journal of Physics: Conference Series*, volume 1618, page 022001. IOP Publishing.

- [Carlin et al., 2003] Carlin, P. W., Laxson, A. S., and Muljadi, E. B. (2003). The history and state of the art of variable-speed wind turbine technology. *Wind Energy: An International Journal for Progress and Applications in Wind Power Conversion Technology*, 6(2):129–159.
- [Charbal, 2017] Charbal, A. (2017). *Mesure de champs thermomécaniques pour l'étude de la fatigue par chocs thermiques*. PhD thesis, Université Paris-Saclay.
- [Charbal et al., 2016a] Charbal, A., Dufour, J., Guery, A., Hild, F., Roux, S., Vincent, L., and Poncelet, M. (2016a). Integrated digital image correlation considering gray level and blur variations: Application to distortion measurements of IR camera. *Optics and Lasers in Engineering*, 78:75–85.
- [Charbal et al., 2016b] Charbal, A., Dufour, J.-E., Hild, F., Poncelet, M., Vincent, L., and Roux, S. (2016b). Hybrid stereocorrelation using infrared and visible light cameras. *Experimental Mechanics*, 56(5):845–860.
- [Chatterjee, 2000] Chatterjee, A. (2000). An introduction to the proper orthogonal decomposition. *Current science*, pages 808–817.
- [Chauhan et al., 2011] Chauhan, S., Tcherniak, D., Basurko, J., Salgado, O., Urresti, I., Carcangiu, C. E., and Rossetti, M. (2011). Operational modal analysis of operating wind turbines: application to measured data. In *Rotating Machinery, Structural Health Monitoring, Shock and Vibration, Volume 5*, pages 65–81. Springer.
- [Chen et al., 2015] Chen, X., Li, C., and Xu, J. (2015). Failure investigation on a coastal wind farm damaged by super typhoon: A forensic engineering study. *Journal of Wind Engineering and Industrial Aerodynamics*, 147:132–142.
- [Chen and Xu, 2016] Chen, X. and Xu, J. Z. (2016). Structural failure analysis of wind turbines impacted by super typhoon usagi. *Engineering Failure Analysis*, 60:391–404.
- [Chiaruttini et al., 2013] Chiaruttini, V., Riolo, V., and Feyel, F. (2013). Advanced remeshing techniques for complex 3d crack propagation. In *Icf13*.
- [Chinesta et al., 2010] Chinesta, F., Ammar, A., and Cueto, E. (2010). Recent advances and new challenges in the use of the proper generalized decomposition for solving multidimensional models. *Archives of Computational methods in Engineering*, 17(4):327–350.
- [Chou et al., 2018] Chou, J.-S., Ou, Y.-C., Lin, K.-Y., and Wang, Z.-J. (2018). Structural failure simulation of onshore wind turbines impacted by strong winds. *Engineering Structures*, 162:257–269.

- [Chou and Tu, 2009] Chou, J.-S. and Tu, W.-T. (2009). Lessons learned from a collapsed wind turbine tower in taiwan. In *Proceedings of the International Conference on Computing in Civil and Building Engineering*.
- [Chou and Tu, 2011] Chou, J.-S. and Tu, W.-T. (2011). Failure analysis and risk management of a collapsed large wind turbine tower. *Engineering Failure Analysis*, 18(1):295–313.
- [Chu et al., 1985] Chu, T. C., Ranson, W. F., and Sutton, M. A. (1985). Applications of digital-image-correlation techniques to experimental mechanics. *Experimental mechanics*, 25(3):232–244.
- [Chung and Chan, 2006] Chung, K.-H. and Chan, Y.-H. (2006). Color demosaicing using variance of color differences. *IEEE transactions on image processing*, 15(10):2944–2955.
- [Cicero et al., 2009] Cicero, S., Lacalle, R., and Cicero, R. (2009). Estimation of the maximum allowable lack of penetration defects in circumferential butt welds of structural tubular towers. *Engineering structures*, 31(9):2123–2131.
- [CIE, 1932] CIE (1932). Commission internationale de l'éclairage proceedings, 1931. *Cambridge University, Cambridge*.
- [Cinar et al., 2017] Cinar, A. F., Barhli, S. M., Hollis, D., Flansbjer, M., Tomlinson, R. A., Marrow, T. J., and Mostafavi, M. (2017). An autonomous surface discontinuity detection and quantification method by digital image correlation and phase congruency. *Optics and Lasers in Engineering*, 96:94–106.
- [Claire et al., 2004] Claire, D., Hild, F., and Roux, S. (2004). A finite element formulation to identify damage fields: the equilibrium gap method. *International journal for numerical methods in engineering*, 61(2):189–208.
- [Claire et al., 2007] Claire, D., Hild, F., and Roux, S. (2007). Identification of a damage law by using full-field displacement measurements. *International Journal of Damage Mechanics*, 16(2):179–197.
- [Coulthard, 1989] Coulthard, M. A. (1989). Image processing for automatic surface defect detection. In *Third International Conference on Image Processing and its Applications, 1989.*, pages 192–196. IET.
- [Curt et al., 2020a] Curt, J., Capaldo, M., Hild, F., and Roux, S. (2020a). Modal analysis of a wind turbine tower by digital image correlation. In *Journal of Physics: Conference Series*, volume 1618, page 022002. IOP Publishing.
- [Curt et al., 2020b] Curt, J., Capaldo, M., Hild, F., and Roux, S. (2020b). Optimal digital color image correlation. *Optics and Lasers in Engineering*, 127:105896.

- [Dai et al., 2017] Dai, K., Sheng, C., Zhao, Z., Yi, Z., Camara, A., and Bitsuamlak, G. (2017). Non-linear response history analysis and collapse mode study of a wind turbine tower subjected to tropical cyclonic winds. *Wind and Structures*, 25(1):79–100.
- [Dao et al., 2019] Dao, C., Kazemtabrizi, B., and Crabtree, C. (2019). Wind turbine reliability data review and impacts on levelised cost of energy. *Wind Energy*, 22(12):1848–1871.
- [Dare et al., 2002] Dare, P., Hanley, H., Fraser, C., Riedel, B., and Niemeier, W. (2002). An operational application of automatic feature extraction: the measurement of cracks in concrete structures. *The Photogrammetric Record*, 17(99):453–464.
- [Devriendt et al., 2014] Devriendt, C., Weijtjens, W., El-Kafafy, M., and De Sitter, G. (2014). Monitoring resonant frequencies and damping values of an offshore wind turbine in parked conditions. *IET Renewable Power Generation*, 8(4):433–441.
- [Dillian et al., 2017] Dillian, S. K., Cerqueira, S. C., and Ali, A.-Q. H. (2017). Cracking propagation prediction methodology applied for a bulk carrier. *FME Transactions*, 45(3):428–434.
- [Dimopoulos and Gantes, 2012] Dimopoulos, C. A. and Gantes, C. J. (2012). Experimental investigation of buckling of wind turbine tower cylindrical shells with opening and stiffening under bending. *Thin-Walled Structures*, 54:140–155.
- [Dufour, 2015] Dufour, J.-E. (2015). *Mesures de forme, de déplacement, et de paramètres mécaniques parstéréo-corrélation d’images isogéométrique*. PhD thesis, Université Paris-Saclay (ComUE).
- [Dufour et al., 2014] Dufour, J.-E., Hild, F., and Roux, S. (2014). Integrated digital image correlation for the evaluation and correction of optical distortions. *Optics and Lasers in Engineering*, 56:121–133.
- [Dung, 2019] Dung, C. V. (2019). Autonomous concrete crack detection using deep fully convolutional neural network. *Automation in Construction*, 99:52–58.
- [Dung et al., 2019] Dung, C. V., Sekiya, H., Hirano, S., Okatani, T., and Miki, C. (2019). A vision-based method for crack detection in gusset plate welded joints of steel bridges using deep convolutional neural networks. *Automation in Construction*, 102:217–229.
- [EDF, 2011] EDF (2011). *Hexahedral element at a point of integration, stabilized by the method "Assumed Strain"*. EDF Research and Development. R3.06.11.
- [EDF, 2013] EDF (2013). *Methods of piloting of the loading*. EDF Research and Development. R5.03.80.

- [EDF, 2017a] EDF (2017a). Code analyses des structures et thermomécanique pour des études et des recherches.
- [EDF, 2017b] EDF (2017b). *Operator CALC G*. EDF Research and Development. U4.82.03.
- [EDF, 2018] EDF (2018). *Characterization of wind turbine towers*. EDF Research and Development (internal report).
- [EDF-Renewables, 2020] EDF-Renewables (2020). Website: key figures. <https://www.edf-renouvelables.com/en/>.
- [El Bartali et al., 2008] El Bartali, A., Aubin, V., and Degallaix, S. (2008). Fatigue damage analysis in a duplex stainless steel by digital image correlation technique. *Fatigue & Fracture of Engineering Materials & Structures*, 31(2):137–151.
- [Eleftheroglou et al., 2018] Eleftheroglou, N., Zarouchas, D., Loutas, T., Alderliesten, R., and Benedictus, R. (2018). Structural health monitoring data fusion for in-situ life prognosis of composite structures. *Reliability Engineering & System Safety*, 178:40–54.
- [Eshelby, 1957] Eshelby, J. D. (1957). The determination of the elastic field of an ellipsoidal inclusion, and related problems. *Proceedings of the royal society of London. Series A. Mathematical and physical sciences*, 241(1226):376–396.
- [EWEA, 2019] EWEA (2019). Wind in power: 2018 european statistics (february).
- [Farrar and Worden, 2007] Farrar, C. R. and Worden, K. (2007). An introduction to structural health monitoring. *Philosophical Transactions of the Royal Society A: Mathematical, Physical and Engineering Sciences*, 365(1851):303–315.
- [Force-Technology, 2020] Force-Technology (2020). Force technology website. "<https://forcetechnology.com/en/services/ndt-on-wind-turbines>".
- [Forsey and Gungor, 2016] Forsey, A. and Gungor, S. (2016). Demosaicing images from colour cameras for digital image correlation. *Optics and lasers in engineering*, 86:20–28.
- [France-3, 2018] France-3 (2018). Pithiverais : Une éolienne s'effondre à guigneville (loiret). *France 3 Centre-Val de Loire*.
- [Fu and He, 2001] Fu, Z.-F. and He, J. (2001). *Modal analysis*. Elsevier.
- [Futuren, 2020] Futuren (2020). Futuren website. "<https://www.futuren-group.com>".
- [Galappaththi et al., 2012] Galappaththi, U. I. K., De Silva, A. K. M., Macdonald, M., and Adewale, O. R. (2012). Review of inspection and quality control techniques for composite wind turbine blades. *Insight-Non-Destructive Testing and Condition Monitoring*, 54(2):82–85.

- [Gamot et al., 2019] Gamot, J., Lasserre, T., Richard, L., Neggers, J., Swiergiel, N., and Hild, F. (2019). Calibrating thermoelastic stress analysis with integrated digital image correlation: Application to fatigue cracks. *The Journal of Strain Analysis for Engineering Design*, 54(5-6):320–330.
- [Gao et al., 2019] Gao, Q., Liu, S., Fan, J., and Shen, Z. (2019). Wind-induced fatigue analysis of wind turbine steel tower. In *IOP Conference Series: Earth and Environmental Science*, volume 310, page 032007. IOP Publishing.
- [García-Martín et al., 2011] García-Martín, J., Gómez-Gil, J., and Vázquez-Sánchez, E. (2011). Non-destructive techniques based on eddy current testing. *Sensors*, 11(3):2525–2565.
- [Gentile and Bernardini, 2010] Gentile, C. and Bernardini, G. (2010). An interferometric radar for non-contact measurement of deflections on civil engineering structures: laboratory and full-scale tests. *Structure and Infrastructure Engineering*, 6(5):521–534.
- [Gerard and Becker, 1957] Gerard, G. and Becker, H. (1957). Handbook of structural stability. part 3. buckling of curved plates and shells. Technical report, National Aeronautics And Space Administration Washington DC.
- [Glauert, 1935] Glauert, H. (1935). Airplane propellers. In *Aerodynamic theory*, pages 169–360. Springer.
- [Gomes Perini et al., 2014] Gomes Perini, L. A., Passieux, J.-C., and Périé, J.-N. (2014). A multigrid PGD-based algorithm for volumetric displacement fields measurements. *Strain*, 50(4):355–367.
- [Grediac et al., 2006] Grediac, M., Pierron, F., Avril, S., and Toussaint, E. (2006). The virtual fields method for extracting constitutive parameters from full-field measurements: a review. *Strain*, 42(4):233–253.
- [Griffith, 1921] Griffith, A. A. (1921). VI. The phenomena of rupture and flow in solids. *Philosophical transactions of the royal society of london. Series A, containing papers of a mathematical or physical character*, 221(582-593):163–198.
- [Gueguen et al., 2010] Gueguen, P., Jolivet, V., Michel, C., and Schweitzer, A.-S. (2010). Comparison of velocimeter and coherent lidar measurements for building frequency assessment. *Bulletin of Earthquake Engineering*, 8(2):327–338.
- [Guery et al., 2016] Guery, A., Hild, F., Latourte, F., and Roux, S. (2016). Identification of crystal plasticity parameters using DIC measurements and weighted FEMU. *Mechanics of Materials*, 100:55–71.
- [Guo et al., 2011] Guo, L., Uang, C.-M., Elgamal, A., Prowell, I., and Zhang, S. (2011). Pushover analysis of a 53 m high wind turbine tower. *Advanced Science Letters*, 4(3):656–662.

- [Ha et al., 2015] Ha, N. S., Vang, H. M., and Goo, N. S. (2015). Modal analysis using digital image correlation technique: an application to artificial wing mimicking beetle’s hind wing. *Experimental Mechanics*, 55(5):989–998.
- [Hagara and Kulla, 2011] Hagara, M. and Kulla, P. (2011). Edge detection with sub-pixel accuracy based on approximation of edge with erf function. *Radioengineering*, 20(2):516–524.
- [Hamam et al., 2007] Hamam, R., Hild, F., and Roux, S. (2007). Stress intensity factor gauging by digital image correlation: Application in cyclic fatigue. *Strain*, 43(3):181–192.
- [Hang et al., 2016] Hang, D., Hassan, G. M., MacNish, C., and Dyskin, A. (2016). Characteristics of color digital image correlation for deformation measurement in geomechanical structures. In *Digital Image Computing: Techniques and Applications (DICTA), 2016 International Conference on*, pages 1–8. IEEE.
- [Hansen, 2003] Hansen, M. H. (2003). Improved modal dynamics of wind turbines to avoid stall-induced vibrations. *Wind Energy: An International Journal for Progress and Applications in Wind Power Conversion Technology*, 6(2):179–195.
- [Hao et al., 2017] Hao, W., Zhu, J., Zhu, Q., Chen, L., and Li, L. (2017). Displacement field denoising for high-temperature digital image correlation using principal component analysis. *Mechanics of Advanced Materials and Structures*, 24(10):830–839.
- [Harrison et al., 2008] Harrison, G. P., Cradden, L. C., and Chick, J. P. (2008). Preliminary assessment of climate change impacts on the uk onshore wind energy resource. *Energy Sources, Part A*, 30(14-15):1286–1299.
- [Heilmann et al., 2014] Heilmann, C., Grunwald, A., Melsheimer, M., Liebich, R., and Kamieth, R. (2014). Reconstruction of a wind turbine’s endured load spectrum using a short-time load measurement and operational data. *Proceeding of EWEA 2014*.
- [Hermosilla et al., 2008] Hermosilla, T., Bermejo, E., Balaguer, A., and Ruiz, L. A. (2008). Non-linear fourth-order image interpolation for subpixel edge detection and localization. *Image and vision computing*, 26(9):1240–1248.
- [Higham and Higham, 2017] Higham, D. J. and Higham, N. J. (2017). *MATLAB guide*, volume 150. Siam.
- [Hild et al., 2015] Hild, F., Bouterf, A., and Roux, S. (2015). Damage measurements via DIC. *International Journal of Fracture*, 191:77–105.
- [Hild et al., 2002] Hild, F., Raka, B., Baudequin, M., Roux, S., and Cantelaube, F. (2002). Multiscale displacement field measurements of compressed mineral-wool samples by digital image correlation. *Applied Optics*, 41:6815–6828.

- [Hild and Roux, 2012a] Hild, F. and Roux, S. (2012a). Comparison of local and global approaches to digital image correlation. *Experimental Mechanics*, 52(9):1503–1519.
- [Hild and Roux, 2012b] Hild, F. and Roux, S. (2012b). Digital Image Correlation. In Rastogi, P. and Hack, E., editors, *Optical Methods for Solid Mechanics. A Full-Field Approach*, pages 183–228, Weinheim (Germany). Wiley-VCH.
- [Hild and Roux, 2012c] Hild, F. and Roux, S. (2012c). Digital image correlation. *Optical Methods for Solid Mechanics. A Full-Field Approach*, pages 183–228.
- [Hild et al., 2009] Hild, F., Roux, S., Gras, R., Guerrero, N., Marante, M. E., and Flórez-López, J. (2009). Displacement measurement technique for beam kinematics. *Optics and Lasers in Engineering*, 47(3-4):495–503.
- [Hildreth and Marr, 1980] Hildreth, E. and Marr, D. (1980). Theory of edge detection. *Proceedings of Royal Society of London*, 207(187-217):9.
- [Hirakawa and Parks, 2005] Hirakawa, K. and Parks, T. W. (2005). Adaptive homogeneity-directed demosaicing algorithm. *IEEE Transactions on Image Processing*, 14(3):360–369.
- [Hoa et al., 2010] Hoa, L. T., Tamura, Y., Yoshida, A., and Anh, N. D. (2010). Frequency domain versus time domain modal identifications for ambient excited structures. In *International Conference on Engineering Mechanics and Automation (ICEMA 2010)*, pages 1–2.
- [Hu et al., 2019] Hu, Y., Guo, W., Zhu, W., and Xu, Y. (2019). Local damage detection of membranes based on bayesian operational modal analysis and three-dimensional digital image correlation. *Mechanical Systems and Signal Processing*, 131:633–648.
- [Huchet, 2018] Huchet, Q. (2018). *Kriging based methods for the structural damage assessment of offshore wind turbines*. PhD thesis, Université Clermont Auvergne.
- [Hutchinson, 1974] Hutchinson, J. W. (1974). Plastic buckling. In *Advances in applied mechanics*, volume 14, pages 67–144. Elsevier.
- [Hutchinson et al., 1971] Hutchinson, J. W., Tennyson, R. C., and Muggeridge, D. B. (1971). Effect of a local axisymmetric imperfection on the buckling behavior of a circular cylindrical shell under axial compression. *AIAA journal*, 9(1):48–52.
- [IEC, 2005] IEC (2005). Wind turbines-part 1: Design requirements. *IEC 61400-1 Ed. 3*.
- [Indow, 1980] Indow, T. (1980). Global color metrics and color-appearance systems. *Color Research & Application*, 5(1):5–12.
- [Ingram, 2011] Ingram, G. (2011). Wind turbine blade analysis using the blade element momentum method. version 1.1. *Durham University, Durham*.

- [Irwin, 1957] Irwin, G. R. (1957). Analysis of stresses and strains near the end of a crack transversing a plate. *Trans. ASME, Ser. E, J. Appl. Mech.*, 24:361–364.
- [Jailin, 2018] Jailin, C. (2018). Full field modal measurement with a single standard camera. *Optics and Lasers in Engineering*, 107:265–272.
- [James et al., 1995] James, G. H., Carne, T. G., Lauffer, J. P., et al. (1995). The natural excitation technique (NExT) for modal parameter extraction from operating structures. *Modal Analysis-the International Journal of Analytical and Experimental Modal Analysis*, 10(4):260.
- [Jasinien et al., 2009] Jasinien, E., Raiutis, R., Voleiis, A., Vladiauskas, A., Mitchard, D., Amos, M., et al. (2009). Ndt of wind turbine blades using adapted ultrasonic and radiographic techniques. *Insight-Non-Destructive Testing and Condition Monitoring*, 51(9):477–483.
- [Jay et al., 2016] Jay, A., Myers, A. T., Torabian, S., Mahmoud, A., Smith, E., Agbayani, N., and Schafer, B. W. (2016). Spirally welded steel wind towers: Buckling experiments, analyses, and research needs. *Journal of Constructional Steel Research*, 125:218–226.
- [Jia et al., 2004] Jia, H., Murphey, Y. L., Shi, J., and Chang, T. (2004). An intelligent real-time vision system for surface defect detection. In *Proceedings of the 17th International Conference on Pattern Recognition, 2004. ICPR 2004.*, volume 3, pages 239–242. IEEE.
- [Johnson and Will, 1974] Johnson, C. P. and Will, K. M. (1974). Beam buckling by finite element procedure. *Journal of the Structural Division*, 100(Proc Paper 10432).
- [Joliffe and Morgan, 1992] Joliffe, I. T. and Morgan, B. J. T. (1992). Principal component analysis and exploratory factor analysis. *Statistical methods in medical research*, 1(1):69–95.
- [Jonkman, 2010] Jonkman, J. (2010). Definition of the floating system for phase IV of OC3. Technical report, National Renewable Energy Lab.(NREL), Golden, CO (United States).
- [Jonkman et al., 2009] Jonkman, J., Butterfield, S., Musial, W., and Scott, G. (2009). Definition of a 5-MW reference wind turbine for offshore system development. Technical report, National Renewable Energy Lab.(NREL), Golden, CO (United States).
- [Jonkman and Musial, 2010] Jonkman, J. and Musial, W. (2010). Offshore code comparison collaboration (OC3) for IEA wind task 23 offshore wind technology and deployment. Technical report, National Renewable Energy Lab.(NREL), Golden, CO (United States).
- [Kammers and Daly, 2013] Kammers, A. D. and Daly, S. (2013). Digital image correlation under scanning electron microscopy: methodology and validation. *Experimental Mechanics*, 53(9):1743–1761.

- [Kanninen, 1974] Kanninen, M. F. (1974). A dynamic analysis of unstable crack propagation and arrest in the DCB test specimen. *International Journal of Fracture*, 10(3):415–430.
- [Keating et al., 1975] Keating, T. J., Wolf, P. R., and Scarpace, F. L. (1975). An improved method of digital image correlation. *Photogrammetric Engineering and Remote Sensing*, 41(8):993–1002.
- [Khadka et al., 2019] Khadka, A., Dong, Y., and Baqersad, J. (2019). Structural Health Monitoring of Wind Turbines Using a Digital Image Correlation System on a UAV. In *Rotating Machinery, Optical Methods & Scanning LDV Methods, Volume 6*, pages 85–91. Springer.
- [Khadka et al., 2020] Khadka, A., Fick, B., Afshar, A., Tavakoli, M., and Baqersad, J. (2020). Non-contact vibration monitoring of rotating wind turbines using a semi-autonomous UAV. *Mechanical Systems and Signal Processing*, 138:106446.
- [Kumar and Verma, 2010] Kumar, T. and Verma, K. (2010). A theory based on conversion of RGB image to gray image. *International Journal of Computer Applications*, 7(2):7–10.
- [Lacalle et al., 2011] Lacalle, R., Cicero, S., Álvarez, J., Cicero, R., and Madrazo, V. (2011). On the analysis of the causes of cracking in a wind tower. *Engineering Failure Analysis*, 18(7):1698–1710.
- [Ladevèze, 2012] Ladevèze, P. (2012). *Nonlinear computational structural mechanics: new approaches and non-incremental methods of calculation*. Springer Science & Business Media.
- [Ladevèze, 2014] Ladevèze, P. (2014). Pgd in linear and nonlinear computational solid mechanics. In *Separated representations and PGD-based model reduction*, pages 91–152. Springer.
- [Lakshmi et al., 2013] Lakshmi, M. R., Mondal, A. K., Jadhav, C. K., Dutta, B. V., and Sreedhar, S. (2013). Overview of ndt methods applied on an aero engine turbine rotor blade. *Insight-Non-Destructive Testing and Condition Monitoring*, 55(9):482–486.
- [Le Blanc et al., 2011] Le Blanc, B., Niezrecki, C., Avitabile, P., Chen, J., Sherwood, J., and Hughes, S. (2011). Full-field inspection of a wind turbine blade using three-dimensional digital image correlation. In *Industrial and Commercial Applications of Smart Structures Technologies 2011*, volume 7979, page 79790L. International Society for Optics and Photonics.
- [Leblond, 2003] Leblond, J.-B. (2003). *Mécanique de la rupture fragile et ductile*. Hermès science publications.
- [Leclerc et al., 2015] Leclerc, H., Neggers, J., Mathieu, F., Roux, S., and Hild, F. (2015). Correli 3.0. *Agence pour la Protection des Programmes, Paris*, IDDN.FR.001.520008.000.S.P.2015.000.31500.
- [Lembrechts, 1988] Lembrechts, F. (1988). *Frequency domain identification techniques for experimental multiple input modal analysis*. PhD thesis, K.U. Leuven, Belgium.

- [Li et al., 2019] Li, X., Gao, C., Guo, Y., He, F., and Shao, Y. (2019). Cable surface damage detection in cable-stayed bridges using optical techniques and image mosaicking. *Optics & Laser Technology*, 110:36–43.
- [Liu and Ishihara, 2015] Liu, Y. and Ishihara, T. (2015). Fatigue failure accident of wind turbine tower in taikoyama wind power plant. *Measurement*, 15:20.
- [Longere et al., 2002] Longere, P., Zhang, X., Delahunt, P. B., and Brainard, D. H. (2002). Perceptual assessment of demosaicing algorithm performance. *Proceedings of the IEEE*, 90(1):123–132.
- [Loraux, 2018] Loraux, C. (2018). *Long-term monitoring of existing wind turbine towers and fatigue performance of UHPFRC under compressive stresses*. PhD thesis, Ecole Polytechnique Federale de Lausanne.
- [Lorentz and Wadier, 2004] Lorentz, E. and Wadier, Y. (2004). L’approche énergétique de la rupture élastoplastique appliquée à la modélisation de propagation d’une entaille. *Revue Européenne des Eléments*, 13(5-7):583–592.
- [Lorentz et al., 2000] Lorentz, E., Wadier, Y., and Debruyne, G. (2000). Mécanique de la rupture fragile en présence de plasticité: définition d’un taux de restitution d’énergie. *Comptes Rendus de l’Académie des Sciences-Series IIB-Mechanics*, 328(9):657–662.
- [Lu and Cary, 2000] Lu, H. and Cary, P. D. (2000). Deformation measurements by digital image correlation: implementation of a second-order displacement gradient. *Experimental mechanics*, 40(4):393–400.
- [Ma et al., 2019] Ma, Y., Martinez-Vazquez, P., and Baniotopoulos, C. (2019). Wind turbine tower collapse cases: a historical overview. *Proceedings of the Institution of Civil Engineers-Structures and Buildings*, 172(8):547–555.
- [Mabel et al., 2011] Mabel, M. C., Raj, R. E., and Fernandez, E. (2011). Analysis on reliability aspects of wind power. *Renewable and Sustainable Energy Reviews*, 15(2):1210–1216.
- [Mahalanobis, 1936] Mahalanobis, P. C. (1936). On the generalised distance in statistics. *Proceedings of the National Institute of Sciences of India*, 2(1):49–55.
- [Marante and Flórez-López, 2003] Marante, M. E. and Flórez-López, J. (2003). Three-dimensional analysis of reinforced concrete frames based on lumped damage mechanics. *International Journal of Solids and Structures*, 40(19):5109–5123.
- [Marante et al., 2012] Marante, M. E., Picón, R., Guerrero, N., and Flórez-López, J. (2012). Local buckling in tridimensional frames: experimentation and simplified analysis. *Latin American Journal of Solids & Structures*, 9(6).

- [Martinez-Luengo et al., 2016] Martinez-Luengo, M., Kolios, A., and Wang, L. (2016). Structural health monitoring of offshore wind turbines: A review through the statistical pattern recognition paradigm. *Renewable and Sustainable Energy Reviews*, 64:91–105.
- [Mathieu et al., 2012] Mathieu, F., Hild, F., and Roux, S. (2012). Identification of a crack propagation law by digital image correlation. *International Journal of Fatigue*, 36(1):146–154.
- [Mathieu et al., 2015] Mathieu, F., Leclerc, H., Hild, F., and Roux, S. (2015). Estimation of elastoplastic parameters via weighted FEMU and integrated-DIC. *Experimental Mechanics*, 55(1):105–119.
- [McAlorum et al., 2018] McAlorum, J., Perry, M., Fusiek, G., Niewczas, P., McKeeman, I., and Rubert, T. (2018). Deterioration of cracks in onshore wind turbine foundations. *Engineering Structures*, 167:121–131.
- [McNeill et al., 1987] McNeill, S., Peters, W., and Sutton, M. A. (1987). Estimation of stress intensity factor by digital image correlation. *Engineering fracture mechanics*, 28(1):101–112.
- [Melgosa et al., 1994] Melgosa, M., Quesada, J. J., and Hita, E. (1994). Uniformity of some recent color metrics tested with an accurate color-difference tolerance dataset. *Applied Optics*, 33(34):8069–8077.
- [Mendoza et al., 2019] Mendoza, A., Schneider, J., Parra, E., Obert, E., and Roux, S. (2019). Differentiating 3d textile composites: A novel field of application for digital volume correlation. *Composite Structures*, 208:735–743.
- [Meteo-France, 2020] Meteo-France (2020). Meteo france website. <https://www.meteofrance.com>.
- [Miladi and Razzaghi, 2014] Miladi, S. and Razzaghi, M. S. (2014). A parametric study on inelastic buckling in steel cylindrical shells with circular cutouts. *International Journal of Advanced Structural Engineering*, 6(1):47.
- [Milano et al., 2019] Milano, D., Peyrard, C., Capaldo, M., Ingram, D., Xiao, Q., and Johanning, L. (2019). Impact of high order wave loads on a 10 mw tension-leg platform floating wind turbine at different tendon inclination angles. In *ASME 2019 38th International Conference on Ocean, Offshore and Arctic Engineering*. American Society of Mechanical Engineers Digital Collection.
- [Miner et al., 1945] Miner, M. A. et al. (1945). Cumulative fatigue damage. *Journal of applied mechanics*, 12(3):A159–A164.
- [Mohamed et al., 2019] Mohamed, Y. S., Shehata, H. M., Abdellatif, M., and Awad, T. H. (2019). Steel crack depth estimation based on 2d images using artificial neural networks. *Alexandria Engineering Journal*.

- [Moschas and Stiros, 2011] Moschas, F. and Stiros, S. (2011). Measurement of the dynamic displacements and of the modal frequencies of a short-span pedestrian bridge using GPS and an accelerometer. *Engineering Structures*, 33(1):10–17.
- [Moschas and Stiros, 2014] Moschas, F. and Stiros, S. (2014). High accuracy measurement of deflections of an electricity transmission line tower. *Engineering structures*, 80:418–425.
- [Munier et al., 2010] Munier, R., Doudard, C., Calloch, S., and Weber, B. (2010). Digital image correlation and infrared measurements to determine the influence of a uniaxial pre-strain on fatigue properties of a dual phase steel. In *EPJ Web of Conferences*, volume 6, page 37007. EDP Sciences.
- [Musallam and Johnson, 2012] Musallam, M. and Johnson, C. M. (2012). An efficient implementation of the rainflow counting algorithm for life consumption estimation. *IEEE Transactions on reliability*, 61(4):978–986.
- [Nag-Chowdhury et al., 2018] Nag-Chowdhury, S., Bellégou, H., Pillin, I., Castro, M., Longrais, P., and Feller, J. F. (2018). Crossed investigation of damage in composites with embedded quantum resistive strain sensors (sQRS), acoustic emission (AE) and digital image correlation (DIC). *Composites Science and Technology*, 160:79–85.
- [Nasirmanesh and Mohammadi, 2017] Nasirmanesh, A. and Mohammadi, S. (2017). Eigenvalue buckling analysis of cracked functionally graded cylindrical shells in the framework of the extended finite element method. *Composite Structures*, 159:548–566.
- [Negggers et al., 2018] Neggers, J., Allix, O., Hild, F., and Roux, S. (2018). Big data in experimental mechanics and model order reduction: today’s challenges and tomorrow’s opportunities. *Archives of Computational Methods in Engineering*, 25(1):143–164.
- [Noon, 2000] Noon, R. K. (2000). *Forensic engineering investigation*. CRC Press.
- [Nouy, 2010] Nouy, A. (2010). Proper generalized decompositions and separated representations for the numerical solution of high dimensional stochastic problems. *Archives of Computational Methods in Engineering*, 17(4):403–434.
- [Olaszek, 1999] Olaszek, P. (1999). Investigation of the dynamic characteristic of bridge structures using a computer vision method. *Measurement*, 25(3):227–236.
- [Özbek, 2013] Özbek, M. (2013). *Optical monitoring and operational modal analysis of large wind turbines*. PhD thesis, Technical University of Delft, Netherlands.
- [Pan, 2011] Pan, B. (2011). Recent progress in digital image correlation. *Experimental mechanics*, 51(7):1223–1235.

- [Pan et al., 2016] Pan, B., Tian, L., and Song, X. (2016). Real-time, non-contact and targetless measurement of vertical deflection of bridges using off-axis digital image correlation. *Ndt & E International*, 79:73–80.
- [Pan et al., 2015] Pan, B., Wang, B., Lubineau, G., and Moussawi, A. (2015). Comparison of subset-based local and finite element-based global digital image correlation. *Experimental Mechanics*, 55(5):887–901.
- [Pan et al., 2012] Pan, B., Wu, D., and Xia, Y. (2012). An active imaging digital image correlation method for deformation measurement insensitive to ambient light. *Optics & Laser Technology*, 44(1):204–209.
- [Paris, 1961] Paris, P. C. (1961). A rational analytic theory of fatigue. *The trend in engineering*, 13:9.
- [Paris and Erdogan, 1963] Paris, P. C. and Erdogan, F. (1963). A critical analysis of crack propagation laws. *Journal of Basic Engineering*, 85:528–534.
- [Parisien, 2018] Parisien, L. (2018). Les chutes d'éoliennes, des accidents rares et spectaculaires. *Le Parisien*.
- [Passieux et al., 2018] Passieux, J.-C., Bouclier, R., and Périé, J.-N. (2018). A space-time PGD-DIC algorithm. *Experimental Mechanics*, 58(7):1195–1206.
- [Passieux and Périé, 2012] Passieux, J.-C. and Périé, J.-N. (2012). High resolution digital image correlation using proper generalized decomposition: PGD-DIC. *International Journal for Numerical Methods in Engineering*, 92(6):531–550.
- [Peng et al., 2012] Peng, B., Zhang, Q., Zhou, W., Hao, X., and Ding, L. (2012). Modified correlation criterion for digital image correlation considering the effect of lighting variations in deformation measurements. *Optical Engineering*, 51(1):017004.
- [Pérez et al., 2013] Pérez, J. M. P., Márquez, F. P. G., Tobias, A., and Papaelias, M. (2013). Wind turbine reliability analysis. *Renewable and Sustainable Energy Reviews*, 23:463–472.
- [Périé et al., 2002] Périé, J.-N., Calloch, S., Cluzel, C., and Hild, F. (2002). Analysis of a multiaxial test on a C/C composite by using digital image correlation and a damage model. *Experimental Mechanics*, 42(3):318–328.
- [Peters et al., 1983] Peters, W. H., Ranson, W. F., Sutton, M. A., Chu, T. C., and Anderson, J. (1983). Application of digital correlation methods to rigid body mechanics. *Optical Engineering*, 22(6):226738.
- [Petiot et al., 2015] Petiot, C., Roux, S., and Hild, F. (2015). Multi-scale method for measuring the shape, movement and/or deformation of a structural part subjected to stresses by creating a plurality

of colorimetric speckled patterns. U.S. Patent No. 9,852,514. *Washington, DC: U.S Patent and Trademark Office.*

[Ponomarenko et al., 2009] Ponomarenko, N., Lukin, V., Zelensky, A., Egiazarian, K., Carli, M., and Battisti, F. (2009). Tid2008-a database for evaluation of full-reference visual quality assessment metrics. *Advances of Modern Radioelectronics*, 10(4):30–45.

[Poozesh et al., 2014] Poozesh, P., Baqersad, J., Niezrecki, C., Harvey, E., and Yarala, R. (2014). Full field inspection of a utility scale wind turbine blade using digital image correlation. *CAMX, Orlando, FL*, 10(2.1):2891–2960.

[Popko et al., 2012] Popko, W., Vorpahl, F., Zuga, A., Kohlmeier, M., Jonkman, J., Robertson, A., Larsen, T. J., Yde, A., Saetertro, K., Okstad, K. M., et al. (2012). Offshore code comparison collaboration continuation (OC4), Phase I-results of coupled simulations of an offshore wind turbine with jacket support structure. Technical report, National Renewable Energy Lab.(NREL), Golden, CO (United States).

[Post and Cupp, 1990] Post, M. J. and Cupp, R. E. (1990). Optimizing a pulsed doppler lidar. *Applied optics*, 29(28):4145–4158.

[Ragan and Manuel, 2007] Ragan, P. and Manuel, L. (2007). Comparing estimates of wind turbine fatigue loads using time-domain and spectral methods. *Wind engineering*, 31(2):83–99.

[Raišutis et al., 2008] Raišutis, R., Jasiūnienė, E., Šliteris, R., and Vladišauskas, A. (2008). The review of non-destructive testing techniques suitable for inspection of the wind turbine blades. *Ultragarsas" Ultrasound"*, 63(2):49–52.

[Reder et al., 2016] Reder, M. D., Gonzalez, E., and Melero, J. J. (2016). Wind turbine failures-tackling current problems in failure data analysis. In *Journal of Physics: Conference Series*, volume 753, page 072027. IOP Publishing.

[Régál et al., 2017] Régál, X., Cumunel, G., Bornert, M., and Quiertant, M. (2017). Analyse modale d'une poutre par corrélation d'images numériques. In *Congrès français de mécanique*. AFM, Association Française de Mécanique.

[Rethore et al., 2005] Rethore, J., Gravouil, A., Morestin, F., and Combescure, A. (2005). Estimation of mixed-mode stress intensity factors using digital image correlation and an interaction integral. *International Journal of Fracture*, 132(1):65–79.

[Reynders, 2012] Reynders, E. (2012). System identification methods for (operational) modal analysis: review and comparison. *Archives of Computational Methods in Engineering*, 19(1):51–124.

- [Rhode and Lundquist, 1931] Rhode, R. V. and Lundquist, E. E. (1931). *Strength Tests on Paper Cylinders in Compression, Bending, and Shear*. Number 370. National Advisory Committee for Aeronautics.
- [Rice, 1968] Rice, J. R. (1968). A path independent integral and the approximate analysis of strain concentration by notches and cracks. *Journal of Applied Mechanics*, 35:379–386.
- [Rizo-Patron and Sirohi, 2017] Rizo-Patron, S. and Sirohi, J. (2017). Operational modal analysis of a helicopter rotor blade using digital image correlation. *Experimental Mechanics*, 57(3):367–375.
- [Robertson et al., 2017] Robertson, A. N., Wendt, F., Jonkman, J. M., Popko, W., Dagher, H., Gueydon, S., Qvist, J., Vittori, F., Azcona, J., Uzunoglu, E., et al. (2017). OC5 project phase II: validation of global loads of the DeepCwind floating semisubmersible wind turbine. *Energy Procedia*, 137:38–57.
- [Rolfe and Barsom, 1977] Rolfe, S. T. and Barsom, J. M. (1977). *Fracture and fatigue control in structures: Applications of fracture mechanics*. ASTM International.
- [Roux and Hild, 2006] Roux, S. and Hild, F. (2006). Stress intensity factor measurements from digital image correlation: post-processing and integrated approaches. *International journal of fracture*, 140(1-4):141–157.
- [Roux et al., 2009] Roux, S., Réthoré, J., and Hild, F. (2009). Digital image correlation and fracture: an advanced technique for estimating stress intensity factors of 2D and 3D cracks. *Journal of Physics D: Applied Physics*, 42(21):214004.
- [Roux-Langlois et al., 2015] Roux-Langlois, C., Gravouil, A., Baietto, M.-C., Réthoré, J., Mathieu, F., Hild, F., and Roux, S. (2015). DIC identification and X-FEM simulation of fatigue crack growth based on the Williams’ series. *International Journal of Solids and Structures*, 53:38–47.
- [Rubert et al., 2019] Rubert, T., Zorzi, G., Fusiek, G., Niewczas, P., McMillan, D., McAlorum, J., and Perry, M. (2019). Wind turbine lifetime extension decision-making based on structural health monitoring. *Renewable Energy*, 143:611–621.
- [Rupil et al., 2011] Rupil, J., Roux, S., Hild, F., and Vincent, L. (2011). Fatigue microcrack detection with digital image correlation. *The Journal of Strain Analysis for Engineering Design*, 46(6):492–509.
- [Rytter, 1993] Rytter, A. (1993). *Vibrational based inspection of civil engineering structures*. PhD thesis, Dept. of Building Technology and Structural Engineering, Aalborg University.
- [Saemi et al., 2015] Saemi, J., Sedighi, M., and Shariati, M. (2015). Numerical and experimental study on buckling and postbuckling behavior of cracked cylindrical shells. *Mechanics of Solids*, 50(5):529–545.

- [Schmaltz and Willner, 2011] Schmaltz, S. and Willner, K. (2011). Identification of orthotropic plastic material parameters for deep-drawing steel using DIC and FEMU. In *COMPLAS XI: proceedings of the XI International Conference on Computational Plasticity: fundamentals and applications*, pages 241–250. CIMNE.
- [Sciuti et al., 2020] Sciuti, V. F., Canto, R. B., Neggers, J., and Hild, F. (2020). On the benefits of correcting brightness and contrast in global digital image correlation: Monitoring cracks during curing and drying of a refractory castable. *Optics and Lasers in Engineering*, 136:106316.
- [Seitl et al., 2019] Seitl, S., Miarka, P., Blasón, S., and Canteli, A. F. (2019). Evaluation of fatigue properties of s355 j2 and s355 j0 by using profatigue software. In *Mechanical Fatigue of Metals*, pages 213–219. Springer.
- [Shi et al., 2016] Shi, Q., Latourte, F., Hild, F., and Roux, S. (2016). Quaternion correlation for tracking crystal motions. *Measurement Science and Technology*, 27(9):095006.
- [Shi et al., 2019] Shi, Q., Roux, S., Latourte, F., and Hild, F. (2019). Estimation of elastic strain by integrated image correlation on electron diffraction patterns. *Ultramicroscopy*, 199:16–33.
- [Smarsly et al., 2013] Smarsly, K., Hartmann, D., and Law, K. H. (2013). An integrated monitoring system for life-cycle management of wind turbines. *International Journal of Smart Structures and Systems*, 12(2):209–233.
- [Smith and Guild, 1931] Smith, T. and Guild, J. (1931). The CIE colorimetric standards and their use. *Transactions of the optical society*, 33(3):73.
- [Sophian et al., 2017] Sophian, A., Tian, G., and Fan, M. (2017). Pulsed eddy current non-destructive testing and evaluation: A review. *Chinese Journal of Mechanical Engineering*, 30(3):500–514.
- [Stehly and Beiter, 2020] Stehly, T. J. and Beiter, P. C. (2020). 2018 cost of wind energy review. Technical report, National Renewable Energy Lab.(NREL), Golden, CO (United States).
- [Stephen et al., 1993] Stephen, G. A., Brownjohn, J. M. W., and Taylor, C. A. (1993). Measurements of static and dynamic displacement from visual monitoring of the humber bridge. *Engineering Structures*, 15(3):197–208.
- [Stiros and Psimoulis, 2012] Stiros, S. C. and Psimoulis, P. A. (2012). Response of a historical short-span railway bridge to passing trains: 3-D deflections and dominant frequencies derived from Robotic Total Station (RTS) measurements. *Engineering Structures*, 45:362–371.
- [Sur and Grediac, 2014] Sur, F. and Grediac, M. (2014). Sensor noise modeling by stacking pseudo-periodic grid images affected by vibrations. *IEEE Signal Processing Letters*, 21(4):432–436.

- [Sutton, 2013] Sutton, M. (2013). Computer vision-based, noncontacting deformation measurements in mechanics: a generational transformation. *Applied Mechanics Reviews*, 65(5):050802.
- [Sutton et al., 2009] Sutton, M. A., Orteu, J. J., and Schreier, H. (2009). *Image correlation for shape, motion and deformation measurements: Basic Concepts, Theory and Applications*. Springer, New York, NY (USA).
- [Sutton et al., 1983] Sutton, M. A., Wolters, W. J., Peters, W. H., Ranson, W. F., and McNeill, S. R. (1983). Determination of displacements using an improved digital correlation method. *Image and vision computing*, 1(3):133–139.
- [Tcherniak et al., 2011] Tcherniak, D., Chauhan, S., and Hansen, M. H. (2011). Applicability limits of operational modal analysis to operational wind turbines. In *Structural Dynamics and Renewable Energy, Volume 1*, pages 317–327. Springer.
- [Tegen et al., 2012] Tegen, S., Hand, M., Maples, B., Lantz, E., Schwabe, P., and Smith, A. (2012). 2010 cost of wind energy review. Technical report, National Renewable Energy Lab.(NREL), Golden, CO (United States).
- [Tehranchi et al., 2011] Tehranchi, M. M., Hamidi, S. M., Eftekhari, H., Karbaschi, M., and Ranjbaran, M. (2011). The inspection of magnetic flux leakage from metal surface cracks by magneto-optical sensors. *Sensors and Actuators A: Physical*, 172(2):365–368.
- [The-Civil-Engineer, 2017] The-Civil-Engineer (2017). Wind turbine collapse in eastern germany. <https://www.thecivilengineer.org/>.
- [Tibaldi et al., 2016] Tibaldi, C., Henriksen, L., Hansen, M., and Bak, C. (2016). Wind turbine fatigue damage evaluation based on a linear model and a spectral method. *Wind Energy*, 19(7):1289–1306.
- [Timoshenko, 1910] Timoshenko, S. P. (1910). Einige stabilitätsprobleme der elastizitätstheorie. *Zeitschrift für Mathematik und Physik*, 58(4):337–385.
- [Tong, 2005] Tong, W. (2005). An evaluation of digital image correlation criteria for strain mapping applications. *Strain*, 41(4):167–175.
- [Toussaint et al., 2006] Toussaint, E., Grédiac, M., and Pierron, F. (2006). The virtual fields method with piecewise virtual fields. *International Journal of Mechanical Sciences*, 48(3):256–264.
- [UL, 2016] UL (2016). Outline of investigation for wind turbine generator life time extension. *LTE*.
- [UNFCCC, 2009] UNFCCC, U. (2009). Kyoto protocol reference manual on accounting of emissions and assigned amount. *esocialsciences.com, Working Papers*.

- [Valla et al., 2015] Valla, M., Gueguen, P., Augère, B., Goular, D., and Perrault, M. (2015). Remote modal study of reinforced concrete buildings using a multipath lidar vibrometer. *Journal of Structural Engineering*, 141(1):D4014005.
- [Vaziri and Estekanchi, 2006] Vaziri, A. and Estekanchi, H. E. (2006). Buckling of cracked cylindrical thin shells under combined internal pressure and axial compression. *Thin-Walled Structures*, 44(2):141–151.
- [Veers and Winterstein, 1998] Veers, P. S. and Winterstein, S. R. (1998). Application of measured loads to wind turbine fatigue and reliability analysis. *Journal of Solar Energy Engineering*, 120(4):233–239.
- [Veritas, 2016] Veritas, D. N. (2016). Lifetime extension of wind turbines. *Edition March*, 3.
- [Vermeij and Hoefnagels, 2018] Vermeij, T. and Hoefnagels, J. P. M. (2018). A consistent full-field integrated DIC framework for HR-EBSD. *Ultramicroscopy*, 191:44–50.
- [Wagne et al., 2002] Wagne, B., Roux, S., and Hild, F. (2002). Spectral approach to displacement evaluation from image analysis. *The European Physical Journal Applied Physics*, 17(3):247–252.
- [Wang and Zhang, 2017] Wang, L. and Zhang, Z. (2017). Automatic detection of wind turbine blade surface cracks based on uav-taken images. *IEEE Transactions on Industrial Electronics*, 64(9):7293–7303.
- [Wang, 2019] Wang, Y. (2019). *Fatigue Thermique à grand nombre de cycles d'un acier inoxydable austénitique: apport des mesures de champs pour l'identification du chargement et le suivi in-situ de l'endommagement*. PhD thesis, Université Paris-Saclay.
- [Wang et al., 2019] Wang, Y., Charbal, A., Dufour, J.-E., Hild, F., Roux, S., and Vincent, L. (2019). Hybrid multiview correlation for measuring and monitoring thermomechanical fatigue test. *Experimental Mechanics*, DOI: 10.1007/s11340-019-00500-8.
- [Wen et al., 2009] Wen, J., Zheng, Y., and Donghan, F. (2009). A review on reliability assessment for wind power. *Renewable and sustainable energy reviews*, 13(9):2485–2494.
- [Westergaard, 1933] Westergaard, H. M. (1933). Stresses at a crack, size of the crack, and the bending of reinforced concrete. In *Journal Proceedings*, volume 30, pages 93–102.
- [Winstroth et al., 2014] Winstroth, J., Schoen, L., Ernst, B., and Seume, J. R. (2014). Wind turbine rotor blade monitoring using digital image correlation: a comparison to aeroelastic simulations of a multi-megawatt wind turbine. In *Journal of Physics: Conference Series*, volume 524, page 012064. IOP Publishing.

- [Wiser et al., 2016] Wiser, R., Hand, M., Seel, J., and Paulos, B. (2016). Reducing wind energy costs through increased turbine size: is the sky the limit. *Rev. Berkeley National Laboratory Electricity Markets and Policy Group*.
- [Wöhler, 1867] Wöhler, A. (1867). Wöhler's experiments on the strength of metals. *Engineering*, 4:160–161.
- [Wu et al., 2019] Wu, R., Zhang, D., Yu, Q., Jiang, Y., and Arola, D. (2019). Health monitoring of wind turbine blades in operation using three-dimensional digital image correlation. *Mechanical Systems and Signal Processing*, 130:470–483.
- [Wymore et al., 2015] Wymore, M. L., Van Dam, J. E., Ceylan, H., and Qiao, D. (2015). A survey of health monitoring systems for wind turbines. *Renewable and Sustainable Energy Reviews*, 52:976–990.
- [Yamaguchi and Hashimoto, 2010] Yamaguchi, T. and Hashimoto, S. (2010). Fast crack detection method for large-size concrete surface images using percolation-based image processing. *Machine Vision and Applications*, 21(5):797–809.
- [Yang and Jiang, 2011] Yang, W. and Jiang, J. (2011). Wind turbine condition monitoring and reliability analysis by scada information. In *2011 Second International Conference on Mechanic Automation and Control Engineering*, pages 1872–1875. IEEE.
- [Yates et al., 2010] Yates, J. R., Zanganeh, M., and Tai, Y. H. (2010). Quantifying crack tip displacement fields with dic. *Engineering Fracture Mechanics*, 77(11):2063–2076.
- [Yeh et al., 1999] Yeh, M.-K., Lin, M.-C., and Wu, W.-T. (1999). Bending buckling of an elastoplastic cylindrical shell with a cutout. *Engineering structures*, 21(11):996–1005.
- [Yigit et al., 2010] Yigit, C. O., Li, X., Inal, C., Ge, L., and Yetkin, M. (2010). Preliminary evaluation of precise inclination sensor and GPS for monitoring full-scale dynamic response of a tall reinforced concrete building. *Journal of Applied Geodesy*, 4(2):103–113.
- [Yoneyama and Ueda, 2012] Yoneyama, S. and Ueda, H. (2012). Bridge deflection measurement using digital image correlation with camera movement correction. *Materials transactions*, 53(2):285–290.
- [Yu and Pan, 2017a] Yu, L. and Pan, B. (2017a). Color stereo-digital image correlation method using a single 3CCD color camera. *Experimental Mechanics*, 57(4):649–657.
- [Yu and Pan, 2017b] Yu, L. and Pan, B. (2017b). Full-frame, high-speed 3D shape and deformation measurements using stereo-digital image correlation and a single color high-speed camera. *Optics and Lasers in Engineering*, 95:17–25.

- [Zendehbad et al., 2017] Zendehbad, M., Chokani, N., and Abhari, R. S. (2017). Measurements of tower deflections on full-scale wind turbines using an opto-mechanical platform. *Journal of Wind Engineering and Industrial Aerodynamics*, 168:72–80.
- [Zhao et al., 2019] Zhao, B., Lei, D., Fu, J., Yang, L., and Xu, W. (2019). Experimental study on micro-damage identification in reinforced concrete beam with wavelet packet and DIC method. *Construction and Building Materials*, 210:338–346.
- [Ziegler et al., 2018] Ziegler, L., Gonzalez, E., Rubert, T., Smolka, U., and Melero, J. J. (2018). Lifetime extension of onshore wind turbines: A review covering germany, spain, denmark, and the uk. *Renewable and Sustainable Energy Reviews*, 82:1261–1271.
- [Zivanovic and Carlosena, 2002] Zivanovic, M. and Carlosena, A. (2002). Extending the limits of resolution for narrow-band harmonic and modal analysis: a non-parametric approach. *Measurement Science and Technology*, 13(12):2082.

Titre : Détection d'endommagement dans les tours d'éoliennes terrestres par Corrélation d'Images Numériques

Mots clés : Corrélation d'images numériques, Endommagement, Energie éolienne

Résumé : Pour développer l'exploitation des éoliennes, l'optimisation de la maintenance des tours est un élément clef, qui motive ce travail. Premièrement, une étude sur la criticité d'une fissure vis-à-vis de sa propagation brutale est montré être le facteur dimensionnant pour la résistance de la structure vis-à-vis d'épisodes environnementaux extrêmes, ce qui nous permet de définir l'endommagement minimum qu'il convient de détecter. Dans ce but, l'imagerie optique, et plus spécifiquement la Corrélation d'Images Numériques, CIN, a été exploitée via le déploiement de deux stratégies : l'une à l'échelle de la structure, et la seconde, à une échelle mésoscopique. Une analyse modale par CIN a également été réalisée.

Title: Damage detection for wind turbine towers with Digital Image Correlation

Keywords: Digital image correlation, Damage, Wind energy

Abstract:In order to develop the exploitation of wind turbines, the optimization of tower maintenance is a key element which motivates this work. Firstly, a study of the propagation of a crack is shown to be the limiting factor for designing a structure able to sustain extreme environmental events, and a critical crack size that should be detectable is defined. Thanks to plain optical imaging, and more specifically Digital Image Correlation (DIC), two strategies are envisioned, either at the structural scale or at a mesoscopic one. Additionally a DIC-based modal analysis is shown to be feasible and accurate.

